

1993

Light scattering from periodic surfaces and turned surface roughness measurement.

Yiying. Fan
University of Windsor

Follow this and additional works at: <http://scholar.uwindsor.ca/etd>

Recommended Citation

Fan, Yiying, "Light scattering from periodic surfaces and turned surface roughness measurement." (1993). *Electronic Theses and Dissertations*. Paper 2610.

This online database contains the full-text of PhD dissertations and Masters' theses of University of Windsor students from 1954 forward. These documents are made available for personal study and research purposes only, in accordance with the Canadian Copyright Act and the Creative Commons license—CC BY-NC-ND (Attribution, Non-Commercial, No Derivative Works). Under this license, works must always be attributed to the copyright holder (original author), cannot be used for any commercial purposes, and may not be altered. Any other use would require the permission of the copyright holder. Students may inquire about withdrawing their dissertation and/or thesis from this database. For additional inquiries, please contact the repository administrator via email (scholarship@uwindsor.ca) or by telephone at 519-253-3000ext. 3208.



National Library
of Canada

Acquisitions and
Bibliographic Services Branch

395 Wellington Street
Ottawa, Ontario
K1A 0N4

Bibliothèque nationale
du Canada

Direction des acquisitions et
des services bibliographiques

395, rue Wellington
Ottawa (Ontario)
K1A 0N4

Your file Votre référence

Our file Notre référence

NOTICE

The quality of this microform is heavily dependent upon the quality of the original thesis submitted for microfilming. Every effort has been made to ensure the highest quality of reproduction possible.

If pages are missing, contact the university which granted the degree.

Some pages may have indistinct print especially if the original pages were typed with a poor typewriter ribbon or if the university sent us an inferior photocopy.

Reproduction in full or in part of this microform is governed by the Canadian Copyright Act, R.S.C. 1970, c. C-30, and subsequent amendments.

AVIS

La qualité de cette microforme dépend grandement de la qualité de la thèse soumise au microfilmage. Nous avons tout fait pour assurer une qualité supérieure de reproduction.

S'il manque des pages, veuillez communiquer avec l'université qui a conféré le grade.

La qualité d'impression de certaines pages peut laisser à désirer, surtout si les pages originales ont été dactylographiées à l'aide d'un ruban usé ou si l'université nous a fait parvenir une photocopie de qualité inférieure.

La reproduction, même partielle, de cette microforme est soumise à la Loi canadienne sur le droit d'auteur, SRC 1970, c. C-30, et ses amendements subséquents.

**LIGHT SCATTERING FROM PERIODIC SURFACES AND
TURNED SURFACE ROUGHNESS MEASUREMENT**

by

Yiying Fan

A Dissertation
Submitted to the Faculty of Graduate Studies and Research
through the Department of Mechanical Engineering
in Partial Fulfillment
of the Requirements for the Degree of
Doctor of Philosophy
at the University of Windsor

Windsor, Ontario, Canada
1992

© 1992, Yiying Fan



National Library
of Canada

Acquisitions and
Bibliographic Services Branch

395 Wellington Street
Ottawa, Ontario
K1A 0N4

Bibliothèque nationale
du Canada

Direction des acquisitions et
des services bibliographiques

395, rue Wellington
Ottawa (Ontario)
K1A 0N4

Vous dir - *Votre référence*

Our file - *Notre référence*

The author has granted an irrevocable non-exclusive licence allowing the National Library of Canada to reproduce, loan, distribute or sell copies of his/her thesis by any means and in any form or format, making this thesis available to interested persons.

The author retains ownership of the copyright in his/her thesis. Neither the thesis nor substantial extracts from it may be printed or otherwise reproduced without his/her permission.

L'auteur a accordé une licence irrévocable et non exclusive permettant à la Bibliothèque nationale du Canada de reproduire, prêter, distribuer ou vendre des copies de sa thèse de quelque manière et sous quelque forme que ce soit pour mettre des exemplaires de cette thèse à la disposition des personnes intéressées.

L'auteur conserve la propriété du droit d'auteur qui protège sa thèse. Ni la thèse ni des extraits substantiels de celle-ci ne doivent être imprimés ou autrement reproduits sans son autorisation.

ISBN 0-315-83051-4

Canada

ABSTRACT

This dissertation deals with the light scattering from machined periodic surfaces, such as turned surfaces, whose roughness amplitude is greater than the illumination wavelength. The main objective is to establish a theoretical basis for the development of an optical technique for in-process surface roughness measurement.

The Beckmann's scalar scattering model was used to determine the scattering patterns for the case where the incident plane was perpendicular to the lay and the case where the incident plane is parallel to the lay. It was obtained that the intensity of any given scattering order oscillated as the incident angle changed. The degree of oscillation was directly related to roughness; as roughness increased the number of oscillations increased. This observation was supported by scattering measurements from flat periodic surfaces. Solutions for the light scattering from cylindrical surfaces were also derived from the flat surface scattering model by using the principle of superposition. A special scattering geometry was considered where the incident plane was restricted to a direction parallel to the lay and near zero grazing angles were utilized. Numerical results were then obtained for different cylindrical surfaces having sinusoidal roughness profiles. These results were later confirmed by scattering measurements from turned surfaces having varied roughness and different materials. In these measurements, it was observed that the surface wavelength was inversely proportional to the fringe spacing. In addition, the location of the first intensity minimum on the central fringe was related to the amplitude of the surface roughness. From these two observations, a new surface roughness measurement technique was developed. This technique makes use of the scattering pattern of the surface to determine both the surface roughness and wavelength. Tested results correlated well with the stylus method. A reasonable accuracy and repeatability were achieved. It was also found that this technique was capable of measuring surface wavelengths from 10 μm to 300 μm and surface roughness (R_a) from 1 to 10 μm . In comparison to other techniques, this method is relatively simple, independent of material property and capable of fast processing speed. In light of these features, it holds great promise for in-process applications.

Dedicated to
my parents and sisters

ACKNOWLEDGEMENTS

I would like to express my sincere gratitude to my supervisors, Dr. V. M. Huynh and Dr. N. Singh, for their continued guidance and support throughout the project. I would also like to thank my supervisory committee members, Dr. W. P. T. North, Dr. Z. F. Reif, and Dr. J. Soltis for their valuable comments and suggestions.

I also wish to express my appreciation to:

- Mr. Lawrence Cuthbert of Sensor Adaptive Machines, Inc., Windsor, Ontario, for helping me with his expertise in surface roughness measurement and for supplying turned samples which were valuable for this research;

- Faculty of Graduate Studies and Research for financial support through scholarships and assistantship;

- The Mechanical Engineering Department staff for their excellent technical assistance;

- My fellow graduate students for their friendship and advice;

- Mary for her encouragement, understanding, and faith, which gave me the confidence and determination to see this through to the end.

TABLE OF CONTENTS

ABSTRACT	iii
DEDICATION	iv
ACKNOWLEDGEMENTS	v
LIST OF TABLES	viii
LIST OF FIGURES	ix
NOMENCLATURE	xi
CHAPTER	
I. INTRODUCTION	1
1.1 Background and Motivations	1
1.2 Research on Optical Techniques	4
1.2.1 Interferometry	5
1.2.2 Optical Profilometers	6
1.2.3 Surface Image Analysis	6
1.2.4 Laser Doppler Vibrometry	7
1.2.5 Light Scattering	7
1.3 Light Scattering Theory	13
1.4 Turned Surface Generation	17
1.5 Objectives	18
II. THE BECKMANN'S MODEL	20
2.1 General Scattering Formula	20
2.2 Solution for Periodic Surfaces	23
2.3 Solution for Random Surfaces	24
2.4 A Two-Scale Surface Model	27
III. NUMERICAL SOLUTION OF THE SCATTERING PATTERN	29
3.1 Scattering Model	29
3.2 Numerical Procedure	31
3.3 Results and Discussion	34
3.3.1 Scattering from a Given Incident Angle	34
3.3.2 Component Intensity versus the Incident Angle	35
3.4 Experimental Evidence	37
3.4.1 Experiment Setup and Procedure	37
3.4.2 Results and Comparison	38

3.4.3 Surface Roughness Estimation	39
3.5 Summary	40
IV. SCATTERING FROM INCIDENCE PARALLEL TO THE LAY	42
4.1 Scattering Model	42
4.2 Numerical Results and Discussion	45
4.3 Experiment and Results	49
4.4 Comparison between Theory and Experiment	50
4.5 Summary	51
V. LIGHT SCATTERING FROM TURNED SURFACES AND SURFACE ROUGHNESS MEASUREMENT	53
5.1 Scattering Model for A Cylindrical Surface	53
5.2 Numerical Solutions	56
5.3 Experimental Setup and Results	57
5.4 Discission	58
5.4.1 General Scattering Pattern	58
5.4.2 Surface Wavelength	59
5.4.3 Surface Roughness Amplitude	60
5.4.4 Comparison of Results	60
5.5 Additional Evidence	61
5.6 Surface Texture Measurement Procedure	62
5.6.1 Principles	63
5.6.2 Test Results and Comparison with the Stylus Data	67
5.6.3 Performance	68
5.6.4 Advantages and Weaknesses	74
5.7 Summary	75
VI. CONCLUSIONS AND RECOMMENDATIONS	77
6.1 Contribution	77
6.2 Conclusions	79
6.3 Recommendations	80
REFERENCES	82
TABLES	88
FIGURES	92
APPENDIX A. Double Scattering Formula by Ray Optics	130
APPENDIX B. Equipment Specifications	133
VITA AUCTORIS	134

LIST OF TABLES

Table	page
Table 1.1 Roughness produced by common production methods	89
Table 1.2 Various attributes of surface roughness measurement techniques	90
Table 5.1 Surface roughness parameters for the sinusoidal profiles used in the calculation	91
Table 5.2 Surface roughness data of turned samples used in the experiment	91

LIST OF FIGURES

Figure	page
Figure 1.1 Turned surface geometry	93
Figure 2.1 General scattering geometry	94
Figure 2.2 Periodic scattering pattern	94
Figure 2.3 Two-scale scattering pattern formation	95
Figure 3.1 Scattering geometry	96
Figure 3.2 Various surface profiles used in the study	96
Figure 3.3 The scattering pattern from a fixed incident angle	97
Figure 3.4 The scattering patterns from a fixed incident angle for different surface profiles	98
Figure 3.5 Intensity variation versus incident angle (sinusoidal surface profile)	99
Figure 3.6 Intensity variation versus incident angle (triangular surface profile)	99
Figure 3.7 Intensity variation versus incident angle (half-sinusoidal surface profile)	100
Figure 3.8 Intensity variation versus incident angle (cusp surface profile)	100
Figure 3.9 Intensity of $m=1$ scattering order versus incident angle (cusp surface profile)	101
Figure 3.10a,b Stylus measurements of GAR standard sample A	102
Figure 3.10c,d Stylus measurement of GAR standard sample B	103
Figure 3.11 The setup for scattering measurement	104
Figure 3.12 Comparison of intensity of the scattering patterns: (a) measured (b) calculated	105
Figure 3.13 Measured scattering intensity of the zero order fringe versus incident angle	106
Figure 3.14 Scattering pattern of Sample B	107
Figure 3.15 Scattering pattern of a turned sample	107
Figure 4.1 A diagram for the scattering geometry	108
Figure 4.2 A diagram for the screen coordinate system including the measurement setup	108
Figure 4.3 Calculated scattering peaks for five sinusoidal surfaces of different roughness amplitudes	109
Figure 4.4 Calculated scattering peaks for five triangular surfaces of different roughness amplitudes	110
Figure 4.5 Calculated fringe spacing versus surface wavelength	111

Figure 4.6 Intensity of zero order fringe versus grazing angle for sinusoidal surface profile	111
Figure 4.7 Intensity of $m=1$ order fringe versus grazing angle for sinusoidal surface profile	112
Figure 4.8a, b Photographs of the scattering patterns: (a): sample A, (b): sample B	113
Figure 4.8c, d Intensity profiles: (c): sample A, (d): sample B	114
Figure 4.9 Comparison of the measured scattering pattern from sample A and the prediction using a sinusoidal surface profile	115
Figure 4.10 Comparison of the measured scattering pattern from sample B and the prediction using a sinusoidal surface profile	115
Figure 4.11 Intensity versus incident angle of Sample B: (a) Theoretical results, (b) Experiment data	116
Figure 5.1 A diagram for the scattering geometry from a cylindrical surface including the measurement setup	117
Figure 5.2 Cylindrical scattering on the incident plane and its coordinate system	117
Figure 5.3 Intensity variation along screen ordinate Z_s	118
Figure 5.4 Surface roughness profile and its Fourier spectrum of samples A and B as obtained from the stylus instrument	119
Figure 5.5 Photographs of the scattering patterns of turned surfaces of different roughness (Samples A to E)	120
Figure 5.6 Cross-fringe intensity distributions for Samples A to E	121
Figure 5.7 Comparison of fringe spacing versus surface wavelength curves between experiment and theory	122
Figure 5.8 Measured fringe intensity distribution along the zero-order plane for five test samples (A to E)	122
Figure 5.9 Predicted peak intensity versus roughness using the sinusoidal surface model	123
Figure 5.10 Predicted surface wavelength (Λ) versus the fringe spacing (Δ)	124
Figure 5.11a Predicted curve for roughness average (R_a) versus ordinate (D_f) of the first minimum on the fringe intensity profile	124
Figure 5.11b Illustration of phase difference in the scattering from a square wave surface profile	125
Figure 5.12 Correlation of surface wavelengths obtained from optical and stylus methods	126
Figure 5.13 Comparison of measured and predicted (D_f) versus average roughness (R_a)	126
Figure 5.14 Correlation of Roughness (R_a) obtained by the optical and stylus methods	127
Figure 5.15 Stability of the test results	127
Figure 5.16 Repeatability of the central fringe intensity distribution	128
Figure 5.17 Repeatability of the cross fringe intensity distribution	128
Figure 5.18 Influence of specimen misalignment on the scattering pattern: (a) proper alignment, (b) 20° mis-aligned	129

Figure A.1 Light reflection from a triangular surface: incident plane perpendicular to the lay	132
Figure A.2 Light reflection from a triangular surface: incident plane parallel to the lay	132

NOMENCLATURE

A	illuminated area
C	autocorrelation coefficient function
D_x	distance from sample to screen
D_f	ordinate of the point of first minimum in the intensity profile
F	geometrical factor
f	feed rate
g	roughness parameter
H	peak-to-valley height
h	surface roughness amplitude
I	intensity
p	probability density distribution function
R	radius of cusp profile, radius of turned samples
R_a	roughness average
I_o	material constant
R_q	root-mean-square roughness
I_s	specular reflectance
R_r	peak-to-valley roughness
r_n	tool-nose radius
T	correlation distance

Greek Letters

α	angle
Δ	finite difference
Δ_f	fringe spacing
ζ	surface height function
θ_1	angle of incidence
θ_2	angle of scattering
θ_3	angle of lateral scattering
Λ	surface spatial wavelength
λ	illumination wavelength
ρ	normalized amplitude or scattering coefficient
σ	variance

Subscripts:

1	incident field
2	scattering field
3	lateral scattering field
L	local coordinate

- p periodic component
- r random component
- s screen coordinate

Superscripts:

- * complex conjugate

Chapter 1

Introduction

1.1 Background and Motivation

In the past four decades, there has been a constant increase in the awareness of the importance of the surface finish of fabricated parts in manufacturing industries. This is because it is realized that an improvement in surface finish often leads to an improved performance or increased machine life. The important role of surface finish or surface texture on various aspects of machine performance such as functioning, lubrication, resistance to wear, load-carrying capacity, etc., has been clearly demonstrated in numerous investigations (Thomas, 1982).

The commonly used instruments for surface roughness measurement are the mechanical stylus-type profilometers. These are based on a relatively simple principle. A stylus, having a small tip radius (in the order of $1\ \mu\text{m}$), is dragged across the surface at a constant speed. Its vertical movement is detected by a displacement transducer such as the Linear Variable Differential Transformer (LVDT), and is amplified to create a time varying signal which is approximately proportional to the amplitude of the surface roughness profile. In the past decade, various improvements have been made to the

instruments to enhance the resolution, portability, and data processing capability. Even though there are a number of other techniques available for use in production industries and research laboratories, at the present time, the stylus instrument is still the only accepted standard (ANSI/ASME B46.1, 1985).

The surface texture can be characterized by a single or multiple parameters or in some cases by some functional forms. Numerous surface roughness parameters have been developed that were derived from the surface roughness profile signals (Whitehouse et al., 1974; Peters et al., 1979). Among them, the Roughness Average, R_a , is defined as an absolute arithmetic mean of the deviation of the roughness profile from the mean line. Because of its simplicity, this parameter has been widely used in the metal cutting industry. Other parameters such as the Root-Mean-Square Roughness, R_q , and the Peak-to-Valley Roughness, R_p , are also used in statistical analysis.

The above parameters, however, only give an indication of the roughness amplitudes and are independent of the spatial wavelength of the profiles. To quantify the openness or closeness of a profile, an average wavelength was introduced for periodic surfaces and a correlation length for surfaces of Gaussian distribution. A hybrid parameter such as the RMS slope of roughness profile can also be used. Table 1.1 shows the range of R_a which is produced in common metal cutting operations. With the advent of digital signal processing instruments, especially those incorporating the Fast Fourier Transform (FFT) algorithm, a host of comprehensive surface characterization techniques has been developed, for example, the Data Dependent Systems methodology (Pandit and Shunmugan, 1992), the fractal surface model (Church, 1988), etc.. Most of them are

to characterize random surfaces with an emphasis on establishing the relationship between surface roughness parameters and cutting conditions.

In general, workpiece surface quality including the dimensional accuracy, the form error, and the surface finish, is primarily dependent on the shape of the tool and the relative movement between the tool and workpiece. Hence, the surface quality is considered as a signature of the tool and the machining process. As such, an analysis of the surface texture can reveal the tool wear, machine-tool conditions such as spindle vibrations, slideway inaccuracies, and misalignment. (Raja, 1983; Hingle, 1987). Recognizing the importance of this application to production and machining industries, a large amount of research work has been carried out in recent years to develop tool and machine condition monitoring systems and adaptive control systems for machine tools (Shiraishi, 1988, 1989a, b). Significant progress has been made, mostly in surface roughness modelling, based on profile information acquired off-line by stylus measurement (Zhang and Kapoor, 1991a, b).

At the present time, there is a lack of suitable surface texture measurement sensors for in-process or on-line quality control and condition monitoring. These applications require fast measurement speeds and the ability to operate in a hostile environment including dirt, cutting fluid and chips. It is also desirable to perform in-process measurement where parts are moving or rotating. Because of these demanding requirements, it is not surprising to find that the attempt to adapt stylus-type instruments was met with very limited success (Whitehouse, 1987).

To overcome the disadvantages of the stylus contact measurements, various innovations in the area of non-contact roughness sensing have ensued (Thomas, 1982).

Table 1.2 shows a summary of different measurement techniques and the associated attributes such as resolution, range, and speed. Among these, the capacitance-based, the ultrasonic, and the optical techniques are the most favorable ones mainly because of their fast measuring speed. Although great improvements have been achieved in the first two techniques in recent years (Garbini et al., 1992; Blessing and Eitzen, 1988), only the optical technique, has experienced rapid progress and holds great promise for surface roughness measurement. This is because the optical techniques have potential for providing high resolution by virtue of relatively short illumination wavelengths. In addition, the proliferation of inexpensive components such as diode lasers, fiber optics, Charge-Coupled Devices (CCD), and digital computers helps to enhance the performance of existing techniques and provides useful tools for the development of new techniques.

There is a great need for developing optical sensors capable of measuring surface roughness of machined parts especially for surfaces which are produced by turning, which is one of the most commonly used metal cutting operations. Thus, the development of such a sensor is one of the primary driving forces for this work.

In the following sections, a review of different optical techniques is given, followed by a description of different light scattering models. This section continues with a description of the surface generation in a cylindrical turning process and finally ends with the thesis objectives.

1.2 Research on Optical Techniques

Optical techniques for surface roughness measurement were historically designed to inspect delicate optical components which could not be touched by the sharp stylus.

A comprehensive review of these methods was given by Vorburger and Teague (1981) and more recently by Bennett and Mattsson (1989). For a complete review of all roughness measurement techniques (including optical techniques), the reader should refer to a paper by Huynh and Fan (1992). In this present survey, a greater emphasis was placed on the measurement of machined surfaces with a view to its in-process capability. In general, optical techniques can be classified into five groups depending on how the different inter-actions between the light and the surface are utilized in the measurement.

1.2.1 Interferometry

The underlying principle of interferometry is that when two coherent beams of light (or light waves) from different paths intersect, they interact with each other to form light or dark patterns or fringes whose intensity is dependent on the path or phase difference between them. The relationship between fringe intensity and phase difference forms a basis for surface roughness height measurement. The measurement system consists of a collimated light beam which is split into two and then focused, through an optical microscope system, to a small spot on both the test surface and the reference surface. Any height variation between the two will cause a path difference which produces interference fringes whose intensity contours are related to the surface roughness topography. Various configurations were devised, some of which may include a video camera for capturing the image which can be subsequently analyzed by a dedicated image processing system. Notable progress has been made in the area of computerized interferogram processing, for example, the Bruning's phase detection algorithm (Robinson et al., 1991). This resulted in a significant improvement in the

measurement speed and resolution. Typical applications include the inspection of super-finished surfaces such as computer disk-drive heads and air bearing surfaces (Mason, 1990).

1.2.2 Optical Profilometers

The principle for these measurement techniques is somewhat similar to that of the mechanical profilometers except that the former uses the adjustment in focusing the light spot on the surface to determine the surface height. Usually a laser is used and its focused spot size is about 1.0 μm in diameter (typical). Focusing is carried out by adjusting the objective lens whose position is measured to indicate the surface height as the surface is traversed across the beam (Brown and Breitmeier, 1988). The accuracy of the method depends largely on techniques used to measure the focusing error. Various research efforts have been made mainly in devising different techniques to detect focusing error and separate it from other disturbances. As the focus detection technique is ultra sensitive to ambient temperature and mechanical disturbance, the method is unlikely to be used in a normal shop floor environment.

1.2.3 Surface Image Analysis

In these techniques, a grey level analysis of microscope images of surfaces, which were illuminated by white light sources, was carried out. A number of parameters have been derived and experimentally related to surface roughness and surface wavelength (Chao et al., 1986; Luk et al., 1989). For controlling roughness in turning, Shiraishi (1989a) utilized a shadow graph on a screen which was created by projecting a light

beam over the top of the cylindrical surface. Another form of roughness image can be created by projecting a light plane through a small aperture on to the inspected surface at an incident angle of 45° . The image is viewed through a microscope at an angle of reflection of 45° (Uchida et al., 1979). These methods usually employ white light sources which preclude any diffraction effect. As a consequence, the measurement range is limited to large scale roughness or waviness such as in rough turned surfaces and sometimes chatter marks.

1.2.4 Laser Doppler Vibrometry

This is a relatively new technique which was essentially designed to measure surface velocity. The test surface is travelling at a constant speed and is illuminated by a coherent light. The motion of the surface will impart a frequency shift to the reflected beam. A velocity signal is then derived from the frequency shift information. From the data of surface velocity in the direction perpendicular to the surface, a displacement profile of the surface can be obtained. This technique was first applied to inspect the magnetic disk surfaces (Bogy et al., 1986) and more recently, roller bearing surfaces (Georgeson and Lieu, 1992). As workpiece motion is inherent in the measurement, this technique lends itself well to in-process applications where the part motion is necessary.

1.2.5 Light Scattering

When light is incident on a rough surface, it will scatter into various directions, each of different intensities. From the scattering pattern, various quantities, such as light intensity, angular distribution, and degree of polarization, can be measured and related

to the surface roughness. A wide variety of roughness measuring techniques was devised based on the measurement of the scattering pattern.

The simplest way to quantify roughness is to measure the intensity of the specular component denoted by I_s . For the case where the surface roughness amplitude is much less than the illumination wavelength, most reflected light is directed in a very narrow cone at an angle equal to the incident angle. This reflected beam is often called specular component. The relationship between its intensity and the RMS roughness of the surfaces was derived from electromagnetic wave scattering theories and was also first experimentally verified by Bennett and Porteus (1961). In their pioneering experiment, an infrared illumination was directed at the normal incident angle to the surface. The measured intensity was established as:

$$I_s = I_0 \exp\left[-\left(\frac{4\pi R_g}{\lambda}\right)^2\right] \quad (1.1)$$

where λ denotes the illumination wavelength and I_0 is a constant depending on the sample material. This work was later extended to an incident angle of 20° by Depew and Weir (1971).

The reflectance of white light from the surface was correlated to the surface roughness amplitude and surface slope by Sakai and Sawabe (1982). In a similar study, Spurgeon and Slater (1974) used fiber optics for transmitting to and receiving light from turned surfaces. Inasaki (1982) later applied this method to measure surface roughness in a grinding operation. The sensitivity of this method was subsequently improved by North and Agarwal (1983) by utilizing the ratio of the specular to diffused component

scattering angle of 35° . It is observed that these techniques established an empirical relationship between the optical parameter and a roughness parameter, usually R_q . As the optical parameter (e.g. reflectance) is not only dependent on surface roughness but also on other factors such as material electrical properties, method of processing, etc., new calibrations are required for different materials and different processes. There is still a lack of a theoretical model to explain and predict the effect of these factors on these calibration curves.

The scattering of coherent light from very smooth surfaces can be approximated by a diffraction from phase gratings. The diffraction pattern at the far field or at the back focal plane of a lens is approximately proportional to the Fourier transform of the surface heights. This phenomenon is commonly known as the Optical Fourier Transform (OFT) which was the subject of study for various investigators. A comparison between the scattering pattern and the Power Spectral Density (PSD) of a surface height function was made in many works which include Stover (1975), Thwaite (1979), Hingle and Rakels (1983), and Huynh et al. (1991). From this comparison, a number of parameters were derived and proposed for use in surface roughness characterization. Roughness measuring instruments, based on the optical Fourier transform, are commercially available (Mansfield, 1992). For optical surface applications, there are two commonly accepted methods of measurement of scattered light: Total Integrated Scatter (TIS) and Bidirectional Reflectance Distribution Function (BRDF). TIS is defined by the ratio of the total sum of diffuse components to total scattered light, which is related to the surface roughness parameter R_q by:

$$\text{TIS} = \left(\frac{4\pi R_q}{\lambda}\right)^2 \quad \text{for } R_q < \lambda \quad (1.2)$$

This is the most widely used technique because of its simplicity and traceability to the ASTM standard (Bennett and Mattsson, 1989). For smooth surfaces, the scattering pattern is related directly to the PSD of the surface height. As such, TIS is simply the measurement of area under the PSD curve which is proportional to the RMS roughness, R_q . Equation (1.2) provides a basis for the development of commercial scatterometers (TMA Technologies, 1991). The BRDF is defined by the ratio of the scatter power per unit solid angle to the incident power, which is another form of a normalized scatter intensity distribution (Stover, 1990). While TIS yields only the surface roughness amplitude information, the angular distribution (as defined by BRDF) can provide additional information about the surface texture. The following is a description of two approaches using the BRDF, or angular distribution of the scattering intensity to quantify roughness:

(a) Theoretical Approach

For Gaussian random surfaces, the standard deviation of the optical diffraction pattern (equal to the square root of the ratio of the second moment to the zeroth moment of the BRDF) was found to be proportional to the RMS surface slope (Rakels, 1988). From these results, the RMS slopes of various surfaces were obtained (Marx and Vorburger, 1990; Cao et al., 1991).

b) Empirical Approach

For machined surfaces which are normally rough, the scattering patterns do not display very dominant specular components. Therefore, it may not be possible to separate the specular from the diffuse components in the total distribution. The surface roughness parameters are usually correlated experimentally to some features of the scattering pattern (Cuthbert and Huynh, 1992; Kurita et al., 1992). One of the most often used scattering parameters is the second moment of the angular intensity distribution about its specular axis. This quantity, denoted by S_N (Broadmann and Thurn, 1986; Zimmerman et al., 1988) is related to the surface roughness slope. It should be noted that in these experimental works, however, there was little attempt to separate the influence of roughness from that of surface wavelength on the selected optical parameters. The experimental results from these works, therefore serve as a comparative surface roughness indicator rather than an absolute measurement.

Roughness measurement can also be developed based on the property of speckles which can be considered as a statistical aspect of light scattering pattern. Speckle appears as grainy patterns when a random surface is illuminated by a highly coherent light such as a laser. This pattern is caused by the random interference of light scattered from various depths of the surface. In one application, speckle contrast was measured at the image plane and correlated to roughness using samples up to $0.5 \mu\text{m } R_q$ (Fujii and Asakura, 1974). A similar trend was also found in the case where the speckle pattern was measured at the diffraction field (Ohtsumo and Asakura, 1975). In addition to roughness, this method can also yield an estimation of the correlation length from the speckle contrast versus illumination area curve. In general, the laser speckle measurement can

be carried out at a fairly fast speed using a relatively simple setup. However, its measurement output approaches a saturation level rapidly when the roughness is greater than the illumination wavelength. This restricts its application to ground surfaces or other surfaces of medium to low roughness. Recently, an attempt was made by Shiraishi and Sato (1991) to increase the measurement range from $3.0 \mu\text{m}$ to $70 \mu\text{m}$ R_a . However, because of the low sensitivity obtained, the technique is not likely to be of practical use. Another roughness measurement method utilizes the correlation analysis of speckle images created by two light sources (or two specklegrams taken under different incident angles) (Ruffing, 1986). This method has the advantage of having an adjustable measurement range which is not limited by the illumination wavelength. However, the process is much more involved than the contrast calculation technique. In addition, it requires the same environmental stability (minimum vibration) as interferometry. Therefore, it may not be feasible for use in manufacturing processes.

Techniques based on light scattering measurement give only average parameters. Nevertheless, reconstruction of surface profiles from their scattering data has been an ultimate goal of many theoretical scattering research. So far only the solution for certain periodic surfaces, namely, optical gratings was obtained (Aas, 1972; Sasaki and Fukuhara, 1985). Since the surface profile information is modulated through the phase of scattered light, this class of problem is referred to as phase retrieval problems (Fienup, 1982). The solution requires an accurate measurement of the scattering distribution and an application of the iterative numerical algorithm (Roger and Maystre, 1980).

In light scattering techniques, the measured roughness range is normally determined by the illumination wavelength. As He-Ne lasers ($0.633 \mu\text{m}$) are often used for light sources, these techniques are limited to a roughness range less than a fraction of this value. This range coincides with the roughness of optical surfaces which explains the feasibility of these techniques for optical roughness measurement. By using longer wavelength lasers, sensors based on these techniques (TIS, BRDF) can be adapted to measure machined surfaces which are one order of magnitude rougher than optical surfaces (Janson et al., 1984; Thwaite, 1982). As the detectors for long wavelengths are rather expensive, because of the cooling requirement, this application does not go beyond the walls of the research laboratories.

In summary, optical techniques, thanks to the readily available and inexpensive components, are advancing rapidly. Interferometric devices and optical profile probes can provide surface profile data at a fairly high resolution, however, the high investment cost combined with the vulnerability to the environment make them unsuitable for in-process applications. In contrast, light scattering based devices are more rugged, simple to set up, and can withstand the vibration of machines on the production floor. However, most devices developed to date are applicable to optical surfaces and only a few are fully implemented in a production environment.

The type of machining processes that produces the surface is also an important consideration in the design or the selection of sensors for roughness measurement. Machined surfaces can be classified as random or periodic or a combination of both. Ground surfaces are mostly random while turned and milled surfaces are more periodic. Even though grinding is of general interest in roughness sensing research, more attention

is paid to turning as it is more often used in production industries. Most light scattering techniques were developed for ground surface applications. Similar setups were used for measuring turned surfaces regardless of the shape and the periodic nature of the workpiece (Shiraishi, 1981, 1987; Jansson et al., 1984). In most investigations, the illumination plane or incident plane, defined by the incident beam and the surface normal, was perpendicular to the lay.

1.3 Light Scattering Theory

Surface roughness estimation using light scattering is an inverse problem of prediction of light scattering from a given surface. The prediction of light (or wave) scattering from rough surfaces has been a subject of investigation in various disciplines, for instance, acoustics, electromagnetic waves propagation, and radiative heat transfer. During the past three decades, a large amount of work on rough surface scattering, both theoretical and experimental was carried out. Various scattering models have been developed for predicting the scattering phenomena (Bennett and Mattsson, 1989). In the model development, various assumptions were made in order to simplify the analytical work. Following are some of the important models.

(a) Geometrical optics model

This model is applicable to rough surfaces whose roughness amplitude is much greater than the illumination wavelength. The surface topography is thought of as a collection of planar micro-facets whose slopes are assumed to be normally distributed. This model was used mainly in remote sensing, heat transfer, and computer vision

studies (Nayar et al., 1991). This model can provide a good approximation to the cases where the effect of diffraction is negligible. As such, this model is not adequate for predicting light scattering from machined surfaces where the effect of light wave diffraction cannot be ignored. Even though it is not suitable for quantifying scattering from machined surfaces, it is still used to provide a first approximation to shadowing and multiple scattering (Beckmann, 1965).

(b) Phase grating theory

This theory was first systematically developed by Ratcliffe (1956) in which the wave nature of light was considered. A solution for the scattering amplitude was approximated by a Fourier transform using the assumption that the surface roughness is well below the illumination wavelength. As most optical surfaces satisfy this condition, this theory has been widely used in optical surface characterization. Light scattering methods, such as TIS and BRDF, can be derived from this theory.

(c) Beckmann's theory

This model was developed in the 50's and 60's based on the Kirchhoff approach of solving the wave equations using approximated boundary conditions. It was originally used in radio engineering and later on in radar application. In general, its solution offers a better accuracy than that from the phase grating theory mentioned above. The basic theory was treated in a monograph by Beckmann (1963, 1967). This is the approach used in this work and will be discussed in detail later.

(d) Other approaches

A mathematically more rigorous approach based on minimization of energy was proposed first by Rayleigh (Beckmann, 1965). This method is applicable to surfaces having sharp corners, and in theory, it possesses better accuracy than the others. Since it is mathematically much more involved than other models, the method is very seldom used in practical measurements. Vector models include the polarization properties of light. Their application, however, is limited to gratings of very short wavelengths where the polarization effect cannot be ignored (Elson and Bennett, 1979). More recently, an Integral Method developed by Saillard and Maystre (1990) is considered the most complete and accurate solution for rough surface scattering. This method takes into account the complex phenomena of multiple scattering and shadowing which is completely ignored in other models. This method, however, is fairly complex and some simplification is required before it can be exploited in surface measurement application.

(e) Numerical techniques

With the availability of fast computing techniques, there is an increasing trend for the use of numerical simulations for solving scattering problems. For well defined surfaces such as simple sinusoidal or triangular periodic surfaces and random surfaces with normal or exponential distribution, an analytical solution can be obtained from scattering models such as the Beckmann's. However, for more complex surfaces, the derivation of an analytical solution is very difficult if not impossible. Thus, a numerical integration has to be performed instead. For example, for non Gaussian random surfaces,

a Monte Carlo simulation was used to obtain statistical parameters of the scattered fields (Ogilvy, 1991).

1.4 Turning Surface Profile Generation

In this section, a description of the surface profile geometry obtained from a turning process is given. This will serve as a justification in the modelling of the profile for this process.

In ideal turning, where the vibration and machining errors are not taken into account, the surface profile is defined by the cutter geometry and its feed motion as shown in Figure 1.2. For a circular tool with a nose radius r_n , the average roughness, R_a , is given by (Shaw, 1984):

$$R_a = \frac{f^2}{32r_n} \quad (1.3)$$

where f is the feed rate.

The Peak-to-Valley roughness, R_p , for this tool geometry is:

$$R_p = \frac{f^2}{8r_n} \quad (1.4)$$

From the two expressions given above, it is seen that the surface roughness is determined by the feed rate and tool geometry.

In actual turning, the surface finish is also dependent on other factors such as spindle rotation accuracy, tool material, cutting speed, and workpiece material, etc. (Shaw, 1984). The effect of various operating conditions on roughness was studied by many

investigators, particularly by Whitehouse et al. (1974). In general, turned surfaces, whose characteristics are determined by the feed component of the cutting process, are mainly periodic. Random components also exist on the turned surface. They are caused by such as machine vibrations or tool/workpiece movement. As they are relatively small in amplitude, they have minor effect on the average roughness. For a given cutter geometry, the turned surface profile can be approximated by its surface amplitude and surface wavelength.

1.5 Objectives

From the previous discussion, it is recognized that there is a great need for surface finish control in machining. This requires the development of a technique with an in-process capability for machined surfaces especially for turned surfaces. The following are the objectives set out for the work presented in this dissertation:

1. To investigate the scattering of light from machined periodic surfaces where the roughness amplitude is greater than the illumination wavelength. The Beckmann model is used and numerical integration is performed to obtain the scattering pattern. The model will provide a basis for the understanding of the light scattering phenomenon from these surfaces.
2. To apply the scattering model to the case where the illumination plane is parallel to the lay of the surface. This scattering configuration offers the advantage of minimizing shadowing and multiple scattering which simplifies the model.

3. To extend the scattering model from the flat surface to cylindrical surfaces. This is to predict the light scattering pattern from turned surfaces and verify the validity of the model by scattering measurements.

4. To develop a surface roughness measurement technique for turned surfaces for in-process application. This method should have the capability of measuring both the surface wavelength and roughness.

Chapter 2

Beckmann's Model

In this chapter, first a brief description of Beckmann's formulation is given together with the explanation of notations which will be used throughout the thesis. This is followed by a derivation of a general solution for periodic surfaces and also for Gaussian random surfaces. Finally, a concept of a two-scale model which involves the superposition of a small random component on the main periodic profile is introduced. This is then followed by a qualitative analysis of the scattering from this model.

2.1 General Scattering Formula

Solving light scattering problems generally involves obtaining a solution to the wave equation subjected to a set of boundary conditions. These boundary conditions are defined with respect to the rough surface and the free space surrounding the surface. Applying the Green's Theorem, the scattered field can be expressed by a surface integration known as the Helmholtz integral. Beckmann's model originated from the Kirchhoff's approach in approximating the electrical field and its normal derivative at a

point on the surface by an equivalent field on its tangential plane. Following are a summary of the results:

When a light beam is incident on a rough surface, it is scattered into different directions. For a scattering geometry shown in Figure 2.1, the scattering coefficient, ρ , is defined in the Beckmann's model for a two-dimensional rough surface by (For more details on the development of the formulation, see Beckmann, 1963):

$$\rho = \frac{F}{A} \iint \exp(i\mathbf{v}\cdot\mathbf{r}) dx dy \quad (2.1)$$

where \mathbf{v} is a vector describing the difference between the incident and the reflected wave vectors, and is given as:

$$\mathbf{v} = k[(\sin\theta_1 - \sin\theta_2 \cos\theta_3)x_0 - \sin\theta_2 \sin\theta_3 y_0 - (\cos\theta_1 + \cos\theta_2)z_0] \quad (2.2)$$

\mathbf{r} is the position vector, given by

$$\mathbf{r} = xx_0 + yy_0 + \zeta(x,y)z_0 \quad (2.3)$$

and F is a geometrical factor defined by:

$$F = \frac{1 + \cos\theta_1 \cos\theta_2 - \sin\theta_1 \sin\theta_2 \cos\theta_3}{\cos\theta_1 (\cos\theta_1 + \cos\theta_2)} \quad (2.4)$$

The normalized amplitude of the scattered field, ρ , is in general a complex quantity. $\zeta(x, y)$ is the surface height function which is equal to zero at the mean surface plane. Others are defined as follows:

$k=2\pi/\lambda$, which is the wave number, defined in terms of λ , the illumination wavelength,

θ_1 = angle of incidence,

θ_2 = scattering angle,

θ_3 = angle of lateral scattering,

A = illuminated area

x_0 , y_0 , and z_0 are unit vectors in the x -, y -, and z - directions, respectively.

The major assumptions made in this derivation include: (1) The light beam is a coherent plane wave; (2) The scattering field of interest is far from the scattered surface, namely, in the far field or Fraunhofer region; (3) The surface has a continuous, gently rolling slope which prevents any shadowing and multiple scattering; and (4) the surface is perfectly conducting.

The intensity I , a measurable quantity, can be calculated from $\rho\rho^*$, where ρ^* is the complex conjugate of ρ .

It can be observed from Equation (2.1) that only the phase of the reflected wave is modulated by the surface roughness. The integration process involved here is similar to a two-dimensional Fourier Transform. The geometrical factor F is a geometrical weight function which modifies the angular distribution of the scattering energy to take into account the oblique incidence; it is equal to unity for normal incidence. An analytical solution for Equation (2.1) can be derived if the surface height functions are well defined

simple functions. For complex profiles, however, a numerical integration has to be performed.

2.2 Solution for Periodic Surfaces

Consider a periodic surface height function $\zeta(x, y)$ with surface wavelengths Λ_x and Λ_y in the direction x and y , respectively. For this surface to be periodic, it must satisfy the following condition:

$$\zeta(x, y) = \zeta(x + \Lambda_x, y + \Lambda_y) \quad (2.5)$$

The result of the integration of Equation (2.1) is periodic if the following conditions are met:

$$\sin \theta_{2mn} \cos \theta_{3mn} = \sin \theta_1 + m \frac{\lambda}{\Lambda_x} \quad (2.6)$$

and

$$\sin \theta_{2mn} \sin \theta_{3mn} = n \frac{\lambda}{\Lambda_y} \quad (2.7)$$

where m and n are integers representing the scattering mode or scattering order. A given (m, n) pair corresponds to a particular scattering mode. The total number of scattering modes are determined by the ratio Λ/λ and the angle of incidence θ_1 . These equations are normally referred to as grating equations for two dimensional periodic surfaces.

By ignoring the edge effect, the integration of Equation (2.1) can be carried out within one wavelength (or period) limit to yield the amplitude of each individual scattering mode specified by m and n :

$$\rho = \frac{F(\theta_1, \theta_{2mn}, \theta_{3mn})}{\Lambda_x \Lambda_y} \int_0^{\Lambda_x} \int_0^{\Lambda_y} \exp(i\nu\tau) dx dy \quad (2.8)$$

As indicated previously in Chapter 1, most investigations on light scattering only considered the cases where $m=0$. This corresponds to a scattering geometry where the illumination (incident) plane is perpendicular to the lay which is the commonly used geometry for optical gratings. A polar plot of the scattering intensity for this case is shown in Figure 2.2. The other particular case of interest is when $n=0$ where the incident plane is parallel to the direction of the lay. Although this is not a commonly used geometry, it will be shown later that this geometry is of great importance in the application of roughness measurement for machined surfaces. The scattering from the two geometries ($m=0$ and $n=0$) specified above will be considered in details in the following chapters.

2.3 Solution for Random Surfaces

Random surfaces are not deterministic, therefore, cannot be described by a profile height function. A statistical description is required instead, for the surface characterization. Once this is given, the statistical parameters for the scattering field are derived to quantify the scattering. Analytical solutions for scattering from random

surfaces can be derived for simple distributions such as Gaussian. Let the surface height, ζ be a random variable which is distributed normally with zero mean, i.e. $\langle \zeta(x,y) \rangle = 0$, and a variance, σ . The probability distribution, $p(z)$, of the surface height ζ is governed by:

$$p(z) = \frac{1}{\sigma\sqrt{2\pi}} \exp\left(-\frac{z^2}{2\sigma^2}\right) \quad (2.9)$$

The autocorrelation coefficient function, $C(\tau)$, of the surface height is also assumed to be of a Gaussian form, i.e.:

$$C(\tau) = \exp\left(-\frac{\tau^2}{T^2}\right) \quad (2.10)$$

where τ is a spatial variable and T is the correlation distance or correlation length.

For the Beckmann's model to be valid, the following conditions are imposed: $T \gg \lambda$ and $(\sigma/T) \ll 1$. The mean scattering intensity along a given direction is derived as (Beckmann, 1963):

$$\langle I \rangle = \langle \rho \rho^* \rangle = \exp(-g) \left[\rho_0^2 + \frac{\pi F T^2}{A} \sum_{m=1}^{\infty} \frac{g^m}{m! \sqrt{m}} \exp\left(-\frac{v_{xy}^2 T^2}{4m}\right) \right] \quad (2.11)$$

where A is the illuminated area, and g is the roughness parameter defined by:

$$g = \left[2\pi \frac{\sigma}{\lambda} (\cos\theta_1 + \cos\theta_2) \right]^2 \quad (2.12)$$

V_{xy} is the amplitude of vector V :

$$v_{xy} = \sqrt{v_x^2 + v_y^2} \quad (2.13)$$

ρ_0 is the scattering coefficient of a rectangular plane having a surface area, $A=XY$. It is defined as follows:

$$\rho_0 = \frac{\sin v_x X}{v_x X} \cdot \frac{\sin v_y Y}{v_y Y} \quad (2.14)$$

v_x and v_y are the x and y components of v 's as defined in Equation (2.2). Approximations can be made to reduce Equation (2.11) to a simpler form for easy calculation. Solutions were obtained for the following cases: slightly rough surfaces, $g \ll 1$, moderately rough surfaces, $g \approx 1$, and very rough surface, $g \gg 1$. For example, the expression for a slightly rough surface is given as (Beckmann, 1965):

$$\langle I(\theta_1, \theta_2, \theta_3) \rangle = \exp(-g) \left[\rho_0^2 + \frac{\pi F T^2}{A} \exp\left(-\frac{v_{xy}^2 T^2}{4}\right) \right] \quad (2.15)$$

Equation (2.15) describes a simple bell-shape curve with the roughness g governing its sharpness. The first term in the square bracket represents the specular

intensity. It is the same as Equation (1.1) except lacking a material constant. This term decreases rapidly to zero at directions away from the specular direction. The second term contains a large portion of the diffuse components. For Gaussian surfaces, the RMS of surface slopes was found to be equal to $(2\sigma/T)^{0.5}$. This is a useful relationship for obtaining the surface slope information from scattering measurement (Bennett and Porteus, 1961).

2.4 Two-scale Surface Scattering Model

Real machined surfaces such as turned and milled surfaces can be approximated by periodic functions because they have a dominant periodic component. However, there always exists some additional random components which arise due to some disturbances during the cutting operation or due to material inhomogeneity. For a better approximation of the real surfaces, a concept of a two-scale surface model is introduced.

The two-scale surface model is defined as a super-position of a primary periodic component, ζ_p , and a secondary Gaussian random component, ζ_r . The former has a much longer wavelength and a much greater roughness height than those for the latter, i.e. $\Lambda \gg T$ and $H \ll \sigma \Lambda$, where σ is the RMS roughness and T the correlation length of the Gaussian random surface.

Under the above conditions, the scattering process of the two-scale surface model can be analyzed by using a phase grating analogy. In the phase grating, the angular distribution of the scattering pattern at the far field is a Fourier transform of the phase change due to a surface roughness amplitude variation. The scattering patterns from these

surfaces are known, Equation (2.8) for periodic surfaces and Equation (2.11) for random surfaces. Let the resultant surface roughness be written as:

$$\zeta = \zeta_p + \zeta_r \quad (2.16)$$

Substituting this into Equation (2.1), two multiplication terms will be produced in the integral, one is associated with the primary, the other random surfaces. According to the Convolution Theorem (Goodman, 1968), the scattering field of the two-scale model will thus be a convolution of the two scattering fields produced by each individual component. This transformation procedure is illustrated in Figure 2.3. From this transformation, it can be observed that the effect of adding random components is simply applying a weight function to each of the scattering modes. Thus, small random components tend to reduce the peak intensity of the scattering modes. In addition, increasing the surface wavelength of the random components will have the effect of making the scattering modes less discrete, i.e. scattering intensity distribution is more continuous. The above simple analysis offers a qualitative explanation of how the random component affects the scattering of periodic surfaces. If the random component is relatively small, this effect can be neglected. Otherwise, a more rigorous analysis must be made. The solution for this would be complex because the scattering intensity given by Equation (2.1) is not an exact Fourier transform of the surface roughness height and a statistical average is performed before the integration for the random surface. In light of this, the convolution analogy serves as an illustration of the interaction of the two components of the surface.

Chapter 3

Numerical Analysis of Scattering from Periodic Surfaces

In this chapter, the Beckman's model will be used to derive numerical solutions to study the light scattering from periodic surfaces. The surfaces considered in this work are those with surface roughness amplitudes comparable to (and greater than) the illumination wavelength, and also those with surface spatial wavelengths within the range of regular turned surfaces. Four different one-dimensional surface profiles will be used in the calculations and the effect of profile geometry on scattering will be assessed. Scattering experiments will also be carried out to verify the results. Based on the finding of the investigation, a surface roughness estimation method is proposed.

3.1 Beckmann's model

Consider a scattering geometry where the direction of the incident beam is perpendicular to the lay of a one-dimensional periodic surface, Figure 3.1. The reflected beam in this case, is scattered into an angular distribution of discrete components which are confined to the same plane, namely the plane of incidence (which is the plane of the paper in Figure 3.1). As there is no lateral scattering (i.e. $\theta_3=0$ in the grating equations),

the angular locations of the peaks can be determined from a single, simplified grating equation:

$$\sin\theta_{2m} = \sin\theta_1 + m\frac{\lambda}{\Lambda} \quad (3.1)$$

where

m = scattering or diffraction order, $m=0, \pm 1, \pm 2, \pm 3, \dots$

λ = the wavelength of the incident light

Λ = the spatial wavelength or period of the surface

θ_1 = the incident angle

θ_2 = the scattering angle

The normalized amplitude (ρ) at a given direction θ_2 can be derived from Equation (2.8) as:

$$\rho(\theta_2) = W \sec\theta_1 \frac{1 + \cos(\theta_1 + \theta_2)}{\cos\theta_1 + \cos\theta_2} \frac{1}{\Lambda} \int_{-\Lambda/2}^{\Lambda/2} \exp(i\phi(x)) dx \quad (3.2)$$

where

$$\phi(x) = \frac{2\pi}{\lambda} [(\sin\theta_1 - \sin\theta_2)x - (\cos\theta_1 + \cos\theta_2)\zeta(x)] \quad (3.3)$$

and

$$W = \frac{\sin(2qp\pi)}{2qp\pi} \quad (3.4)$$

The parameters, p and q , in Equation (3.4) above are defined by:

$$p = \frac{\Lambda}{\lambda} (\sin\theta_1 - \sin\theta_2) \quad (3.5)$$

$$q = \frac{\text{footprint length}}{\text{surface wavelength } \Lambda} \quad (3.6)$$

and $\zeta(x)$ is the surface height function which is assumed to be one dimensional. All the dimensional variables including the surface height $\zeta(x)$ and the surface wavelength Λ can be normalized with respect to the illumination wavelength λ . As such, the scattering pattern can be quantified and analyzed directly in terms of these normalized parameters.

3.2 Numerical Procedure

Four different surface profiles were selected to represent typical surfaces produced by a single cutter tool similar to those obtained in turning or milling processes. These are sinusoidal, triangular, half-sine and cusp profiles. Numerical results are obtained for the scattering intensities of these profiles which are defined as follows:

Sinusoidal surface profiles:

$$\zeta(x) = 0.5H \cos\left(\frac{2\pi}{\Lambda}x\right) \quad -\frac{\Lambda}{2} \leq x \leq \frac{\Lambda}{2} \quad (3.7)$$

(Note that an exact solution for peak value obtained by integrating Equation (3.2) for the sinusoidal surface is given by (Beckmann, 1963):

$$\rho(\theta_{2m}) = \frac{1 + \cos(\theta_1 + \theta_{2m})}{\cos\theta_1(\cos\theta_1 + \cos\theta_{2m})} (-1)^m J_m \left[\frac{\pi H}{\lambda} (\cos\theta_1 + \cos\theta_{2m}) \right] \quad (3.8)$$

where J_m is the Bessel function of the first kind and m order).

Triangular surface profiles :

$$\zeta(x) = \begin{cases} \frac{2H}{\Lambda}x & 0 < x < \frac{\Lambda}{2} \\ -\frac{2H}{\Lambda}x & -\frac{\Lambda}{2} < x < 0 \end{cases} \quad (3.9)$$

Half-sine profile:

$$\zeta(x) = H \cos\left(\frac{\pi}{\Lambda}x\right) \quad -\frac{\Lambda}{2} \leq x \leq \frac{\Lambda}{2} \quad (3.10)$$

Cusp surface profiles:

These profiles resemble the case for ideal turning with a circular tool nose radius as shown in Figure 1.1:

$$\zeta(x) = R - \sqrt{R^2 - x^2} \quad (3.11)$$

where R is the radius of the cusp profile, which is given by:

$$R = \frac{\Lambda^2}{8H} + H \quad (3.12)$$

For illustration, the curves of the above four profiles are super-imposed on a graph as shown in Figure 3.2. In this Figure, H denotes the peak to valley height. It should be noted that in the integration, these profiles are shifted vertically so that they all have a zero mean value for the period. The period Λ for these profiles is fixed at 30 μm and the illumination wavelength is equal to 0.633 μm (He-Ne laser).

The numerical integration of Equation (3.2) was carried out on an IBM computer using FORTRAN subroutines from IMSL library. The relative accuracy was set at 1% which defined the criteria for convergence. This accuracy was later determined for a sinusoidal profile by comparing these results with those obtained by the analytical solution given by Equation (3.8). Excellent agreement was observed. In carrying out the integration, the step size was adjusted according to the value of roughness H and the period Λ . Smaller stepsizes, however, must be used for larger H and Λ to maintain convergence of the numerical process.

3.3 Results and Discussion

Numerical results are plotted as shown in Figures 3.3 to 3.9. The discussion will be focussed first in the general behavior of light scattering and then shifted to the particular functional relationships between the scattering pattern and the surface profile parameters.

3.3.1 Light Scattering Pattern

From the numerical results of the scattering of the four surface profiles, Figure 3.3 and 3.4, it is observed that the light scattering pattern, in general, is unique for any given surface profile. This pattern varies as the roughness changes. However, it can generally be grouped into two types or regimes: smooth and rough regimes, each with different scattering characteristics.

In the smooth regime where $H < 0.2 \mu\text{m}$, i.e. $(H/\lambda) < 0.31$, most scattering energy is directed toward the specular direction as dictated by Snell's law (Figure 3.3a). In this roughness region, the scattering patterns from the four profiles are similar in that they are characterized by predominant specular components with peak intensities. These are surrounded by diffused components of decreasing amplitudes at increasing scattering orders. At the very smooth surface limit, the results are the same as those obtained via the phase grating model.

In the rough regime where $H < 0.2 \mu\text{m}$, i.e. $(H/\lambda) < 0.31$, the scattering is characterized by a growth of diffused components at the expense of the specular counterparts. This is evidenced in the shifting of major scattering peaks away from the specular direction. The scattering pattern in this roughness region is strongly dependent

on the surface profile and the scattering geometry (Figures 3.4a,b, and c). For very rough surfaces, the scattering pattern is largely determined by the surface slopes. For the case of a simple triangular profile, the scattering pattern in Figure 3.4a contains two main components which could be identified as a reflection of the specular beam from two sides of the triangular surface. This indicates that numerical solution approaches the geometrical optics model in this roughness range. Experimental results by Allardyce and George (1987) with diffraction gratings in this roughness range showed a similar shape to the scattering pattern shown in Figure 3.3b.

A closer examination of the scattering patterns reveals that the individual component has the shape of a lobe which is modulated by a sinc function defined by Equation (3.4). The spacing between adjacent lobes is determined by the ratio of the illumination footprint to surface wavelength. Lobe overlapping will occur if this ratio is small. To prevent this, a minimum ratio of 5 is required. This value can be used as a set-up guide in scattering measurements to identify individual components.

Note that the above results are valid for an incident angle of 45° . If the incident angle is reduced to zero, the roughness transition point will occur at a roughness amplitude H slightly less than $0.2 \mu\text{m}$. The overall shape of the scattering pattern, however, would be the same as before.

3.3.2 Component Intensity versus Incident Angle

The incident angle plays a major role in determining the behavior of the scattering pattern in the rough regime of scattering. To study this effect, the specular intensity reflecting from a given profile was first calculated for different incident angles. This was

repeated for different roughness amplitudes. The results for sinusoidal surfaces are shown in Figure 3.5. This procedure was repeated for other profiles and the results are shown in Figures 3.6 to 3.8.

It was observed that, in general, the graphs for different profiles of the same roughness are similar. For small roughness amplitudes, the intensity-incident angle curve increases monotonically as the incident angle increases. At large roughness amplitudes, however, the curve oscillates and the frequency of oscillation increases as the roughness increases. This fluctuation is caused by the light path difference between the peaks and valleys of the given surface profile. When the path difference is a multiple of $(\lambda/2)$, an intensity cancellation by interference takes place. Similar observations can be found in the work of Bass and Fuks (1979) for sinusoidal surfaces of random phases. In this case, the reflection coefficient of a transparent plate oscillates as the thickness of the plate changes. This oscillation behavior of the scattering peaks was also observed by Allardyce and George (1987).

It should be noted that for sinusoidal and triangular surfaces, the local minimum in the intensity-versus-incident angle curves is zero for the specular components. This is not true for the other two profiles. The reason for this difference might be that for these two surfaces, the profile is not symmetrical with respect to the mean plane.

The above observations are applicable to the specular components. Similar observations can be made with any other scattering order, for example, the $m=-1$ order shown in Figure 3.9, except that at the near zero grazing angle, the intensity decreases as the incident angle increases. This is also true of all the other three profiles. It should be pointed out that, as the Beckmann's model assumes no shadowing, the results calculated

at an incident angle close to 90° are not quite meaningful in a physical sense. Further improvement may be made by modifying the model using the Beckmann's approach which takes into account the shadowing effect (Beckmann, 1965).

3.4 Experimental Evidence

Two standard samples having $R_a=0.5 \mu\text{m}$ and $3 \mu\text{m}$, respectively, were used in the experiment to verify the numerical results. There are periodic profiles with symmetrical triangular shapes. Their stylus profiles and the Fourier spectra are shown in the Figure 3.10. As it can be seen from these figures that only very small random components are present, they can be neglected in the analysis.

3.4.1 Experiment Setup and Procedure

Figure 3.11 shows the experimental setup for light scattering measurements. It consists of two arms which are pin-connected co-axially so that they can rotate independently around the same center. A laser diode was mounted on one arm and a photo detector on the other. The photo detector has a sensing area of $1 \times 1 \text{ mm}$ and is at 0.1 m distance from the rotation center. The roughness sample was placed on a horizontal plane passing through the axis of rotation of the arms. The laser diode was focused on the surface to a spot size approximately equal to a few millimeters in diameter. The resulting pattern on the detector plane was roughly 4 mm in size (typical). The output of the photo detector was digitized and measured using a data acquisition system. The inclination angles of the laser and detector were measured by a protractor with a resolution of 1° .

Two sets of experiments were carried out:

- a) determination of the angular distribution of scattering for a fixed incident angle and
- b) establishment of the relationship between the intensity of the scattering component and the incident angle.

3.4.2 Experimental Results and Comparison with Prediction

(a) Figure 3.12a is a plot of the angular distribution for sample A with the laser set at 60° incident angle. The pattern contains a number of discrete peaks, each corresponding to a scattering order as shown. The dominant peaks tend to concentrate around the vicinity of 10° scattering angle.

Numerical results were obtained to predict the scattering from a surface realization with the texture parameters similar to those of sample A. The results are superimposed on the experimental data for the scattering orders from $m=-4$ to $m=2$ as shown in Figure 3.12b. In a comparison between the two results, it can be observed that they, in general, have the same trend for the low scattering orders ($m=\pm 2$). For higher scattering orders, however, there are some large discrepancies. These discrepancies may be attributed mostly to the effect of multiple scattering which occurs at large scattering angles that were not accounted for in the model.

(b) Figure 3.13 shows a graph of the variation in intensity of the specular component of sample A when the incident angle is varied. On this graph, the experimental measurements and the numerical results are super-imposed for comparison. A similar oscillating characteristic can be observed in both results. However, there are

some discrepancies in the absolute magnitudes of the two curves. These errors can be attributed to the multiple scattering effect when large incident angles are used.

An attempt was made to measure the scattering intensity for Sample B. A photograph of the scattering pattern is shown in Figure 3.14. In this figure, there are a series of discrete bright spots which are aligned parallel to the direction of the incident plane. However, as the scattering intensity was too low to be measured by the detector, no data was obtained.

A scattering pattern of a turned sample with roughness of $0.3 \mu\text{m } R_a$ is shown in Figure 3.15. In this set up, an incident angle of 5° was used. It is seen, in this figure, that the scattering pattern contains a number of discrete dots (produced from the periodic components) super-imposing on a continuous distribution which arises from its random components. As such, the presence of the random components on the turned surfaces will make the evaluation of the pattern more complicated. To make the present model applicable to these surfaces, some measure has to be taken to reduce the influence of the random components.

3.4.3 A Proposal for Surface Roughness Estimation

The variation of individual component intensity with respect to incident angle is, as observed above, an indication of the phase difference between peaks and valleys of a profile. Therefore, by determining the associated phase differences, a roughness assessment can be carried out. First the relationships between component intensity versus incident angle can be established from numerical calculations (using the model) for

different surfaces of known profiles. These relationships can then be used for the estimation of surface roughness.

The method of roughness assessment as proposed, is similar to interferometric techniques in a sense that the illumination wavelength is used as a reference and that it does not rely on the absolute intensity value. This is more favorable compared to other types of reflection measurements where the results depend strongly on the types of workpiece materials.

Another important factor one must consider here is the surface wavelength. As indicated by Equation (2.1), this factor, represented by the ratio Λ/λ , determines the angular spacing between the adjacent scattering components. Although this does not directly influence the intensity characteristics of the surfaces, it affects the measurement accuracy. To facilitate the scattering intensity measurements, care must be taken to ensure reasonable component separation when measuring surfaces of long wavelengths. To achieve large component separation, a large incident angle must be used. It should be noted, however, that as the incident angle approaches 90° , shadowing and multiple scattering will be present, and this will nullify the model.

3.5 Summary

Following are some of the remarks derived from this chapter:

(1) The scattering behavior was observed to be dependent on the shape of the surface profiles and the incident angles. Two scattering regimes were identified: smooth surface scattering characterized by large specular components, and rough surface scattering indicated by the growth of the diffuse components in combination with strong

back scattering. This kind of behavior cannot be either predicted by geometrical optics or by the phase grating model based on the optical Fourier transform.

(2) The scattering patterns from different surface profiles are significantly different for very rough surfaces where the solutions approach those obtained by geometrical optics.

(3) The scattering intensity of the individual scattering component versus the incident angle curve was found to be uniquely related to surface roughness. Based on this property a new procedure for estimating periodic surface roughness was proposed.

(4) An oscillation behavior is observed when either the roughness or incident angle changes. However, only in the latter case, is there a change in the number of the scattering peaks.

(5) The preliminary experimental results on the scattering peaks showed that they have similar trends to those from the model's prediction for the lower order scattering components. The model was not verified for high order components.

(6) A measure to suppress the effect of random components has to be taken to facilitate the scattering measurement of actual turned surfaces.

The current scattering measurement configuration with an incident plane perpendicular to the lay does not permit the usage of large incident angles as this will produce shadowing and multiple scattering. To overcome this limitation, an illumination parallel to the lay is proposed for the scattering measurements. This is the subject of study for the next chapter.

Chapter 4

Light Scattering from Flat Periodic Rough Surfaces

In this chapter, the Beckmann's scattering model is applied to periodic surfaces for the case where the incident plane is parallel to the lay. Numerical results were obtained for sinusoidal and triangular surface profiles. These were used for analyzing the effect of surface wavelength and roughness on scattering properties. Experimental work was subsequently performed to verify the model and determine its accuracy.

4.1 Scattering Model

Consider a scattering geometry shown in Figure 4.1. Applying the periodic surface scattering given by Equation (2.8) to one dimensional surface profile height, $\zeta = \zeta(y)$, we obtain the normalized scattering amplitude as:

$$\rho = \frac{F 2A \sin[k \sin \theta_1 - \sin \theta_2 \cos \theta_3]}{S k(\sin \theta_1 - \sin \theta_2 \cos \theta_3)} \int_{-\frac{\Lambda}{2}}^{\frac{\Lambda}{2}} \exp(i\Phi(y)) dy \quad (4.1)$$

where

$$\Phi = k[\sin\theta_2 \sin\theta_3 y - (\cos\theta_1 + \cos\theta_2)\zeta(y)] \quad (4.2)$$

S = Illuminated surface area having dimensions $(2A) \times (2B)$,

θ_1 , θ_2 and θ_3 are the incident, reflection, and azimuthal (lateral) scattering angles, respectively.

In contrast to the case considered in the last chapter, the scattered field is no longer contained in one plane. Thus, the additional lateral scattering angle, θ_3 , is needed to describe the scattered field.

For periodic surfaces, the scattering pattern consists of discrete components which can be identified as scattering (or diffraction) orders. The locations of these orders are given by the following grating equations:

$$\sin\theta_2 \cos\theta_3 = \sin\theta_1 \quad (4.3)$$

$$\sin\theta_2 \sin\theta_3 = m \frac{\lambda}{\Lambda} \quad (4.4)$$

where m is the scattering order which is finite for a given surface wavelength.

If the pattern is projected on a screen placed at a distance, D_x , from the rough surface as shown in Figure 4.2, the location of the scattering components on the screen coordinates is given by:

$$Y_s = D_x \tan \theta_3 \quad (4.5)$$

and

$$Z_s = D_x \cot \theta_2 \quad (4.6)$$

Equation (4.1) can be integrated once the surface profile function is defined. Let us consider the two special cases: sinusoidal and triangular profiles.

a) For a sinusoidal profile which is described by:

$$\zeta(y) = 0.5H \cos\left(\frac{2\pi}{\Lambda}y\right) \quad (4.7)$$

the resultant scattering amplitude derived from the integration of Equation (4.1) is:

$$\rho = F i^m J_m \left[(\cos \theta_1 + \cos \theta_2) \frac{\pi H}{\lambda} \right] \quad (4.8)$$

where J_m is the Bessel function of the first kind, m order.

b) For the triangular surface profile described by:

$$\zeta(y) = \begin{cases} \frac{2H}{\Lambda}y & 0 \leq y \leq \frac{\Lambda}{2} \\ -\frac{2H}{\Lambda}y & -\frac{\Lambda}{2} \leq y < 0 \end{cases} \quad (4.9)$$

the scattering amplitude is:

$$\rho_m = F \frac{s \sin\left(\frac{m\pi}{2} + s\right)}{\left(\frac{m\pi}{2}\right)^2 - s^2} \quad (4.10)$$

where:

$$s = \frac{\pi H}{\lambda} (\cos\theta_1 + \cos\theta_2) \quad (4.11)$$

The above solutions represent the individual scattering components which are a function of the incident angle (θ_1), the scattering angle (θ_2), the lateral scattering angle (θ_3), and the surface roughness amplitude (H).

4.2 Numerical Results and Discussion

Numerical results were obtained for the scattering from sinusoidal and triangular profiles. The scattering pattern consisted of a number of scattering orders whose peak intensities were predicted by Equations (4.8) and (4.10). These peaks were aligned along a circular path whose center was located on the Z_x axis. The location of these peaks was determined by the grating equations, namely, Equations (4.3) and (4.4).

a) Influence of surface roughness

The model was applied to sinusoidal profiles of different roughness heights ($H = 1, 2, 4, 8, 16 \mu\text{m}$) to study the effect of changing roughness amplitude. For these profiles, the surface wavelength remained constant ($\Lambda = 60 \mu\text{m}$). The results are shown

in Figure 4.3. For smooth surfaces, scattering was concentrated around the low order region (near the specular component). When the roughness amplitude increased, however, the scattered energy was diverted to the higher order scattering modes. Similar results were obtained for triangular profiles as shown in Figure 4.4.

b) Influence of surface wavelength

The surface wavelength had a direct influence on the spacings between the two neighboring diffraction modes. The horizontal and vertical spacings (ΔY_s and ΔZ_s in Figure 4.2) between the zero and the first orders, are given by:

$$\Delta Y_s = \frac{D_x \lambda}{\Delta \sin \theta_1} \quad (4.12)$$

and

$$\Delta Z_s = D_x \cot \theta_1 - D_x \sqrt{\frac{1 - (\lambda/\Delta)^2 - \sin^2 \theta_1}{(\lambda/\Delta)^2 + \sin^2 \theta_1}} \quad (4.13)$$

The relationships between the fringe spacings and the surface wavelength described by the above equations were illustrated in a plot shown in Figure 4.5. Both the horizontal and vertical spacing curves had similar trends in that they were inversely proportional to the wavelengths.

It should be noted that the horizontal spacings between different adjacent scattering orders are different for different order numbers; the higher the order, the

smaller the spacing. For small lateral scattering angles, however, these spacings could be approximated by a constant. This is indeed the case for most of the samples used in this experiment. This property, similar to multi-slit diffraction, can be used to quantify the spatial wavelength of a surface.

c) Intensity versus grazing angle

The intensities of the specular and the first order components were calculated for different grazing angles and the results were plotted in Figures 4.6 and 4.7, respectively. It was observed that the intensities - in both graphs - oscillated as the grazing angle changed. Even though there was a phase difference between the two sets of curves at zero grazing angle, the number of oscillations was the same for both of them for any given roughness. These oscillations were uniquely related to roughness; their numbers increased with the increase in roughness amplitude.

Those results are applicable to sinusoidal profiles. For triangular profiles, similar curves were obtained and the same characteristics were noted. These characteristics were also obtained for the case of incident plane perpendicular to the lay. Figures 3.5 to 3.9 (note the different angle used in the x-axis).

It should be noted that in the present configuration where the incident beam is parallel to the lay, the restriction imposed by the model when using large grazing angles (to avoid multiple scattering and shadowing) is less severe and can be easily accommodated here. This is illustrated by analyzing the scattering from a triangular surface using geometrical optics.

Let α be the surface slope of the triangular profile, and if the incident beam is

perpendicular to the lay, the constraint imposed on the incident angle is derived as (for details of the calculations, please refer to Appendix A):

$$\theta_1 + 3\alpha < 90^\circ \quad (4.14)$$

For $\alpha = 15^\circ$ for example (this is the case for the two standard samples), $\theta_1 < 45^\circ$ has to be satisfied.

If the incident beam parallel to the lay, the scattering geometry becomes (Appendix A, Case B):

$$\theta_{1e} = 90^\circ - \arcsin(\cos \alpha \cos \theta_1) \quad (4.15)$$

and

$$\alpha_e = \arctan\left(\frac{\sec \alpha - \cos \alpha}{\sqrt{\sec^2 \theta_1 - \cos^2 \alpha}}\right) \quad (4.16)$$

where α_e and θ_{1e} are equivalent surface slope and equivalent incident angles respectively. For $\alpha = 15^\circ$, the constraint given by Equation (4.14) is always satisfied regardless the value of the incident angle. As the slope of turned surfaces in practice is usually less than 15° , this set up will guaranty that neither shadowing nor multiple scattering will occur.

The above derivation was based on geometrical optics which did not take into account the diffraction effect. It under-estimates the degree of the multiple scattering to some extent. Nevertheless, it yields a qualitative comparison of the two scattering

geometries.

4.3 Experiment and Results

Scattering experiments were conducted to verify the model. The experimental setup is shown in Figure 4.2. A He-Ne laser was used to project a beam onto the test surface at a small grazing angle. The scattering pattern was received on a screen placed at a distance 1 meter away from the test sample. The screen pattern was captured by a CCD camera which was situated at 1.2 meter in front of the screen. The image was digitized into 512x480x8 bits elements by a frame grabber board of a P C vision system. The image was stored on a magnetic disk for later processing. By using a square grid calibration system, the spatial resolution of the system was found to be 0.285 and 0.25 mm/pixel for the horizontal and vertical directions, respectively.

For accurate setting, provisions were made to rotate the sample in steps of a fraction of a degree (i.e. 0.5°). An on-screen spot marked by the laser in the absence of the sample (point B in Figure 4.2) was conveniently used as a reference point for distance measurement. The angle of incidence was calculated from the distance (d in Figure 4.2) to the specular spot:

$$\theta_1 = \arctan\left(\frac{d}{2D_x}\right) \quad (4.17)$$

The same two standard samples A and B were used in the test. The images of the scattering patterns of these as displayed on the monitor are shown in Figure 4.8 (a and b). It can be observed that these images consist of a series of discrete dots aligned along

a circular arc whose radius is dependent on the incident angle and the surface spatial wavelength. The digitized intensity profiles along the curved center line of the pattern for the two samples are shown in Figure 4.8 (c and d). The spacings between these dots were found to be inversely proportional to the surface wavelengths (see Equation (4.12)), the wider the spacing, the longer the wavelength.

4.4 Comparison between Theory and Experiment

(1) Spacings of the scattering order:

In this setup, the lateral scattering angle was less than 5° which justified the assumption of small lateral scattering angle. By measuring the horizontal spacing of the scattering pattern on the screen, the surface wavelength for the two samples were determined. These results were within 5% of the results measured by the stylus instrument.

(2) Peak intensity distributions

Peak intensity measurements were made at various scattering modes of sample B ($R_s=3.0 \mu\text{m}$) and the results were plotted in the form of a bar graph as shown in Figure 4.9. These were compared with the predicted values shown in the same figure. It was observed that in the region of the low-order scattering modes, the two curves had similar trends. However, for high order modes, e.g. greater than 10, there were some significant difference. In this case, the model predicted a greater number of high order scattering than what was observed. Similarly, in Figure 4.10 for sample A, the second scattering

peak was measured but not indicated by the model. This discrepancy may be due to the fact that a) shadowing and multiple scattering might occur which was not accounted for in the model, and b) there were some variations in the surface wavelengths across the sample. This non-uniformity might reduce the intensity of the fringe especially those of high orders. This would reduce the number of scattering modes that could be observed.

(3) Intensity versus grazing angle:

The intensity variation for different scattering orders ($0, \pm 1, \pm 2$) were measured for sample B ($R_s=3 \mu\text{m}$) and the results are shown in Figure 4.11a. The grazing angle in this case was varied from 5° to 11° . These were compared to the predicted curves shown in Figure 4.11b. It was observed that the two graphs had the same exponential decay envelopes and the same number of periodicity (number of peaks and valleys). Thus it can be said that the model was fairly accurate in predicting the oscillation behavior of the scattering components. It should be noted that this observation was applicable to the low order scattering components. For high order modes, however, the model might not be as reliable.

4.5 Summary

The following are the particular remarks:

- (1) The Beckmann's model can give a good approximation to the light scattering of periodic surfaces in the region close to the specular direction where the basic assumptions relating to the uniformity of surface wavelength and the absence of shadowing and multi-reflection hold true.

- (2) The surface wavelength calculated from the measurement of horizontal spacings from adjacent scattering modes agreed with the stylus measurement.
- (3) Similar to the results obtained in the preceding chapter, for any given scattering order, the relationship between the scattering intensity and the grazing angle was uniquely related to roughness. This behavior was predicted by the model and was confirmed by the experimental results.
- (4) The scattering geometry used here allows us to apply an illumination near zero grazing angle. For this geometry, the scattering pattern is confined in a small solid angle which simplifies the acquisition of the scattering images.
- (5) These results provide a basis for the development of a new technique for surface roughness estimation. The model thus offers a useful tool for analyzing cylindrical rough surfaces which will be dealt with in the next chapter.

Chapter 5

Light Scattering from Turned Surfaces and Surface Roughness Measurement

In this chapter, an investigation into the light scattering from cylindrical surfaces at near-zero grazing angle is made by adapting the Beckmann's scalar scattering model for flat surfaces. A solution for cylindrical surfaces, having sinusoidal roughness profiles, will be derived. Numerical solutions will be obtained to study the influence of the surface amplitude and wavelength on the scattering behavior.

Scattering intensity measurements are carried out for turned surfaces of different roughness. Based on the new findings, a novel technique of surface roughness estimation for turned surfaces is developed and tested. The measurement performance is examined in terms of range, speed, accuracy and its potential to in-process applications.

5.1 Scattering Model for a Cylindrical Surface

The validity of the Beckmann's scattering model for flat surfaces has been confirmed by the experimental results in the previous chapters. These surfaces are periodic rough surfaces whose average height is a plane. In this chapter, this model is applied to cylindrical surfaces. The surfaces considered here have a periodic roughness

along the axial direction which typifies a turned surface. In such a surface, the height variation in the circumferential direction is negligible for ideal turning, therefore is not considered in the model.

Consider the scattering geometry shown in Figure 5.1. An incident beam from a coherent light source is projected to the top of the cylinder in a direction perpendicular to its axis. The top portion of the beam, without any obstruction, travels straight to the screen to create a bright spot. This spot is chosen as the origin of the screen coordinate system. The lower part of the beam, which constitutes a larger portion of the beam, impinges upon the top surface of the cylinder and subsequently scatters into a spatial distribution. The illuminated portion of the surface forms an arc parallel to the plane of the lay.

To predict scattering on such a surface, the approach used here is to divide the illuminated arc into a number of small elements. Each element is treated as a flat surface whose scattering property is predicted by the model established in previous chapters. To adapt this model to the curved surface, it is necessary to define the coordinate transformation between the curved and the flat surface systems.

Let us consider a cylindrical surface (of radius R) whose roughness profile is periodic with the lay direction perpendicular to the axis of the cylinder. On this cylinder, consider an illuminated element whose tangent makes an angle α with the Z -axis of the cylinder, Figure 5.2. The scattering from this element can be predicted using the flat surface model, Equation (4.1). In this application, a local coordinate system (X_L, Y_L, Z_L) , is introduced (where X_L lies on the tangential plane of the element).

For convenience, a local grazing angle α is used here instead of the incident angle θ_1 , which is equal to $(90^\circ - \alpha)$. The illuminated arc extends from $\alpha=0$ to α_1 . A screen coordinate system (Y_s, Z_s) is established with its origin located at the direct impingement point of the beam. The transformation of spherical coordinates (θ_2, θ_3) , shown in Figure 5.2, to Cartesian coordinates (Y_s, Z_s) located on the screen, is given by:

$$\begin{cases} y_s = (D_x + \delta_x) \tan \theta_2 \\ z_s = \sqrt{(D_x + \delta_x)^2 + y_s^2} \cot \phi - \delta_z \end{cases} \quad (5.1)$$

where:

$$\delta_x = R \sin \alpha \quad (5.2)$$

$$\delta_z = R(1 - \cos \alpha) \quad (5.3)$$

and for small θ_3 ,

$$\phi = \theta_2 - \alpha \quad (5.4)$$

When the cylinder radius is small compared to the distance to the screen D_x , the coordinates are simplified to:

$$\begin{cases} y_s = D_x \tan \theta_2 \\ z_s = D_x \cot(\theta_2 - \alpha) \end{cases} \quad (5.5)$$

Furthermore, for the zero-order fringe, Z_s in Equation (5.5) is reduced to

$$Z_s = D_x \cot(\theta_2) \quad (5.6)$$

This coordinate transformation allows us to determine the scattering pattern of a given element as the pattern is projected on a screen. By superimposing the scattering of all the elements on the curved surface, each associated with a tangential plane and a local grazing angle α , one can obtain the resulting scattering of the cylindrical surface. This superposition is carried out numerically (described in the next section), with α varying from 0 to α_1 using a small increment (e.g. 0.5°).

5.2 Numerical Solutions

From Equation (4.8), the intensity of the zero-order scattering or fringe is derived for a cylindrical surface having a sinusoidal surface roughness profile defined by Equation (4.7) as:

$$I_0(\theta_2) = J_0^2\left(\frac{2\pi H}{\lambda} \cos \theta_2\right) \quad (5.7)$$

Using the coordinate transformation given by Equation (5.6), the intensity distribution along the Z_s axis of the screen is calculated.

To investigate the intensity distribution characteristics along a fringe, numerical solutions for the scattering in the zero-order fringe ($m=0$) were obtained for cylindrical surfaces. Table 5.1 shows the amplitude and the wavelength of the sinusoidal roughness

profiles used in the calculation. For a given angle α (which corresponds to a local incident angle θ_i) on the cylinder, the intensity of the zero-order fringe was obtained from Equation (5.7). The coordinate Z_s for any spot along the fringe on the screen was determined from Equation (5.6). A plot of the intensity versus screen ordinate, Z_s , is shown in Figure 5.3. It should be noted that these results provide a first order approximation to the scattering of turned surfaces whose roughness profiles are periodic and closely related to a sinusoidal wave.

5.3 Experimental Setup and Results

To confirm the model's prediction, a He-Ne laser with a wavelength of $0.633 \mu\text{m}$ was used to project a narrow light beam on top of the cylinder as shown in Figure 5.1. The scattering pattern was received on a translucent screen placed 1 meter away from the sample. This pattern was imaged by a CCD camera which was placed beside the laser and was directed at the screen.

The resolution of the image digitizer was $512 \times 480 \times 8$ bit pixels. The imaging system was first calibrated using a square grid pattern of known dimensions to obtain a spatial resolution of 1.0 mm and 1.2 mm per pixel in the horizontal and vertical directions, respectively. Scattering patterns of the samples were digitized and stored on a magnetic medium for later analysis. Care was taken to reduce the blooming of the CCD because of the high intensity of the specular component.

Five aluminum samples of 35 mm diameter, were machined to have RMS roughness values ranging from $0.4 \mu\text{m}$ to $4.5 \mu\text{m}$. The surface profiles, shown in Figure 5.4, were measured by a stylus instrument. Except Sample No. 1 which is random and

fairly smooth, all samples are periodic. Their Fourier transforms exhibit a dominant primary peak and relatively small harmonics. As such, these surfaces can reasonably be approximated by a sinusoidal profile.

5.4 Discussion

In this section, a discussion of the general behavior of light scattering, observed during the experiment, is first given. The influence of roughness amplitude and wavelength on the scattering intensity and its spatial distribution is then analyzed. Finally a comparison between the experimental results and the theoretical predictions is made.

5.4.1 General Scattering Patterns

The images of the scattering pattern of 5 turned samples captured by the camera are shown in Figures 5.5a to 5.5e. The brightest spot on the image corresponds to the origin of the screen coordinates. For the smooth surface, Figure 5.5a, the scattering pattern consists of primarily a zero order fringe which passes through the origin of the screen coordinates. As the roughness increases, higher order fringes start to appear as a set of lines parallel to and at either side of the zero-order fringe, Figures 5.5b-5.5e.

The fringe pattern intensity distribution is not symmetric with respect to the zero-order fringe, e.g. the intensity distribution along the fringe ($m = +1$) is not the same as that along fringe ($m = -1$). This may be attributed to the non-symmetrical property of the roughness profile. This property can be easily demonstrated by observing the reversed skew of the scattering pattern when the sample is turned 180° . This was indeed the case.

5.4.2 Surface Wavelength

For any given scattering pattern, there is a variation of intensity across the pattern, along the fringe and also from one fringe to the next. The spacing between the fringes (in Y_z -direction, Figure 5.1) and the fringe starting locations (in Z_s) are governed by the grating Equations (4.3) and (4.4). As the wavelength of the surface increases, the fringe spacing decreases, compare Figure 5.5b ($\Lambda=52 \mu\text{m}$) to 5.5c ($\Lambda=156 \mu\text{m}$).

As more higher order fringes are added to the pattern, as a result of increasing roughness, the overall intensity of the image decreases and the fringe visibility or contrast deteriorates, see Figure 5.5d. This may be due to the increase in randomness in the surface profile. The envelope of the fringe edges for the rough surface, Figure 5.5e, forms a "V" shape which can be predicted from Equation (4.8) using the coordinate transformation given above.

To study the intensity distribution of the pattern across the fringes, the grey level distribution along a line of constant screen height Z_s was plotted for different samples as shown in Figure 5.6. These distributions are skewed to one side which further illustrates the non-symmetrical property of the pattern. The width of the fringe is, in theory, governed by a sinc function only applicable to periodic surfaces. This width is affected by the size of the illumination foot-print, i.e. the larger the footprint, the narrower the fringe width. As indicated in Chapter 2, a small random surface height variation also affect the fringe width, however, its nature is not fully explored.

The surface wavelength was calculated using the fringe spacing as measured from the scattering patterns. The results are shown in Table 5.2 together with the stylus results

for comparison. Good agreement was observed as there is only a small difference between the two, see also Figure 5.7.

5.4.3 Surface Roughness Amplitudes

For a given fringe order, there is an intensity variation along the length of the fringe. This variation is related to the amplitude of the surface roughness and is independent of the surface wavelength. For the zero-order fringe, the fringe intensity distributions for different samples of different roughness are plotted as shown in Figure 5.8. For smooth surfaces, the fringe intensity decreases monotonically as the screen ordinate increases. For rougher surfaces, however, the fringe intensity oscillates as this distance increases. The number of oscillations in this case increases as the roughness increases. This unique property can be used to determine the surface roughness as described later. Similar observations for both the zero order scattering and the m th-order scattering were noted in previous chapters for scattering from flat surfaces when the illumination plane was perpendicular to the lay.

5.4.4 Comparison of Results

Numerical results, as obtained, represent the first order approximation of the light scattering from turned samples. The light scattering intensities versus screen ordinate (or distance) curves were plotted for the zero-order scattering as shown in Figure 5.3. These are for surfaces of different roughness amplitudes. In general, these curves show similar trends to those obtained in the experiment, comparing Figures 5.3 to 5.8.

There are some discrepancies, however, at the region near the screen origin. In this region, in contrast with the numerical calculation, there is virtually no difference between the experimental curves for the three samples having the lowest roughness in the experiment. This discrepancy can be attributed to a) the blooming effect of the CCD element near the bright spot at the screen origin which causes the neighboring pixels to have greater intensity values, b) the non-uniformity of the intensity distribution of the laser beam (Gaussian beam), which produces a non-uniform footprint on the surface and thereby modifies the intensity distribution curve somewhat.

5.5 Additional Evidence

For smooth surfaces whose roughness amplitude is approximately the same as the illumination wavelength, the scattering behavior has some special characteristics which can be utilized for roughness quantification. In this range, the intensity of the zero-order fringe at a given screen ordinate decreases monotonously as the roughness increases. The trend is reversed for the $m=\pm 1$ order, i.e. its intensity at a given screen ordinate increases with the increase of roughness. Thus it is possible to use any of these parameters to indicate roughness. However, for maximizing the sensitivity of the measurement, one can use the ratio of the two parameters as a roughness indicator. Figure 5.9 shows the relationship between the roughness indicator and R_a which was obtained from the model for sinusoidal surfaces of different roughness. Test results obtained by Cuthbert (1992) exhibit the same trend as predicted in Figure 5.9. Both the model and the experimental results show that saturation occurs at a roughness level around $1 \mu\text{m } R_a$.

It should be noted that the roughness indicator versus R_a curve, as established above, is strongly dependent on the selection of the location on the fringe (or scattering angle) where the intensity measurement is performed. At low scattering angle, the fringe intensity (at zero order) decreases rapidly as the surface roughness increases. In order to extend the measurement range, one needs to move the point for intensity measurement to larger scattering angles. In addition, as there is a large difference in intensity between the zero and the first order fringe at a given ordinate, a high dynamic range is required for the sensor in this method.

A roughness measurement method based on the roughness indicator, as defined above, has been developed for on-line measurement in turning. It performed reasonably well for hard turned surfaces with roughness range between $0.1 \mu\text{m}$ and $0.6 \mu\text{m}$ R_a . The major drawback of this technique is that it is an intensity-based measurement which is dependent on the workpiece material and the surface wavelength.

5.6 Surface Texture Measurement Procedure

Two important discoveries were confirmed experimentally in the previous sections: (1) The fringe spacing is related to the surface wavelength by the grating equations, and (2) The intensity variation along each individual fringe is related to the surface roughness amplitudes. One can utilize these properties to develop a new measurement technique for surface wavelength and surface roughness of cylindrical surfaces. This will be discussed in this section.

5.6.1 Principles

a) Surface wavelength

To determine the surface wavelength, the spacing (Δ_y) between the two adjacent fringe orders is first measured. The surface wavelength is then calculated by

$$\Delta = \frac{D_x \lambda}{\Delta_y} \quad (5.8)$$

where D_x is the screen distance from the sample. In this equation, it is assumed that the grazing angle is near zero, i.e. $\sin\theta_2 \approx 1$ and $\sin\theta_3 \approx \Delta/D_x$.

In this setup, $D_x = 1000$ mm, $\lambda = 0.633$ μm , Δ is measured in millimeters.

Equation (5.8) now becomes:

$$\Delta = \frac{633}{\Delta_y} \quad (\mu\text{m}) \quad (5.9)$$

This inverse relationship between the surface wavelength and fringe spacing is illustrated in Figure 5.10. This finding may be considered as a new application of well-known grating equations.

b) Surface roughness

Surface roughness amplitude is estimated by measuring the screen ordinate of the first minimum point, denoted by D_f , defined by the distance between the reference point and the first local minimum in the intensity versus distance curve of the central fringe

(zero scattering order). For brevity, D_f can now be referred to as the First Minimum Distance. This distance is associated with the first root of the Bessel function in Equation (5.7).

Let R_f be the variable in the Bessel function given in Equation (5.7), i.e.:

$$R_f = 2\pi H \cos \theta_2 / \lambda \quad (5.10)$$

Expressing θ_2 by the geometrical parameters, after re-arranging one can obtain:

$$H = \frac{\lambda R_f \sqrt{4D_x^2 + D_f^2}}{2\pi D_f} \quad (5.11)$$

Since the screen distance from the sample is much greater than the first minimum distance, i.e. $D_x \gg D_f$, the above equation can be further simplified as

$$H = \frac{\lambda R_f D_x}{\pi D_f} \quad (5.12)$$

The above equation defines the relationship between the roughness amplitude (H) and the First Minimum Distance (D_f). This forms a basis for the proposed surface roughness amplitude measurement technique.

The first root of the Bessel function was found to $R_f=2.41$ (Hahnke and Emde, 1945). The average roughness for the sinusoidal profiles as derived from geometry is: $R_a = H/\pi = 0.319H$. Substituting R_a and R_f values into Equation (5.12) and solving for R_a , one obtains:

$$R_a = \frac{154.7}{D_f} \quad (\mu m) \quad (5.13)$$

where D_f is the ordinate (measured in millimeters) of the first minimum point in the intensity curve.

The above equation indicates that the surface roughness (R_a) is inversely proportional to the first minimum distance (D_f) (Figure 5.11a). A similar relationship can be developed for other type of surfaces such as those considered in Chapter 3. The R_f corresponding to the first minimum may have to be calculated by numerical procedures as analytical solution is not available.

The physical meaning of the first minimum point of the central fringe intensity profile can be illustrated by considering two parallel light rays (from a coherent source) impinging upon a periodic surface which has a square wave profile. These rays are parallel to the surface grooves. One ray is incident at the top and the other at the bottom of the wave, see Figure 5.11b. The phase difference between these two reflected beams can be shown to be $4\pi H \sin \gamma / \lambda$. At $\gamma=0$, the phase difference vanishes, the two rays will be in phase to give a maximum intensity on the receiving screen. When γ increases, the phase difference increases. When the phase difference reaches π , the two rays will interfere to give a minimum intensity. This corresponds to the first minimum in the intensity versus distance curve as defined above.

It can be shown that the value for D_f in this case is given by:

$$D_f = \frac{8\lambda H D_x}{16H^2 - \lambda^2} \quad (5.14)$$

For small grazing angles and with $R_a = 0.5h$, the above equation yields:

$$R_a = \frac{\lambda D_x}{2D_f} \quad (5.15)$$

For the current setup, with $D_x = 1.0$ m and $\lambda = 0.633$ μm , we have:

$$R_a = \frac{158.3}{D_f} \quad (5.16)$$

Equations (5.13) and (5.16) define the relationships between R_a and D_f for sinusoidal and square wave surfaces, respectively. These equations are exactly the same (within 2% error) even although they were derived for surfaces of completely different geometrical profiles. Thus, it can be presumed that the relationship between R_a and D_f is insensitive to the types of surface profiles.

Using this relationship, a calibration curve for R_a versus D_f can be first obtained. This can then be used to find the surface roughness R_a directly when D_f is known. The calibration curve as obtained above is similar to the surface wavelength versus fringe spacing relationship in a sense that it is dependent on the illumination wavelength. Thus

a change in the illumination wavelength produces a change in the measuring range in both quantities. These relationships, however, in theory, are independent of material property.

5.6.2 Test Results and Comparison with the Stylus Data

(a) Surface wavelength

The wavelength measurement by the optical technique was relatively simple and straight forward. Only the fringe spacing on the screen is to be measured. The results are in excellent agreement with the stylus measurements as shown in Figure 5.12. In this application, both techniques, optical and stylus, are fairly accurate, better than 10%.

(b) Roughness

The relationship between R_a and the measured distance D_f is shown in Figure 5.13. A theoretical prediction is also shown in this figure for comparison. Good agreement is observed. It should be noted, however, that to measure the distance D_f , a visual guess has to be made as to where the local minimum of the curve is located. Most often in the experiment, this part of the curve was found to be fairly flat which would cause a large uncertainty in the results.

The above data is replotted in Figure 5.14 to show a correlation between the measurements of R_a made by the two methods (on the same sample), one with a stylus and the other with the optical method. The agreement is reasonably good in spite of the large uncertainty in the stylus method (up to 50% uncertainty in one case). It should be

pointed out here that the R_a value from the stylus measurement is dependent on the cut-off wavelengths, whereas in the optical method there is no such dependency. For this reason, it may not be possible, in general, to achieve a perfect correlation between this method and the stylus method.

As another check, similar R_a measurements were made for the two standard surfaces which have symmetrical triangular roughness profiles. The D_f values were found to be 50 mm and 360 mm for the two samples respectively. These yield estimates of R_a as $3 \mu\text{m}$ and $0.43 \mu\text{m}$ as compared to $3 \mu\text{m}$ and $0.5 \mu\text{m}$ as quoted, respectively. Thus good agreement is achieved.

5.6.3 Performance

The performance of the measurement system as developed in this work is analyzed with respect to repeatability, resolution, range and accuracy. The influence on the measurement roughness by workpiece physical properties, such as material and physical dimensions, is also analyzed.

(a) Repeatability:

Repeatability is of prime concern to any measurement system. It depends on the noise and any other random effect that propagates throughout the measurement system. In this section, we concentrate on the investigation of the variation of the scattering patterns due to the sample uniformity and measurement system stability (variation with time).

The system stability is first evaluated by digitizing the intensity of the scattering pattern of the same spot on a given sample at different times. This was carried out using the same setup described previously. Figure 5.15 shows the test results of intensity measurements along the central fringe. It is observed that even though there is some variation in the signal outputs due to random disturbances such as the fluctuation in laser intensity, the noise in CCD elements and other electrical noises in the digitizer, this variation is smaller than the intensity resolution of the digitizer. Therefore, the two curves are identical.

In the next step of the stability evaluation, two scattering images from different spots of the same sample were obtained and digitized. From these, the intensity curves for the zero order fringe were produced and plotted as shown in Figure 5.16. It is evident through this figure that although the fringe intensity curves do not exactly coincide, however, the location of the first minimum is about the same for both. As a rough estimation, the repeatability was determined by measuring a typical sample (with $R_a = 4.0 \mu\text{m}$) repeatedly (5 times) and the standard deviation was found to be 10 % of the mean R_a value.

(b) Resolution and Sensitivity:

Resolution is defined as the largest change in the input without any change in the output of the measurement system. For this system, the resolution varies with roughness: it is high for smooth surfaces and low for rough ones. For surface roughness measurement, the resolution is determined mainly by the error in estimation of the first minimum point of the fringe intensity profile. This profile in turn, depends on the image

quality of the scattering pattern. For the setup used here, the minimum discernable difference in R_q among the test samples is about $0.3 \mu\text{m}$. This value was obtained by visually locating the minimum point, therefore, it can be considered as a rough estimate.

Since both the wavelength and roughness are determined by the distance between the features in a scattering image filled with speckled pattern, the ultimate resolution will be limited by the speckle size. This size is determined by the footprint diameter d , via equation: $\text{size} = 1.2\lambda D_s/d$ (Ennos, 1975). For this setup the speckle size was found to be 0.25 mm in diameter. This is about a fraction of the resolution of the CCD camera used in the measurement. Thus, the effect of speckle in the measurement is negligible.

Sensitivity, on the other hand is defined as the slope of the output versus input curve. The sensitivity for this system, similar to the resolution, is high for smooth surfaces and low for rough surfaces by virtue of the inverse distance versus R_q relationship.

(c) Range:

i) Surface wavelength

For the fringe spacing measurement in this setup, the maximum surface wavelength measurable was $300 \mu\text{m}$. The measurement system at this point, is approaching the spatial resolution of the CCD camera. As the fringe spacings between different scattering orders (at small grazing angles) are virtually constant, they can be approximated by measuring the spacing between any two higher order scattering fringes.

Some difficulty may arise when measuring surfaces with long surface wavelengths as the resulting fringes may overlap (or may have very narrow spacings). In addition, poor image contrast may also exist which makes fringe locating difficult. At the present

time, there is no theoretical limit for the minimum surface wavelength that can be measured. However, for very smooth surfaces, the high order fringes possess a very low intensity level in general. To detect such fringes, a high sensitivity camera coupled with a very low ambient light level is required. For the present setup, the system was capable of measuring surface wavelengths from 12 to 300 μm .

ii) Roughness amplitude

The lower limit of the measured roughness amplitude is dependent on the fringe visibility and the camera dynamic range. For smooth surfaces the first minimum of the fringe intensity profiles occurs at fairly large scattering angles. In this case, the low fringe intensity, coupled with random speckles makes it difficult to determine this first minimum intensity point. A camera with large dynamic range and high sensitivity at low illumination is helpful in this situation for it is able to pick up the low intensity signal. For the current setup, the low limit for R_a was found to be around 1.0 μm .

The upper limit for the roughness amplitude is governed by the camera resolution. This limit is also dependent on the fringe visibility and the camera dynamic range. For rough surfaces, the oscillation amplitude in the fringe intensity profile (along the fringe) is relatively small. Therefore, it may be difficult to determine the first minimum point of the fringe intensity distribution. For the current setup, the measurement range was established as from 1 μm to 10 μm R_a .

It should be noted that in the above analysis, the sample is assumed to be periodic and uniform. Any change in the wavelength or amplitude of the profile will deteriorate the quality or contrast of the fringes. This will certainly affect the measurement and should be taken into account. However, this is beyond the scope of this work.

(d) Effect of workpiece physical properties

In theory, the material of the sample has no direct effect on the measurement. Different materials, because of different reflectivity coefficients, may change the overall intensity of the pattern. This change may cause a shift in the intensity profile curves of the fringes in a vertical direction. However, the locations of the first minimum point of the curves still remain the same. This is evidenced in the established results shown in Figures 5.13 and 5.14 which include samples of different materials such as steel, aluminum, cast iron and copper. In these figures, a reasonable fitting of the curves through the data points indicates that different materials did not have any effect on the results in the range considered.

The dimension of the samples used in this work ranges from 6 mm to 150 mm in diameter. No discernable change in the measurement was attributed to the dimensions of the workpiece within this range. However, no further study was made in this area.

Other factors which affect the measurement performance may include the sample or workpiece mis-alignment. In the measurement setup, it is required to align the light beam perpendicular to the axis of the cylinder (i.e. parallel to the lay). Any mis-alignment will effectively increase the first minimum distance D_f and thus make the surface appear smoother. Figures 5.18a and b show the scattering patterns from a turned surface with the sample at proper alignment and at 20° misalignment respectively. This misalignment produces a 2 mm increase in the minimum distance measurement (10% error). In general, test results showed that small mis-alignments, up to 10°, can be tolerated without any significant change in the results.

(e) Accuracy:

To evaluate accuracy of a measurement technique, it is necessary to perform measurement on a set of samples which are known or measured accurately by other standard techniques. This is a difficult process in this case because a) the inaccuracy of the stylus instrument which is considered as standard, and b) the unavailability of uniform roughness samples. However, it is possible to estimate the uncertainty in this method. The sources of uncertainty can be divided into two groups: measurement factors and surface factors and these are analyzed below.

The measurement factors are those related to the sensing and measuring apparatus. The surface wavelengths, as obtained in this method, are a function of the screen distance (D_s), the illumination wavelength (λ) and the fringe spacing Δ_y . The first two quantities can be determined fairly accurately and they remain practically constant. The uncertainty in the measurement can thus be approximated by the uncertainty in the measurement of the fringe spacing, i.e.:

$$\frac{\Delta\lambda}{\lambda} = \frac{\Delta\Delta_y}{\Delta_y} \quad (5.17)$$

Similarly, the surface roughness uncertainty is approximated by the uncertainty in determining the first minimum distance D_f , i.e.:

$$\frac{\Delta R_a}{R_a} = \frac{\Delta D_f}{D_f} \quad (5.18)$$

As both surface wavelength and roughness values are inversely proportional to Δ , and D_p , respectively, good accuracy can be obtained in measuring short wavelengths and small roughness values and vice versa.

5.6.4 Advantages and Drawbacks

(a) Advantages:

The proposed method offers the following features:

- Two parameter measurement

Two texture parameters (surface roughness and wavelength) are obtained from measuring a scattering pattern. They are sufficient to quantify the turned surface profile.

- High speed capability.

As the measurement process which includes scattering pattern digitization, fringe spacing, and the first minimum distance calculation, can be developed and automated to perform at a fast speed, the process is capable of high throughput.

- Absolute measurement

This method is independent of the test material property. The wavelength and roughness values are calculated from geometrical parameters and the illumination wavelength. A universal calibration curve can be established for all workpieces of different materials.

(b) Drawbacks

The major disadvantages of this techniques are:

- Limited range

The lower limit of roughness R_a is about $1.0 \mu\text{m}$ which may not be adequate for measuring fine surface finishes such as in hard turning.

- Limited to periodic surfaces

This method is based on the scattering pattern which has clearly visible fringes. Therefore it is not applicable to non-periodic surfaces such as random or quasi-random surfaces from which the scattering pattern will exhibit a continuous distribution instead of discrete fringes.

There are means to improve the performance of this technique. One way is to improve the method of determining the minimum distance by using such a technique as optimum search or extrapolation. Another way is to expand the dynamic range of the camera or increase the camera resolution.

5.7 Summary

A formulation of rough surface scattering was developed for curved surfaces. The method was based on the Beckmann's model where the incident beam is parallel to the lay of one-dimensional periodic surfaces. A closed form solution was obtained for sinusoidal surface profiles. Numerical results were obtained to study the characteristics of the scattering for different surface roughness amplitudes and surface wavelengths.

The images of the scattering patterns were obtained for turned surfaces which approximated the surface texture as modeled. Fringe intensity distributions across the pattern as well as along the fringe were measured and studied. In general, the intensity distribution curves along the zero-order fringe for both experiment and prediction are

similar in shape and characteristics. These curves uniquely define the roughness height of the surface. The surface wavelengths for these samples were also calculated from the fringe spacing using the grating equations. These were compared to the stylus data and good agreement between the two was observed.

As a derivation from this work, a new method of surface texture measurement of turned surface was proposed. By measuring the spacing between the zero order and the first order fringes, the surface wavelength was calculated. Surface roughness (R_a) was estimated from a measurement of the First Minimum Distance. The working range for this is within the range of normal industrial turning. This method offers the advantage of being independent of material property of the surfaces that could not be found in other techniques.

Chapter 6

Conclusions and Recommendations

This project is a combination of numerical and experimental study of light scattering from rough surfaces. These surfaces were periodic and of a one dimensional nature. The illumination planes used in this study were both parallel and perpendicular to the lay of the workpiece. This work was also extended to cylindrical rough surfaces which are applicable to surfaces produced in industrial turning processes. Experimental work on scattering measurements was carried out to verify the numerical results. A new method of roughness assessment for turned surfaces was also devised and successfully tested. The major objectives of this work were achieved.

6.1 Contributions

The importance of the contributions of this research was noted in the previous chapters. It can be summarized as follows:

(1) The Beckmann's periodic model was adapted to very rough surfaces to investigate the light scattering from periodic machined surfaces. This attempt was first in surface roughness measurement research to apply an electromagnetic wave theory to

the light scattering from machined surfaces. The results shed light on the future prospect as well as the limitation of the model. Although this study is directed to surface roughness measurements, the light scattering from rough surface is a fundamental phenomenon which can be applied to other optical measurement techniques for rough surfaces and other non-contact techniques such as sonar, ultrasonic, and radar methods which employ wave scattering properties. The results of this study are a valuable contribution in this context.

(2) To the author's knowledge, this is the first time that the relationship between the intensity variation of individual scattering mode and the incident angle was investigated and utilized for surface roughness estimation purposes. The intensity characteristic and its application to periodic surface roughness measurement were first proposed by Fan and Huynh (1992) in a numerical study which was again presented in Chapter 2. This leads to a study of scattering whose incident plane is parallel to the lay. This is a new investigation which is not found in the literature.

(3) A New formulation of light scattering from rough cylindrical surfaces was established. The influence of the surface roughness was investigated using this superposition of the flat surface scattering.

(4) A novel surface roughness measurement technique was proposed as a result of the scattering analysis from cylindrical surfaces. This technique offers absolute measurements for surface roughness and surface wavelength. These quantities are calculated based on illumination wavelength and are independent of material property. Because of these unique features, this method shows great promise not only as standard

testing method in laboratories but also for in-process roughness monitoring and control in machining.

6.2 Conclusions

Following are the conclusions from this study:

(1) The Beckmann's scalar model can be used to predict light scattering from turned surfaces. This model is reasonably accurate at low scattering angles but is not adequate in predicting the scattering at high scattering angles. It generally over-predicts the scattering energy in the higher scattering modes.

(2) There is a definite relationship between the oscillation of scattering intensity (which occurs when the incident angle changes) and the surface roughness. The intensity of any given scattering order oscillates when the incident angle changes. An increase in surface roughness will increase the degree of the intensity oscillation. For turned surfaces which are classified as rough surfaces, these variations can only be observed at very small grazing angles.

(3) The scattering from turned surfaces can be formulated by the superposition of the scattering from small flat elements whose characteristics are modelled using the Beckmann's method. As such, the intensity distribution in each fringe can be seen as a result of the flat surface scattering when the grazing angle changes from zero to a small positive value. Thus, the resulting scattering pattern has no direct relationship to the diameter of the workpiece.

(4) The location of the first minimum point on the intensity profile curve of the central (the zero order) fringe is related to roughness amplitudes. An inverse relationship

exists between the distance to the first minimum point and roughness. Similarly, the horizontal spacing between adjacent fringes is in inverse proportion to the surface wavelength.

(5) Surface roughness estimation based on the first minimum distance measurement can be carried out for normal turned cylindrical surfaces between $1\ \mu\text{m}$ and $10\ \mu\text{m}$ R_a . The calculated values have good correlation with those by stylus measurement. A good repeatability has been demonstrated. The method is not sensitive to mis-alignment and mechanical disturbance. Measurement can be possibly performed while the part is rotating.

(6) Surface wavelength calculation from the fringe spacing measurement shows an excellent agreement with stylus between $12\ \mu\text{m}$ and $300\ \mu\text{m}$. This covers the range of normal turned surfaces.

6.3 Recommendations

This research is a first attempt to investigate light scattering from machined surfaces using near-zero grazing angles. The proposed surface roughness technique was successfully tested but in a preliminary manner. There are a number of unanswered questions and areas that need to be improved. For future work, further investigation is required in the following areas:

(1) Automation of the measurement process

To facilitate the surface wavelength measurements, it is necessary to develop a measurement procedure and also software to automatically perform the measurement of

fringe spacings and the first minimum distance. These techniques are required for the implementation of this method to in-process measurement of roughness. In addition, for improvement of measurement accuracy, image processing and enhancement techniques should be explored to reduce noise and other random effects.

(2) Design of a prototype for in-process measurement

The measurement setup used in this research is fairly simple. It serves well to confirm the model's prediction. However, this is an indirect type of image measurement where the scattering pattern is captured by the camera from the screen. This indirect type of measurement is susceptible to interference due to ambient light and is not adaptable to an industrial environment. A practical direct measurement system should be developed and built. The setup may include linear CCD arrays which can measure the intensity of the fringes directly. This will offer better measurement accuracy and repeatability. More importantly, the in-process capability of the system can further be explored.

(3) Further study on scattering

Numerical simulation techniques should be explored in detail to study scattering from real turned surfaces. The roughness profiles can be digitized from real surfaces and these can be used as inputs to the model. The results may provide some more information regarding the influence on scattering by the different complex surface profiles. Some effort should also be made to quantify the effect of random components.

References

- Aas, J. A., 1972, "Reconstruction of Surface Profiles from Their Diffraction Spectra," *Applied Optics*, Vol. 11, No. 7, pp.1579-1584.
- Allardyce, K. J., and George, N., 1987, "Diffraction Analysis of Rough Reflective Surfaces," *Applied Optics*, Vol. 26, No. 12, pp.2364-2375.
- ANSI/ASME B46.1, 1985, "Surface Texture (Surface Roughness, Waviness, and Lay)," The American Society of Mechanical Engineers, New York.
- Bass, F. G., and Fuks, I. M., 1979, *Scattering of Electromagnetic Waves from Statically Irregular Surfaces*, Pergamon, New York.
- Beckmann, P., 1963, "Theory," *The Scattering of Electromagnetic Waves from Rough Surfaces*, Part 1, Beckmann, P., and Spizzichino, A., The MacMillan Company, New York.
- Beckmann, P., 1965, "Shadowing of Random Rough Surfaces," *IEEE Transactions on Antennas and Propagation*, Vol. AP-13, No. 3, pp.384-388.
- Beckmann, P., 1967, "Scattering of Light by Rough Surfaces," *Progress in Optics*, E. Wolf, ed., Vol. VI, pp.55-69.
- Bennett, H. E., and Porteus, J. O., 1961, "Relation between Surface Roughness and Specular Reflectance at Normal Incidence," *Journal of the Optical Society of America*, Vol. 51, No. 2, pp.123-129.
- Bennett, J. M., and Mattsson, L., 1989, *Introduction to Surface Roughness and Scattering*, Optical Society of America, Washington, D.C..
- Blessing, G. V., and Eitzen, D. G., 1988, "Surface Roughness Sensed by Ultrasound," *Surface Topography*, Vol. 1, pp.143-158.

- Bogy, D. B., Bouchard, G., Chang, W. R., and Talke, F. E., 1986, "Use of the Laser Doppler Vibrometry to Measure the Surface Topography of Magnetic Disk," *Wear*, Vol. 107, pp.227-244.
- Brodmann, R., and Thurn, G., 1986, "Roughness Measurement of Ground, Turned and Shot-Peened Surfaces by the Light Scattering Method," *Wear*, Vol. 109, pp.1-13.
- Brown, A., and Breitmeier, U., 1988, "Industrial Application of an Optical Profilometer," *Optical Testing and Metrology II*, SPIE Vol. 954, pp.200-207.
- Cao, L., Vorburger, T. V., Lieberman, A. G., and Lettieri, T. R., 1991, "Light-Scattering Measurement of the RMS Slope of Rough Surfaces," *Applied Optics*, Vol. 30, No. 22, pp.3221-3227.
- Chao, Y. J., Lee, C., Sutton, M. A., and Peters, W. H., 1986, "Surface Texture Measurement by Computer Vision," *Optical Testing and Metrology*, SPIE Vol. 661, pp.302-306.
- Church, E. L., 1988, "Fractal Surface Finish," *Applied Optics*, Vol. 27, No. 8, pp.1518-1526.
- Cuthbert, L., 1992, "Report on Lathe Sensor Tests," An internal report, Sensor Adaptive Machines, Incorporated, Windsor, Ontario, Canada.
- Cuthbert, L., and Huynh, V. M., 1992, "Statistical Analysis of Optical Fourier Transform Patterns for Surface Texture Assessment," *Measurement Science and Technology*, Vol. 3, No. 8, pp.740-745.
- Depew, C. A., and Weir, R. D., 1971, "Measurement of Reflectance," *Applied Optics*, Vol. 10, No. 4, pp.969-970.
- Elson, J. M., and Bennett, J. M., 1979, "Vector Scattering Theory," *Optical Engineering*, Vol. 18, pp.116-124.
- Ennos, A. E., 1975, "Speckle Interferometry," *Laser Speckle and Related Phenomena*, J. C. Dainty, ed., Springer-Verlag, Berlin.
- Fan, Y., and Huynh, V.M., 1992, "Investigation of Light Scattering from Rough Periodic Surfaces - Numerical Solutions," *Optics and Laser Technology*, Vol. 24, No. 3, pp.145-150.
- Fienup, J. R., 1982, "Phase Retrieval Algorithms: A Comparison," *Applied Optics*, Vol. 21, No. 15, pp.2758-2769.

Fujii, H., and Asakura, T., 1974, "Effect of Surface Roughness on the Statistical Distribution of Image Speckle intensity," *Optics Communications*, Vol. 11, No. 1, pp.35-38.

Garbini, J. L., Koh, S., Jorgensen, J. E., and Ramulu, M., 1992, "Surface Profile Measurement During Turning Using Fringe-Field Capacitive Profilometry," *ASME Journal of Dynamic Systems, Measurement, and Control*, Vol. 114, pp.234-243.

Georgeson, J. D., and Lieu, D. K., 1992, "Inspection of Roller Bearing Surfaces with Laser Doppler Vibrometry," *ASME Journal of Engineering for Industry*, Vol. 114, No.2, pp.123-125.

Goodman, J. W., 1968, *Introduction to Fourier Optics*, McGraw-Hill, New York.

Hingle, H. T., 1987, "A Practical Method of Machine Tool Condition Monitoring by Analysis of Component Surface Finish Data," *Micromachining of Elements with Optical and Other Submicrometer Dimensional and Surface Specifications*, SPIE Vol. 803, pp.108-156.

Hingle, H. T., and Rakels, J. H., 1983, "The Practical Application of Diffraction Techniques to Assess Surface Finish of Diamond Turned Parts," *CIRP Annals*, Vol. 32, No. 1, pp.499-451.

Huynh, V. M., and Fan, Y., 1992, "Surface-Texture Measurement and Characterization with Applications to Machine-Tool Monitoring," *International Journal of Advanced Manufacturing Technology*, Vol. 7, No. 1, pp.1-10.

Huynh, V. M., Kurada, S., and North, W. P. T., 1991, "Texture Analysis of Rough Surfaces Using Optical Fourier Transform," *Measurement Science and Technology*, Vol. 2, pp.831-837.

Inasaki, I., 1982, "Development of In-Process Sensor for Surface Roughness Measurement," *Proceedings of the 23rd International Machine Tool Design and Research Conference*, B. J. Davis, ed., pp.109-113.

Jahnke, E., and Emde, F., 1945, *Table of Functions with Formulae and Curves*, 4th ed., Dover Publications, New York.

Jansson, D. G., and Bourke, J. M., and Bell, A. C., 1984, "High Speed Surface Roughness Measurement," *ASME Journal of Engineering for Industry*, Vol. 106, No. 2, pp.34-39.

Kurita, M., Sato, M., and Nakano, K., 1992, "A Technique for Rapidly Measuring Surface Roughness Using a Laser," *JSME International Journal, Series I: Solid Mechanics, Strength of Materials*, Vol. 35, No. 3, pp.335-339.

- Luk, F., Huynh, V. M., and North, W. P. T., 1989, "Measurement of Surface Roughness by a Machine Vision System," *Journal of Physics, E: Scientific Instrument*, Vol. 22, pp.977-980.
- Mansfield, D., 1992, "Surface Characterization via Optical Diffraction," *International Journal of Machine Tool and Manufacture*, Vol. 32, No. 12, pp.11-17.
- Mason, F., 1990, "Keeping a Check on Disk-Drive Heads," *Photonics Spectra*, Vol. 24, No. 11, pp.91-91.
- Marx, E., and Vorburger, T. V., 1990, "Direct and Inverse Problems for Light Scattered by Rough Surfaces," *Applied Optics*, Vol. 29, No. 25, pp.3613-3626.
- Nayar, S. K., Ikeuchi, K., and Kanada, T., 1991, "Surface Reflection: Physical and Geometrical Perspectives," *IEEE Transaction on Pattern Analysis and Machine Intelligence*, Vol. 13, No. 7, pp.611-634.
- North, W. P. T., and Agarwal, A. K., 1983, "Surface Roughness Measurement with Fiber-Optics," *ASME Journal of Dynamic Systems, Measurement, and Control*, Vol. 105, pp.295-297.
- Ogilvy, J. A., 1991, *Theory of Wave Scattering from Random Rough Surfaces*, IOP Publishing Ltd., Techno House, Redcliffe Way, Bristol, England.
- Ohtsubo, J., and Asakura, T., 1975, "Statistical Properties of Speckle Intensity Variations in the Diffraction Field under Illumination of Coherent Light," *Optics Communications*, Vol. 14, No. 1, pp.30-34.
- Pandit, S. M., and Shunmugan, M. S., 1992, "Signature of Machine Tool Errors on Surface Texture by DDS," *ASME Journal of Engineering for Industry*, Vol. 114, pp.370-374.
- Peters, J., Vanherck, P., and Sastrodinoto, M., 1979, "Assessment of Surface Typology Analysis Techniques," *CIRP Annals*, Vol. 28, No. 2, pp.539-554.
- Raja, J., 1983, "Field Testing of Machine Tool Diagnostic Techniques Using Surface Metrology," *CIRP Annals*, Vol. 32, No. 1, pp.503-506.
- Rakels, J. H., 1988, "Recognized Surface Finish Parameters Obtained from Diffraction Patterns of Rough Surfaces," *Surface Measurement and Characterization*, SPIE Vol. 1009, pp.119-125.
- Ratcliffe, J. A., 1956, "Some Aspects of Diffraction Theory and Their Application to the Ionosphere," *Reports on Progress in Physics*, Vol. xix, pp.188-267.

- Robinson, G., Perry, D. M., and Peterson, R. W., 1991, "Optical Interferometry of Surfaces," *Scientific American*, July, pp.66-71.
- Roger, A., and Maystre, D., 1980, "Inverse Scattering Method In Electromagnetic Optics: Application to Diffraction Gratings," *Journal of Optical Society of America*, Vol. 70, No. 12, pp.1483-1495.
- Ruffing, B., 1986, "Application of Speckle-Correlation Methods to Surface-roughness Measurement: A Theoretical Study," *Journal of Optical Society of America, A*, Vol. 3, No. 8, pp.1297-1304.
- Sailard, M., and Maystre, D., 1990, "Scattering from Metallic and Dielectric Rough Surfaces," *Journal of Optical Society of America, A*, Vol. 7, No. 6, pp.982-990.
- Sakai, I., and Sawabe, M., 1982, "A Method for Surface Roughness Measurement by Means of Light Reflectance," *Bulletin of Japan Society of Precision Engineers*, Vol. 16, No. 2, pp.123-124.
- Sasaki, O., and Fukuhara, Y., 1985, "Surface Profile Measurement from Intensity of Diffracted Light Using the Phase Retrieval Method," *Applied Optics*, Vol. 24, No. 16, pp.2696-2700.
- Shaw, M. C., 1984, *Metal Cutting Principles*, Clarendon Press, Oxford, U.K..
- Shiraishi, M., 1981, "In-Process Measurement of Surface Roughness in Turning by Laser Beams," *ASME Journal of Engineering for Industry*, Vol. 103, pp.203-209.
- Shiraishi, M., 1987, "A Consideration of Surface Roughness Measurement by Optical Method," *ASME Journal of Engineering for Industry*, Vol. 109, pp.100-105.
- Shiraishi, M., 1988, "Scope of In-Process Measurement, Monitoring and Control Techniques in Machining Processes, Part 1: In-Process Techniques for Tools," *Precision Engineering*, Vol. 10, No. 4, pp.179-189.
- Shiraishi, M., 1989a, "Scope of In-Process Measurement, Monitoring and Control Techniques in Machining Processes, Part 2: In-Process Techniques for Workpieces," *Precision Engineering*, Vol. 11, No. 1, pp.27-37.
- Shiraishi, M., 1989b, "Scope of In-Process Measurement, Monitoring and Control Techniques in Machining Processes, Part 3: In-Process Techniques for Cutting Processes and Machine Tools," *Precision Engineering*, Vol. 11, No. 1, pp.39-47.
- Shiraishi, M., and Sato, K., 1991, "Possibility of Large Roughness Measurement by Laser Speckle," *ASME Journal of Engineering for Industry*, Vol. 113, pp.476-478.

- Spurgeon, D., and Slater, R. A. C., 1974, "In-Process Indication of Surface Roughness Using a Fiber-Optics Transducer," *Proceedings of 15th International Machine Tool Design and Research Conference*, B. Tobias, and F. Koenigsburger, ed., pp.339-347.
- Stover, J. C., 1975, "Roughness Characterization of Smooth Machined Surfaces by Light Scattering," *Applied Optics*, Vol. 14, No. 8, pp.1796-1802.
- Stover, J. C., 1990, *Optical Scattering, Measurement and Analysis*, McGraw-Hill, New York.
- Thomas, T. R., ed., 1982, *Rough Surfaces*, Longman, London, U.K..
- Thwaite, E. G., 1979, "The Direct Measurement of the Power Spectrum of Rough Surfaces by Optical Fourier Transformation," *Wear*, Vol. 57, pp.71-80.
- Thwaite, E. G., 1982, "A Quantitative Comparison of the Wavelength Spectrum of a Surface Obtained by Optical Fourier Transformation with Calculations from Profile Measurements," *Wear*, Vol. 83, pp.181-187.
- TMA Technologies, Inc., 1991, "Light Scatter: A New Light on Quality," *TMA Technical Bulletin*, Vol. 1, No. 2, Bozeman, Montana, U.S.A..
- Uchida, S., Sato, H., and O-hori, M., 1979, "Two Dimensional Measurement of Surface Roughness by the Light Sectioning Method," *CIRP Annals*, Vol. 28, No. 1, pp.419-423.
- Vorburger, T. V., and Teague, E. C., 1981, "Optical Techniques for On-Line Measurement of Surface Topography," *Precision Engineering*, Vol. 3, No. 2, pp.61-83.
- Whitehouse, D. J., Vanherck, P., de Bruin, W., and van Luttervelt, C. A., 1974, "Assessment of Surface Typology Analysis Techniques in Turning," *CIRP Annals*, Vol. 23, No. 2, pp.265-182.
- Whitehouse, D. J., 1987, "Surface Metrology Instrumentation," *Journal of Physics, E: Scientific Instrument*, Vol. 20, pp.1145-1155.
- Zhang, G. M., and Kapoor, S. G., 1991a, "Dynamic Generation of Machined Surfaces, Part I: Description of Random Excitation System," *ASME Journal of Engineering for Industry*, Vol. 113, pp.137-144.
- Zhang, G. M., and Kapoor, S. G., 1991b, "Dynamic Generation of Machined Surfaces, Part II: Construction of Surface Topography," *ASME Journal of Engineering for Industry*, Vol. 113, pp.145-153.
- Zimmerman, J. H., Vorburger, T. V., and Moncarz, H. T., 1988, "Automated Optical Roughness Inspection," *Optical Testing and Metrology II*, SPIE Vol. 954, pp.252-258.

TABLES

Table 1.1 Roughness produced by common production methods

Process	Roughness Average R_a — Micrometers μm (Microinches $\mu in.$)												
	50 (2000)	25 (1000)	12.5 (500)	6.3 (250)	3.2 (125)	1.6 (63)	0.80 (32)	0.40 (16)	0.20 (8)	0.10 (4)	0.05 (2)	0.025 (1)	0.012 (0.5)
Flame cutting		████████											
Snagging		████████	████████										
Sawing		████████	████████	████████	████████								
Planing, shaping			████████	████████	████████	████████							
Drilling				████████	████████	████████							
Chemical milling				████████	████████	████████							
Elect. discharge mach					████████	████████							
Milling				████████	████████	████████	████████						
Broaching					████████	████████	████████						
Reaming					████████	████████	████████						
Electron beam					████████	████████	████████						
Laser					████████	████████	████████						
Electro-chemical					████████	████████	████████	████████					
Boring, turning					████████	████████	████████	████████					
Barrel-finishing							████████	████████					
Electrolytic grinding								████████	████████				
Roller burnishing								████████	████████				
Grinding								████████	████████				
Honing								████████	████████				
Electro-polish								████████	████████				
Polishing								████████	████████				
Lapping								████████	████████				
Superfinishing								████████	████████	████████			
Sand casting		████████											
Hot rolling		████████											
Forging		████████	████████										
Perm mold casting			████████	████████									
Investment casting					████████	████████							
Extruding					████████	████████							
Cold rolling, drawing					████████	████████							
Die casting					████████	████████							

The ranges shown above are typical of the processes listed.
Higher or lower values may be obtained under special conditions.

Key ██████████ Average Application
██████████ Less Frequent Application

Source: ANSI Standard B48.1

Table 1.2 Various attributes of surface roughness measurement techniques

Technique	Resolution (μm)	Range (μm)	Speed	Environmental sensitivity	Application area	Cost Fixed	Operating
<i>Line scanning</i>							
Stylus	1 (H) 0.05 (V)	< 100	Low	High	Lab	Medium	High
Interferometer	2 (H) 0.0001 (V)	< 0.6	Low	High	Lab	High	High
Focus detection	1 (H) 0.001 (V)	n.a.	High	Medium	In-process	Medium	Medium
Shadow graph	2	1-10	High	Medium	In-process	Low	Low
Sectioning	1	2-20	High	Medium	On-line	Low	Low
<i>Area sensing</i>							
Scattering	0.1	1-3 (R_q)	High	Low	On-line	Low	Low
OFT	0.01	< 0.1 (R_q)	Medium	Low	On-line	Medium	Medium
Speckle	0.01	0.01-30 (R_q)	High	Low	On-line	Medium	Medium
Ultrasonic	0.5	< 40 (R_q)	High	Low	In-process	High	Low
Capacitance	1	< 50 (R_q)	High	Low	On-line	Low	Low
Resistance	1	< 50 (R_q)	High	Low	On-time	Low	Low

(H) horizontal or lateral, (V) vertical or height.

Table 5.1 Surface parameters for the sinusoidal profiles used in the calculation

Case	h/λ	Λ/λ
a	1.8	100
b	5.4	50
c	9.2	100
d	15.8	100
e	20.0	100

Table 5.2 Surface roughness data of five turned samples used in the experiment

Sample #	RMS(μm) (Stylus)	Λ (μm) (Stylus)	Λ (μm) (Optical)
1	0.43	---	---
2	1.22	52	52
3	2.08	186	183
4	3.50	228	237
5	4.56	228	231

FIGURES

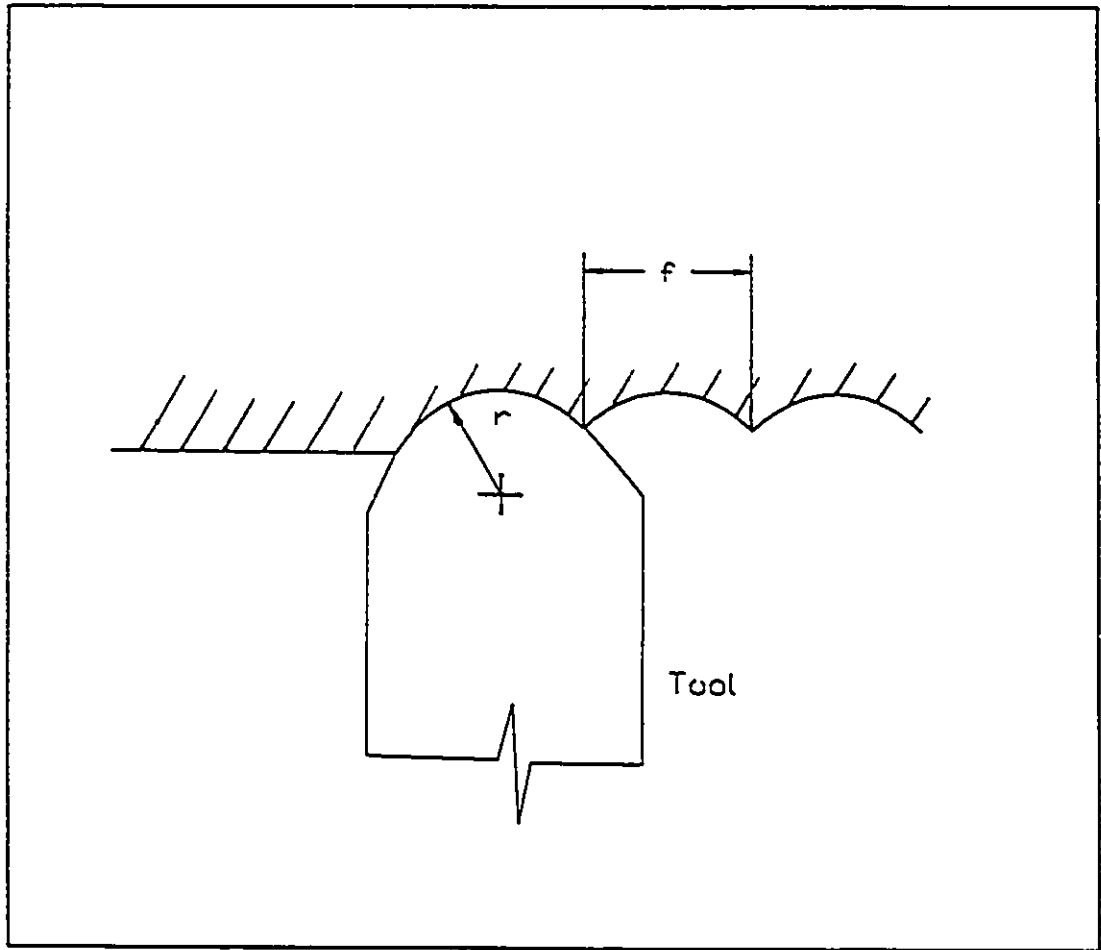


Figure 1.1 Turned surface generation

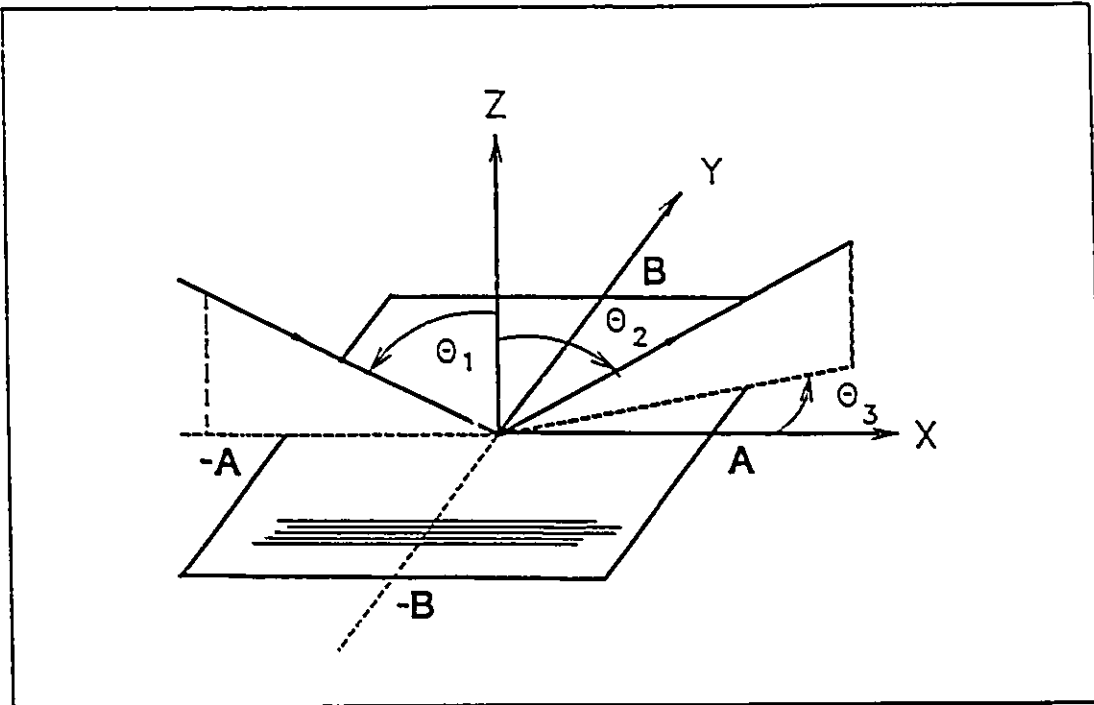


Figure 2.1 General scattering geometry

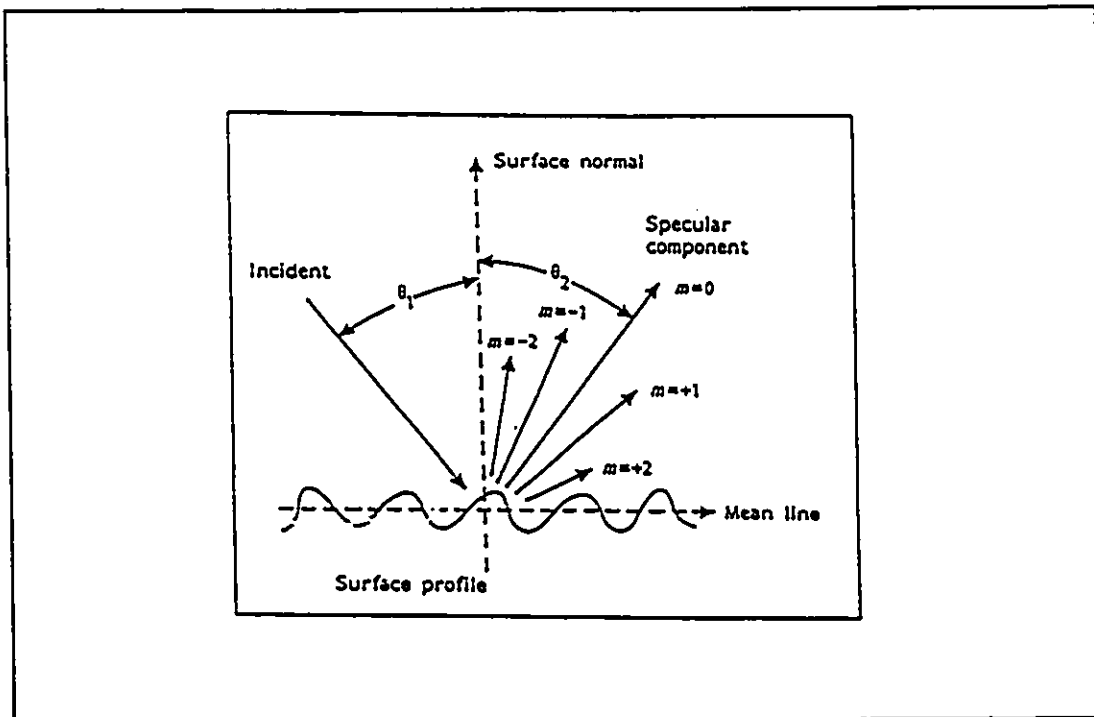


Figure 2.2 Periodic surface scattering pattern

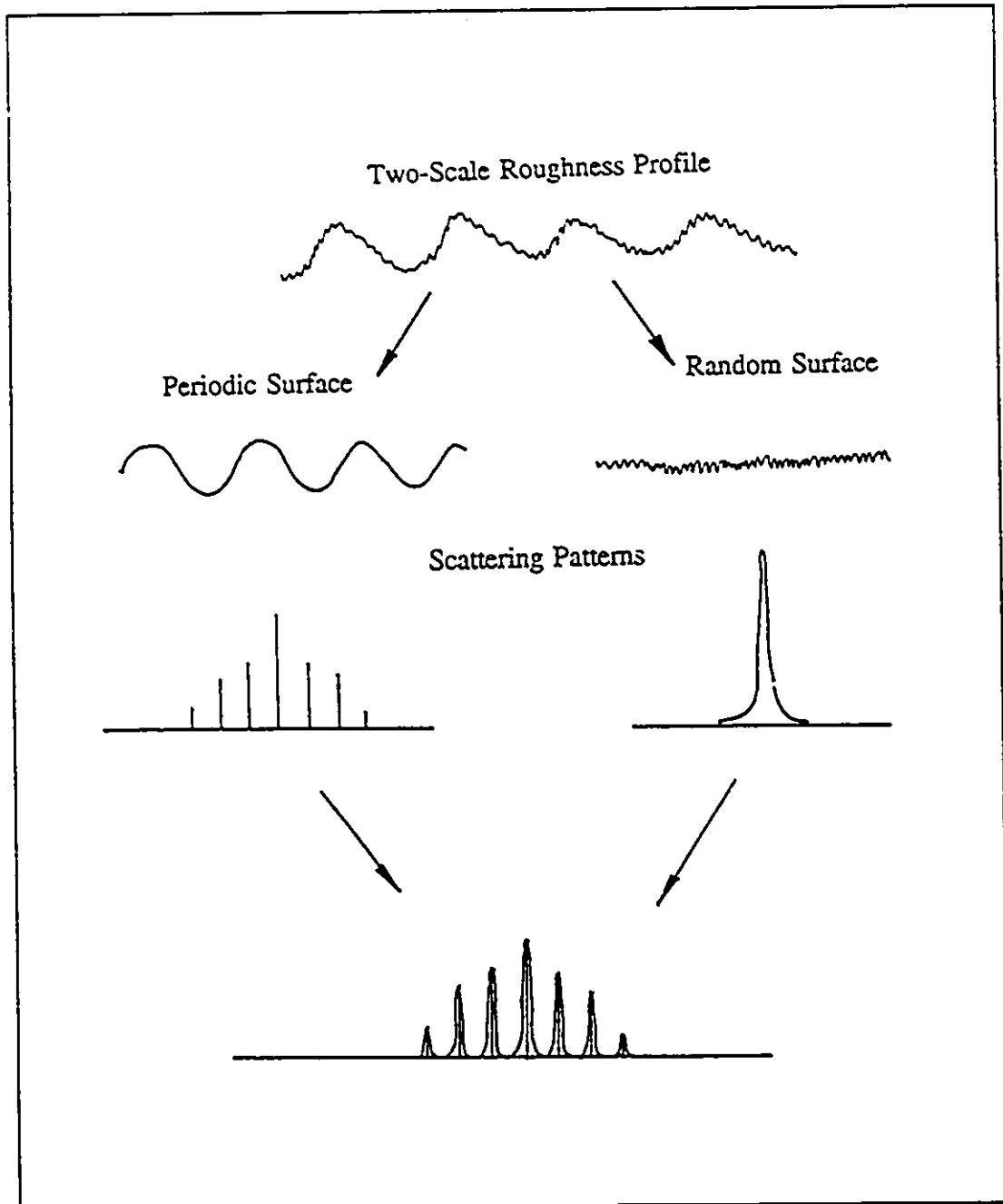


Figure 2.3 Scattering pattern formation from the two-scale surface

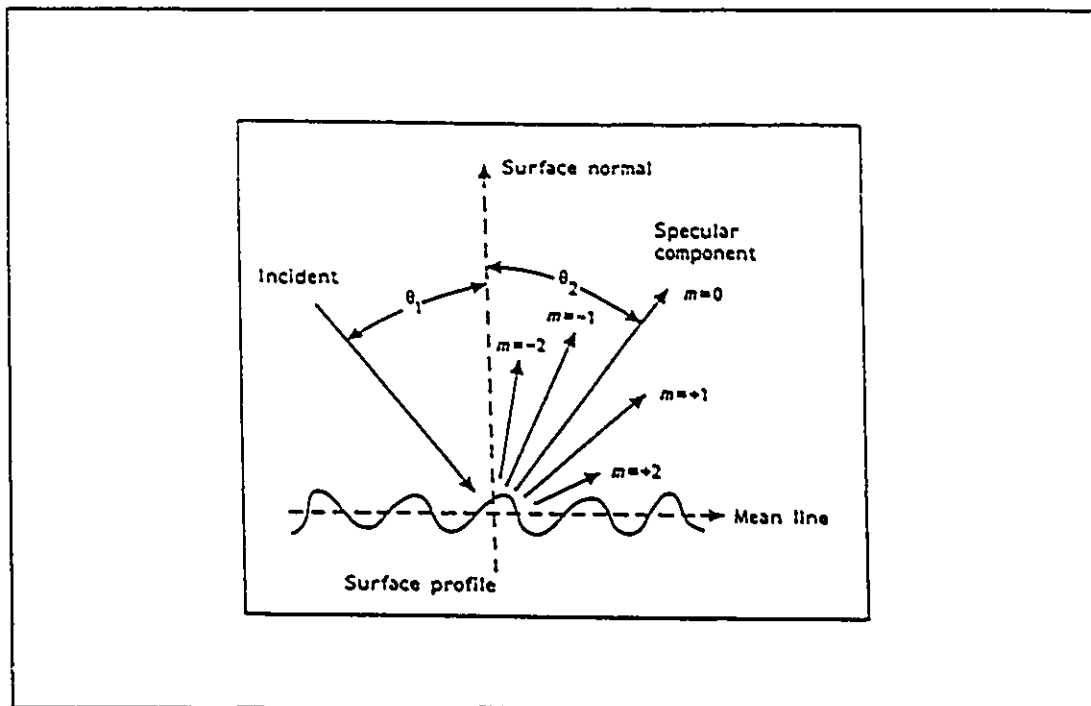


Figure 3.1 Scattering geometry

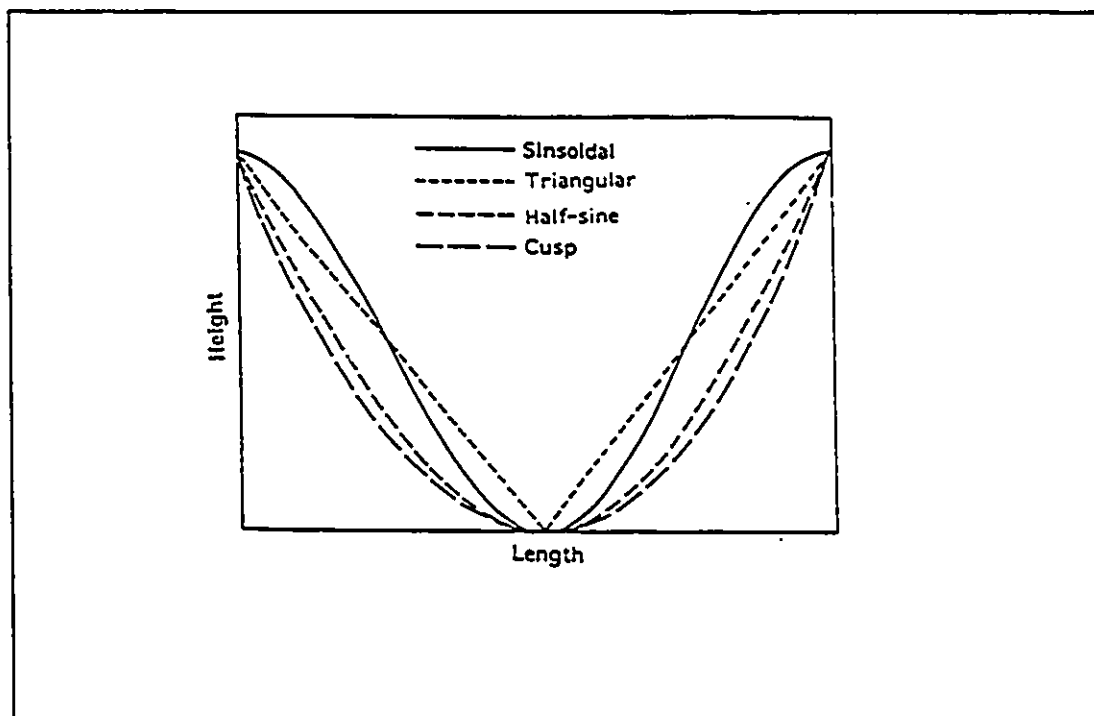


Figure 3.2 Surface profile within one period

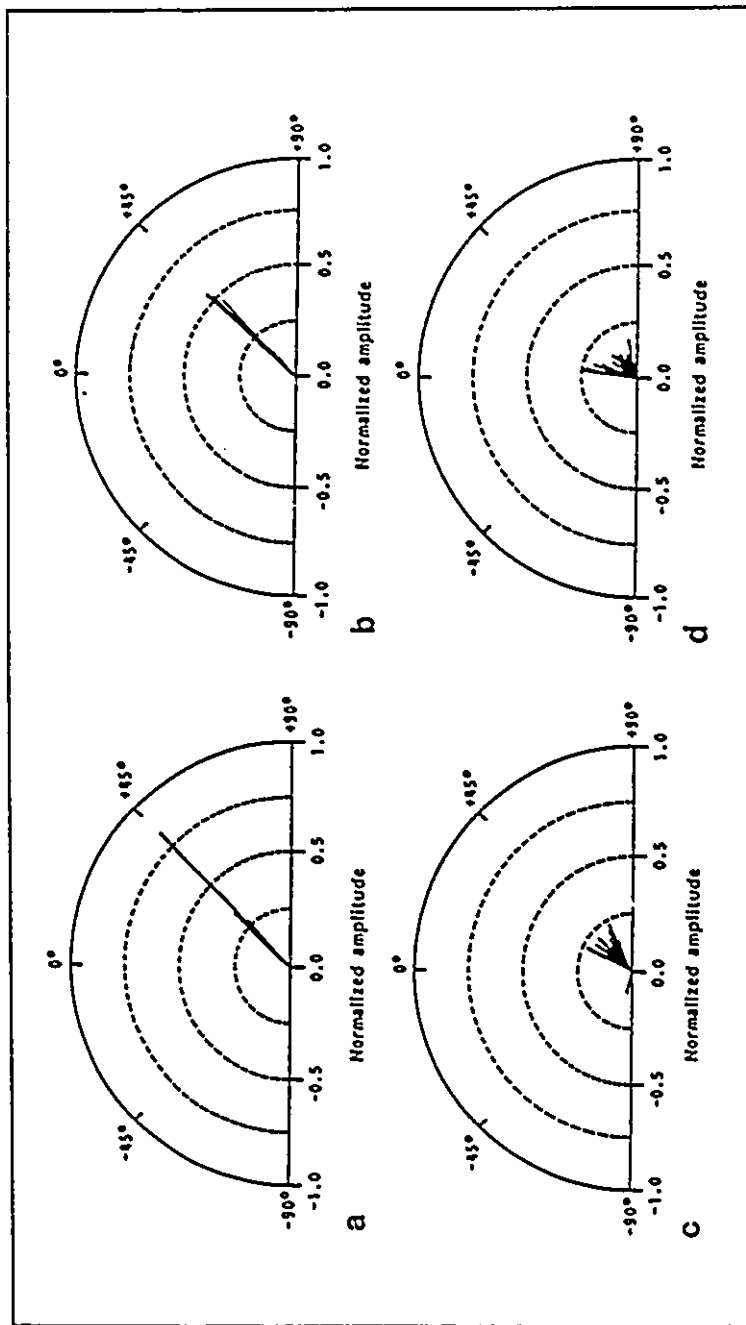


Figure 3.3 Scattering patterns from a sinusoidal surfaces at different roughness for 45° incidence and $30 \mu\text{m}$ surface wavelength: (a) $H=0.12 \mu\text{m}$ (b) $H=0.2 \mu\text{m}$ (c) $H=1.6 \mu\text{m}$ (d) $H=3.2 \mu\text{m}$

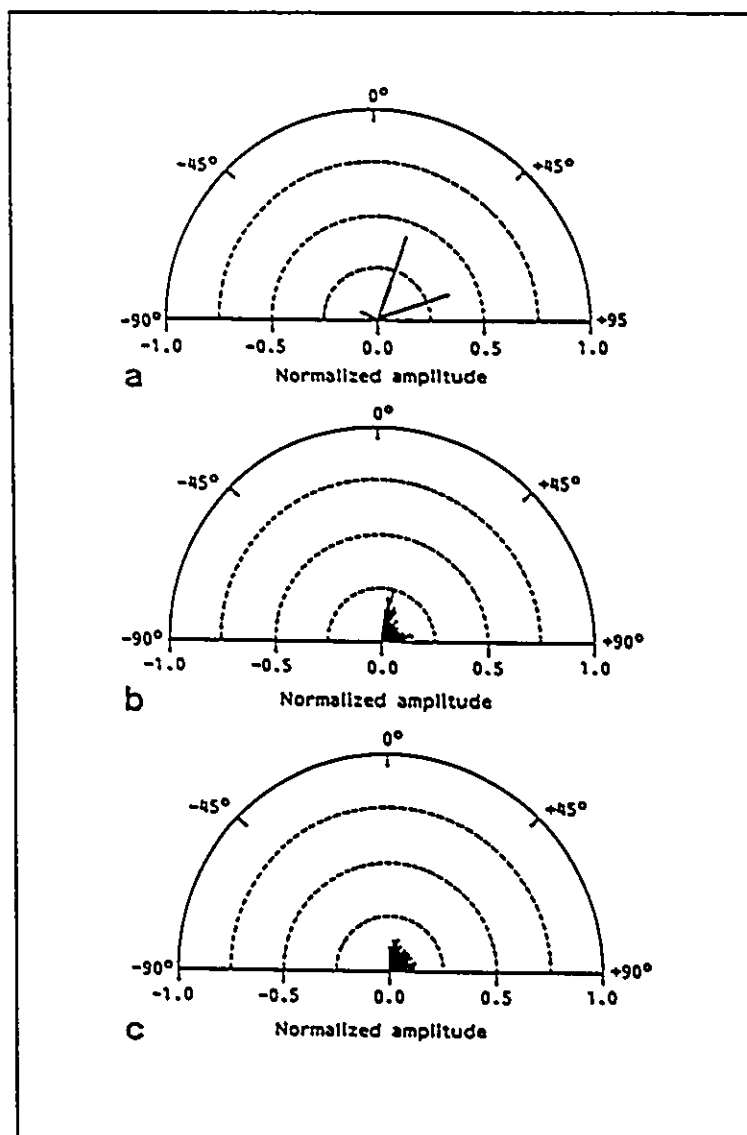


Figure 3.4 Scattering patterns from different profiles for 45° incident angle, $H=3.2 \mu\text{m}$ and $\Lambda=30 \mu\text{m}$ (a) triangular surface (b) half-sine surface (c) cusp surface

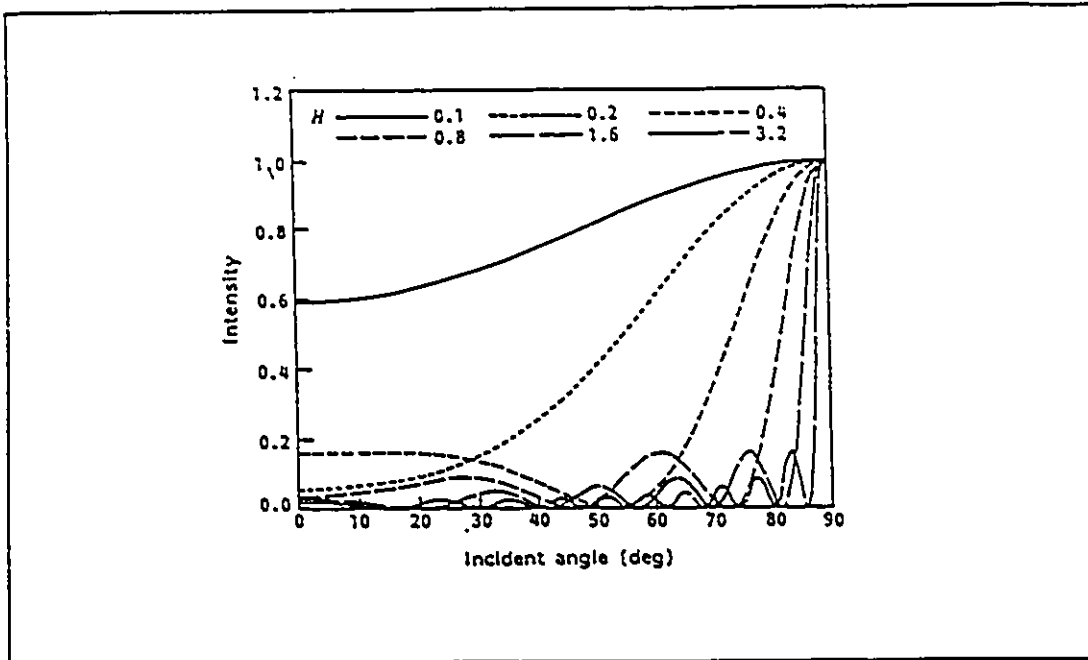


Figure 3.5 Specular component intensity against incident angle for sinusoidal surfaces ($\Lambda/\lambda=47.4$)

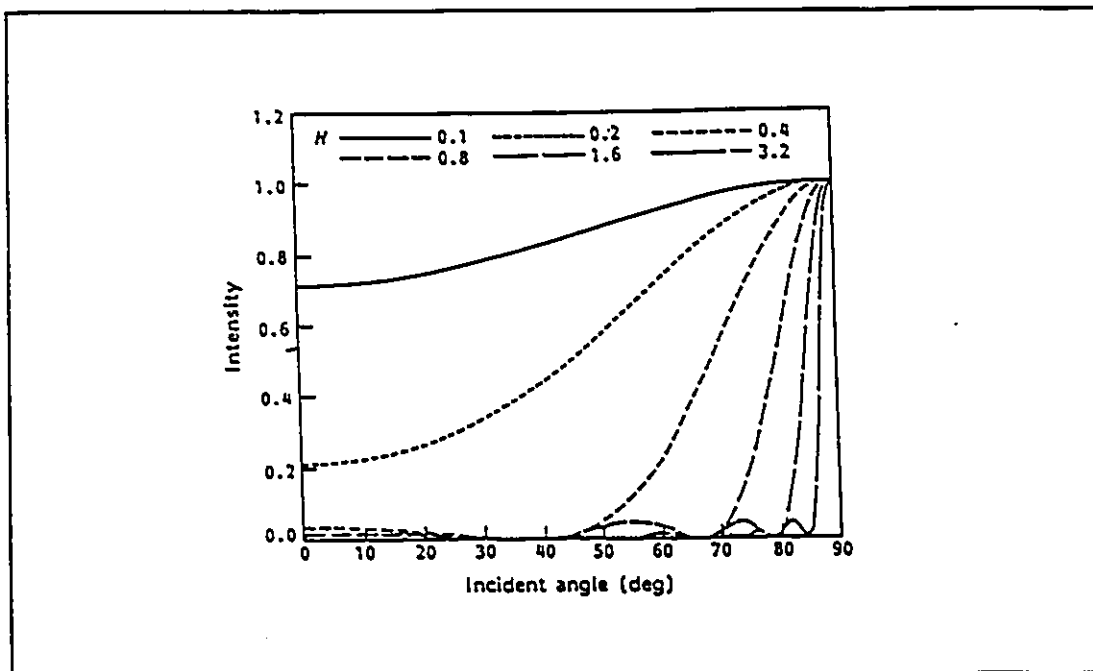


Figure 3.6 Specular component intensity against angle for triangular surfaces ($\Lambda/\lambda=47.4$)

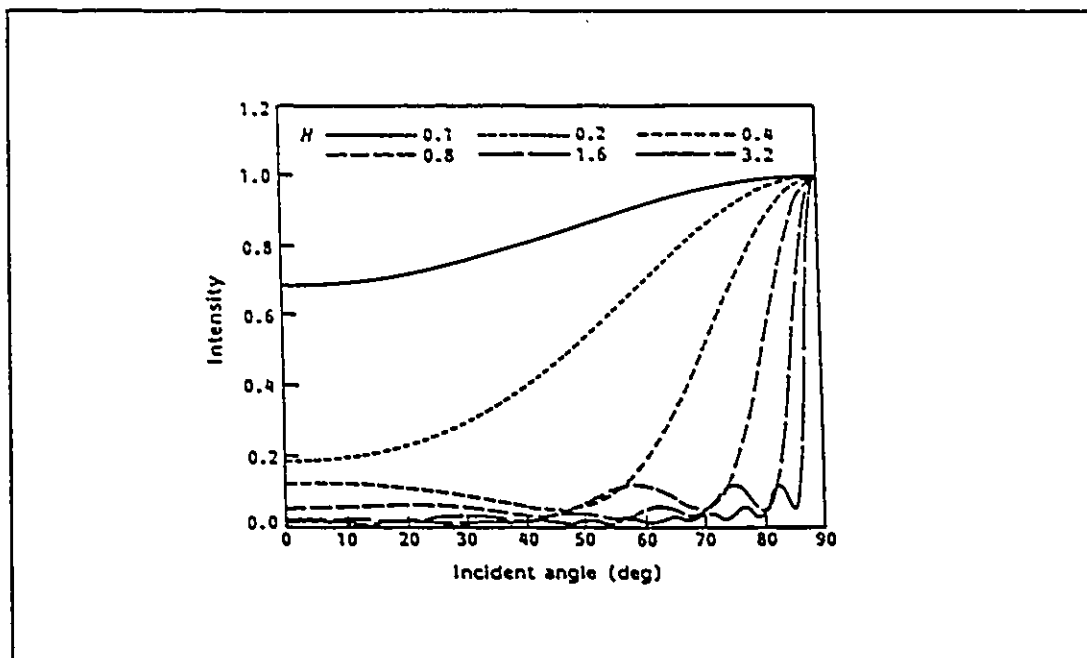


Figure 3.7 Specular component intensity against incident angle for half-sine surfaces ($\Lambda/\lambda=47.4$)

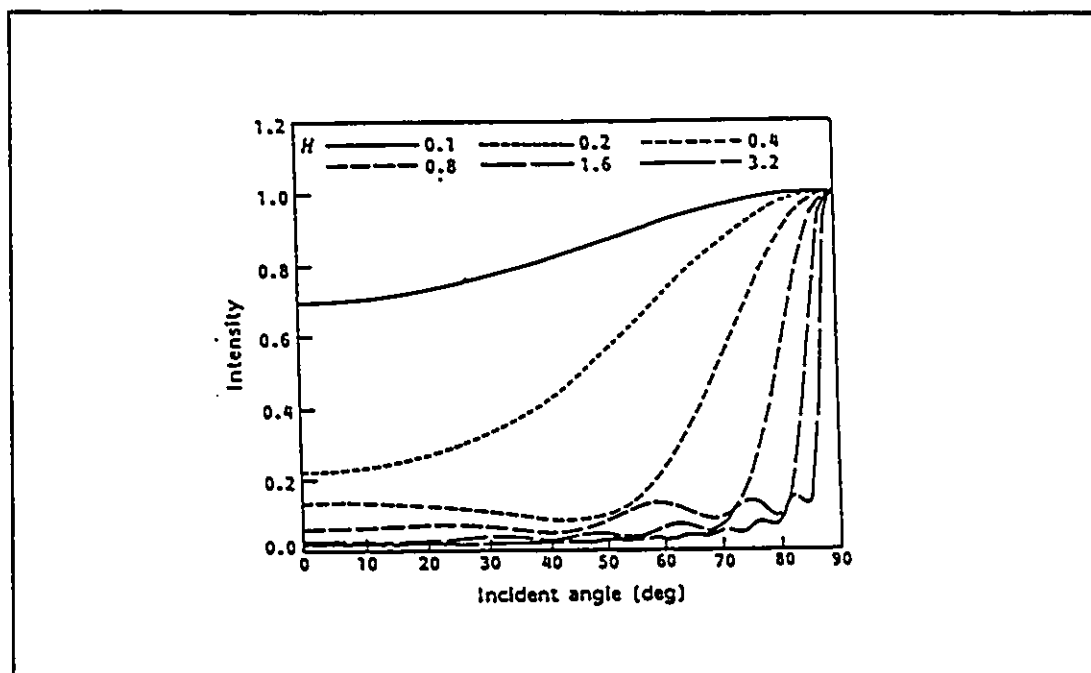


Figure 3.8 Specular component intensity against angle for cusp surfaces ($\Lambda/\lambda=47.4$)

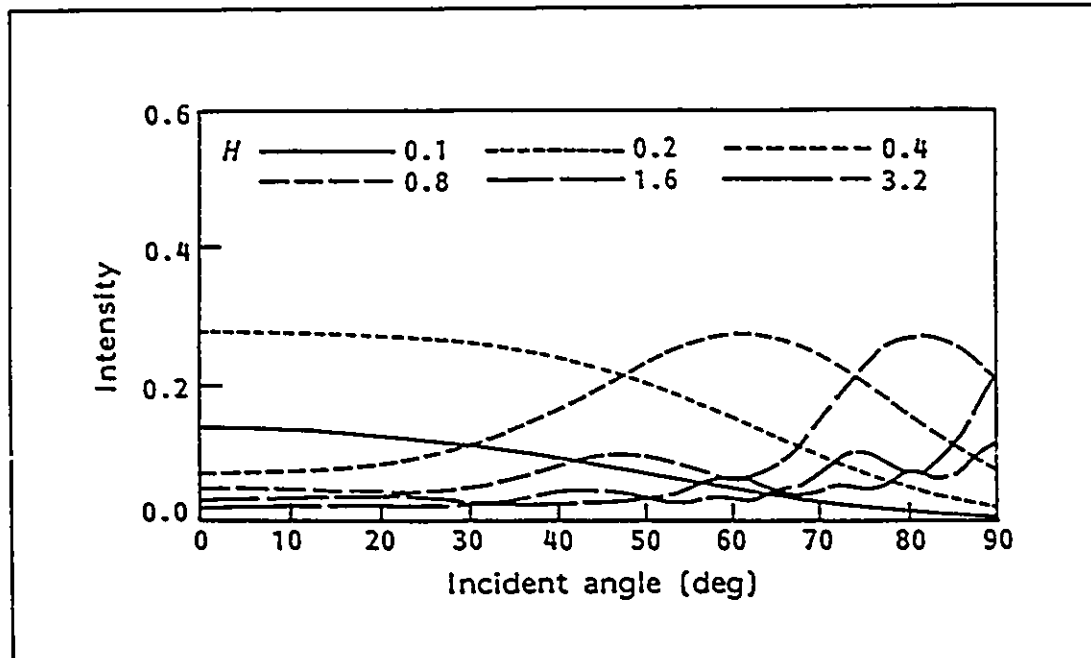


Figure 3.9 First scattering ($m=1$) component intensity against incident angle for cusp surfaces ($\Lambda/\lambda=47.4$)

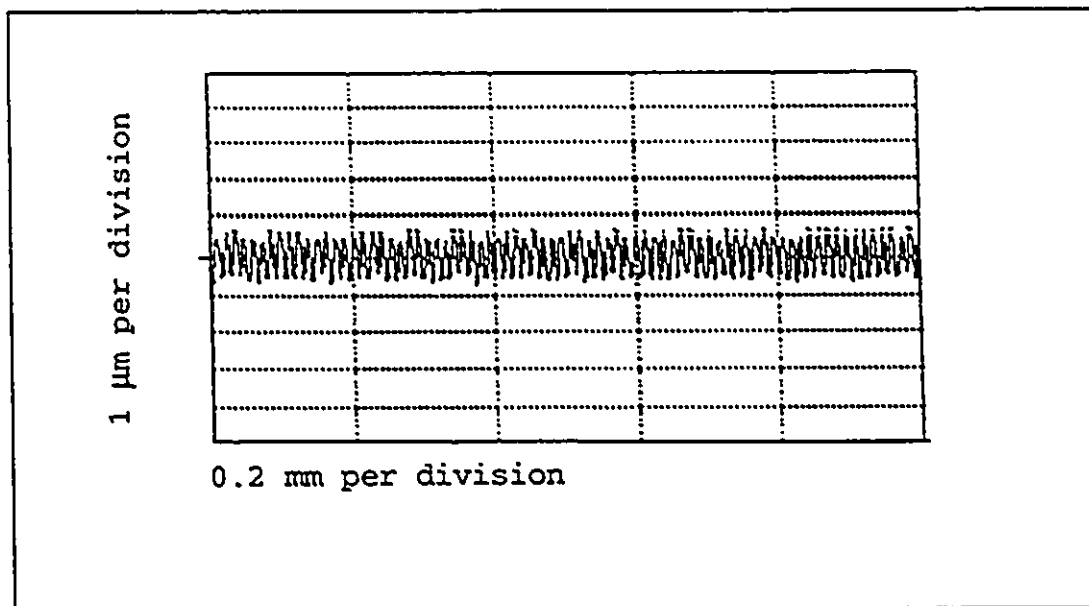


Figure 3.10a Stylus measurement of the GAR standard Sample A

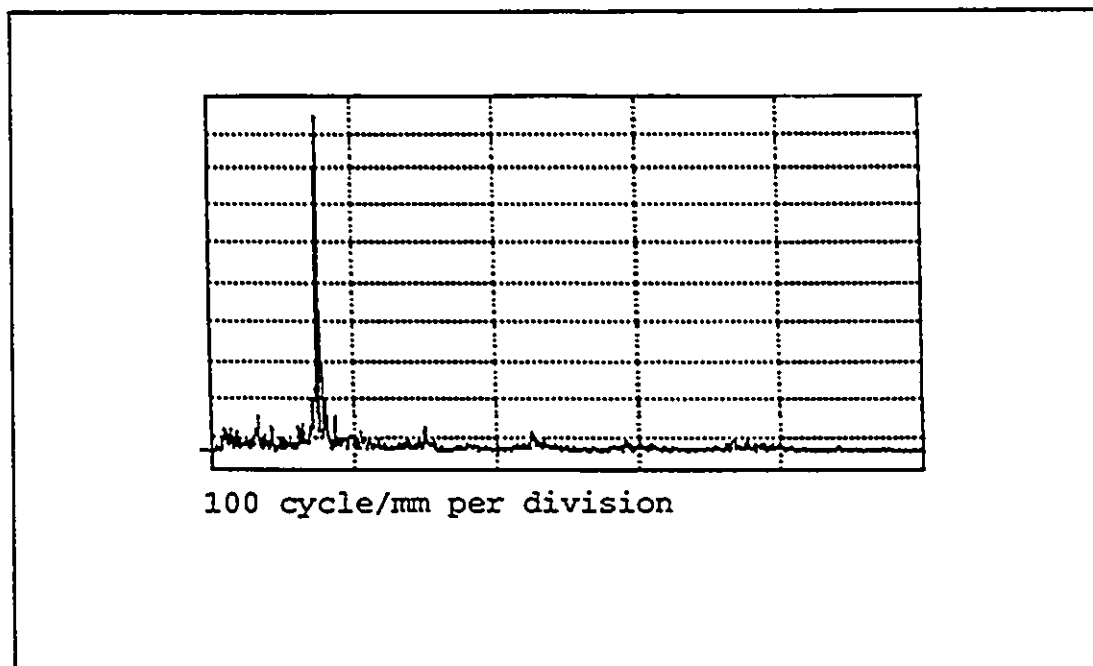


Figure 3.10b Frequency spectrum of the Sample A

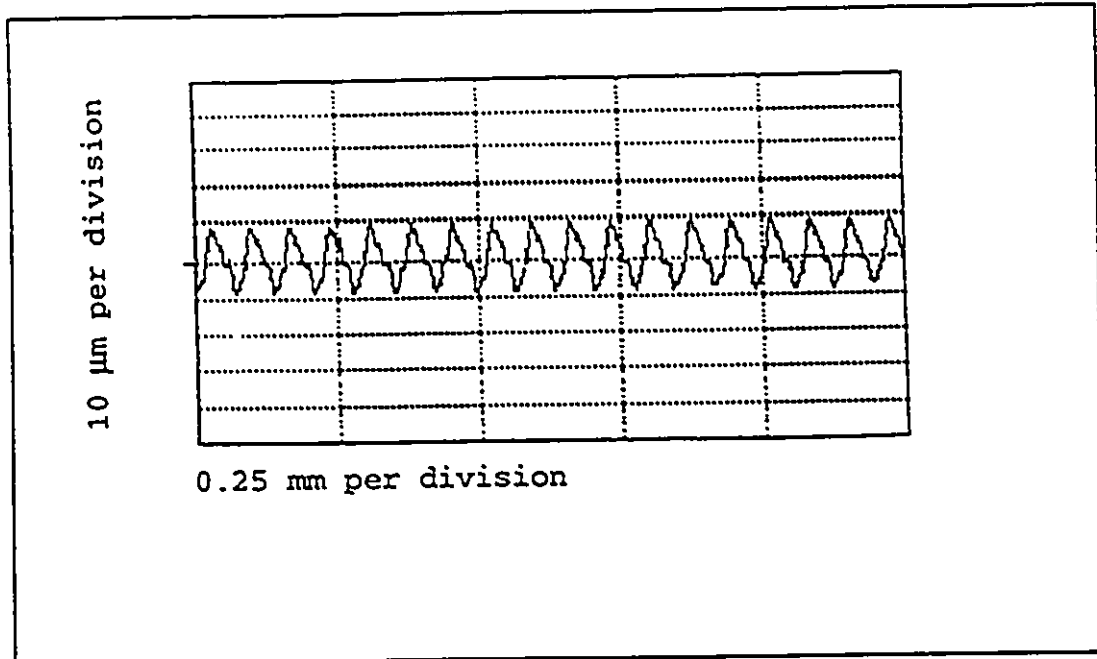


Figure 3.10c Stylus measurement of the GAR standard Sample B

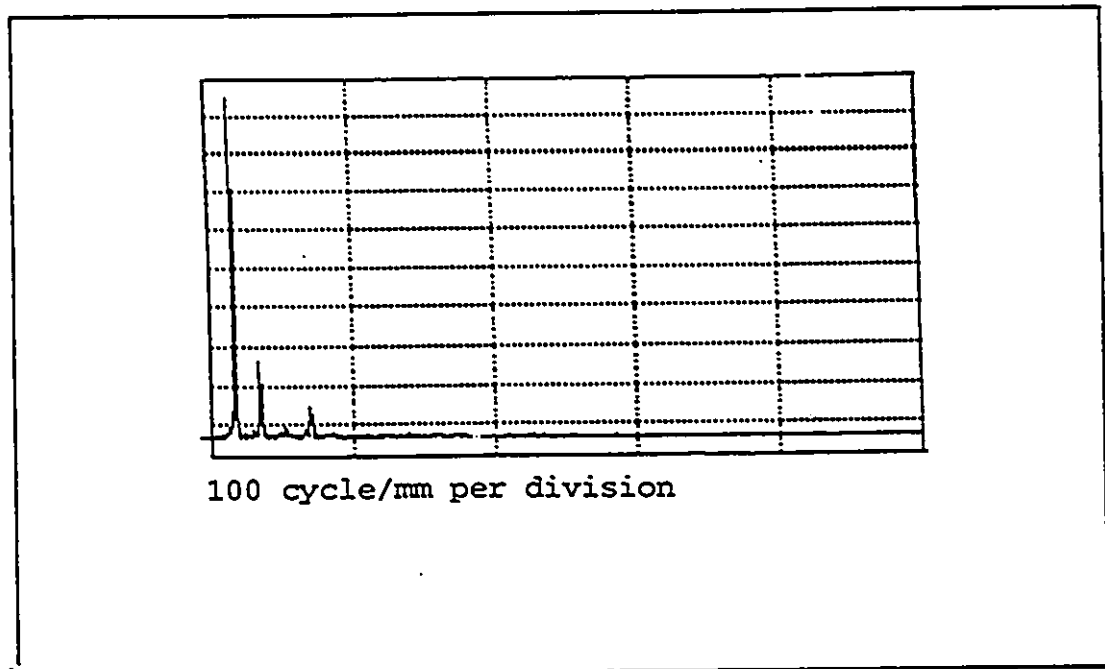


Figure 3.10d Frequency spectrum of Sample B

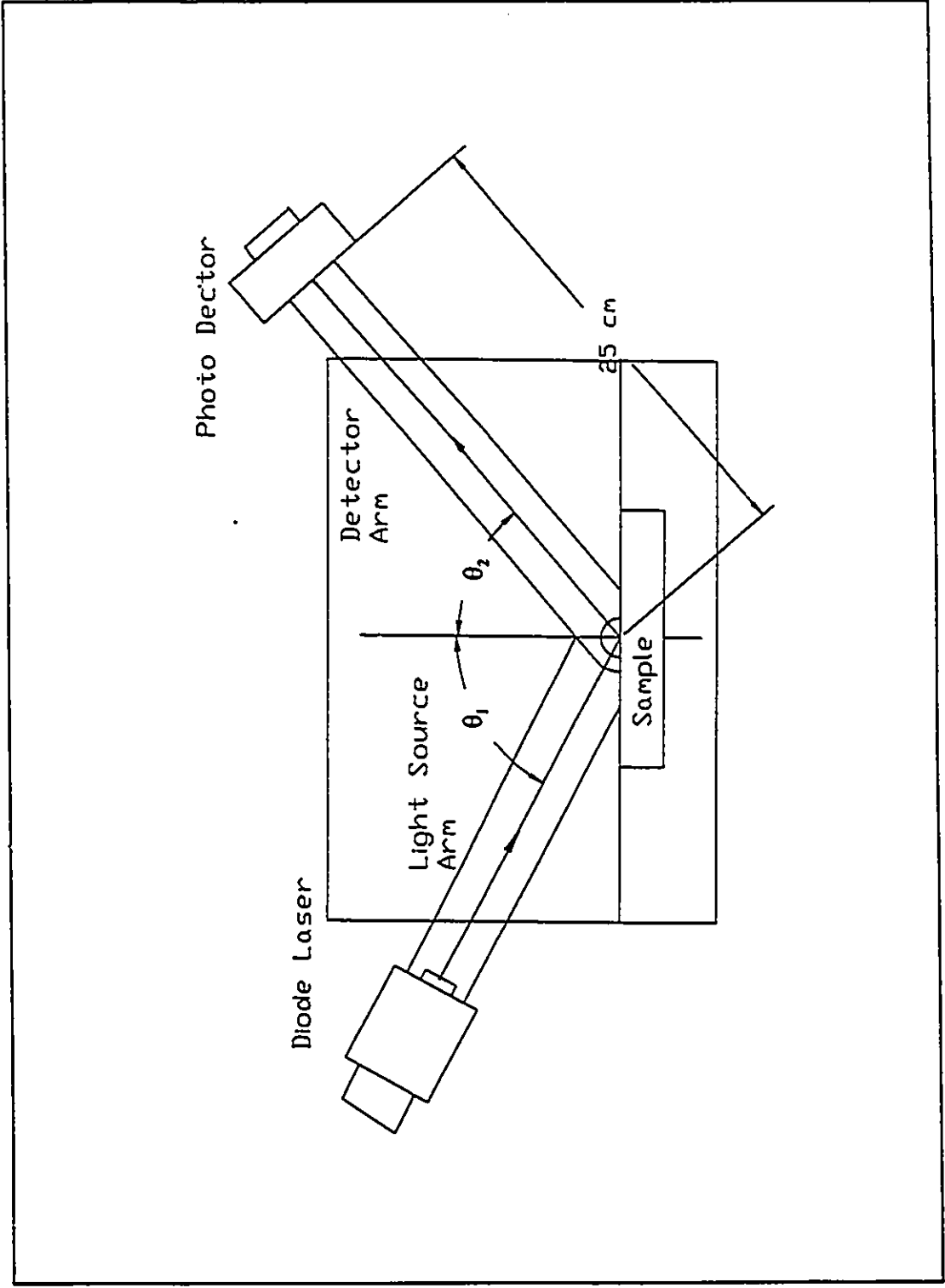


Figure 3.11 The setup for scattering measurement

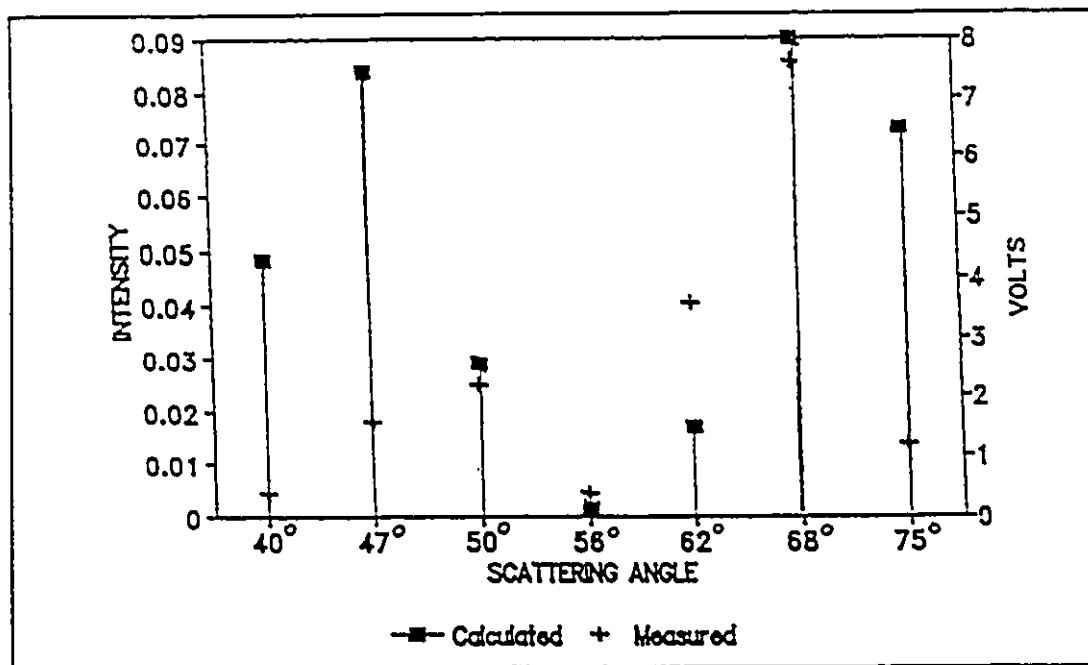


Figure 3.12a Comparison of theoretical and measured scattering pattern of Sample A

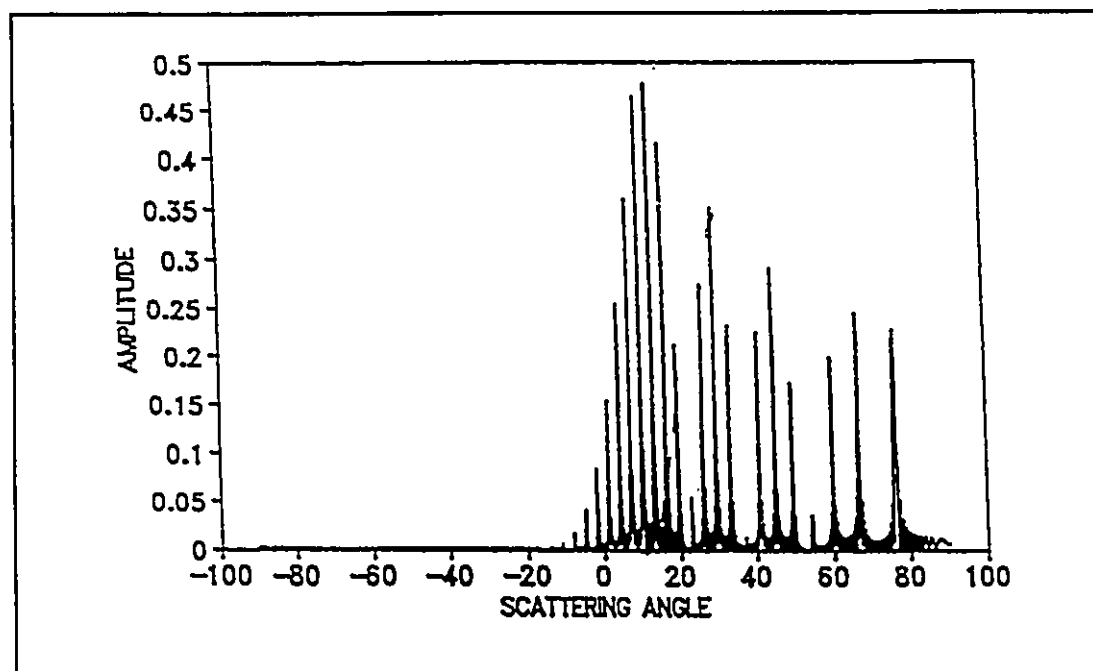


Figure 3.12b Theoretical scattering pattern of Sample A based on the sinusoidal surface approximation

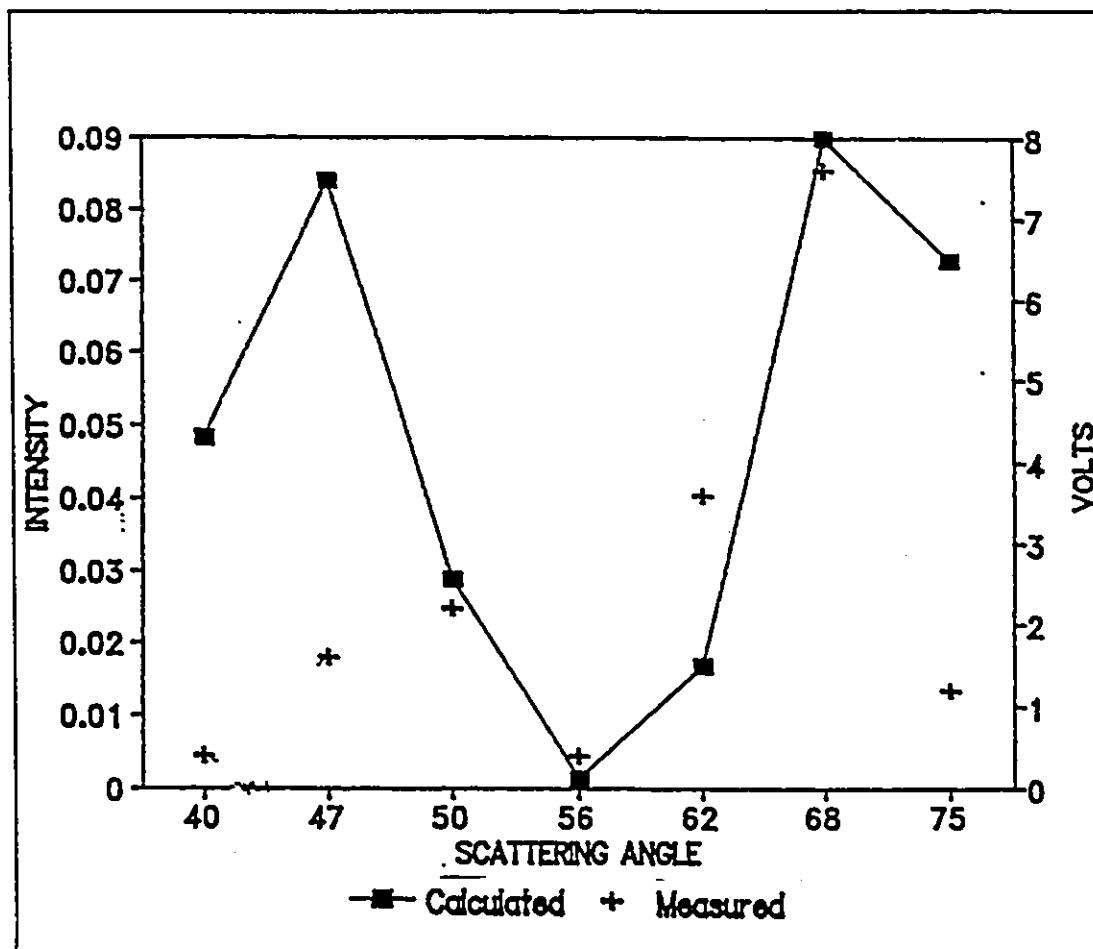


Figure 3.13 Specular intensity versus incident angle

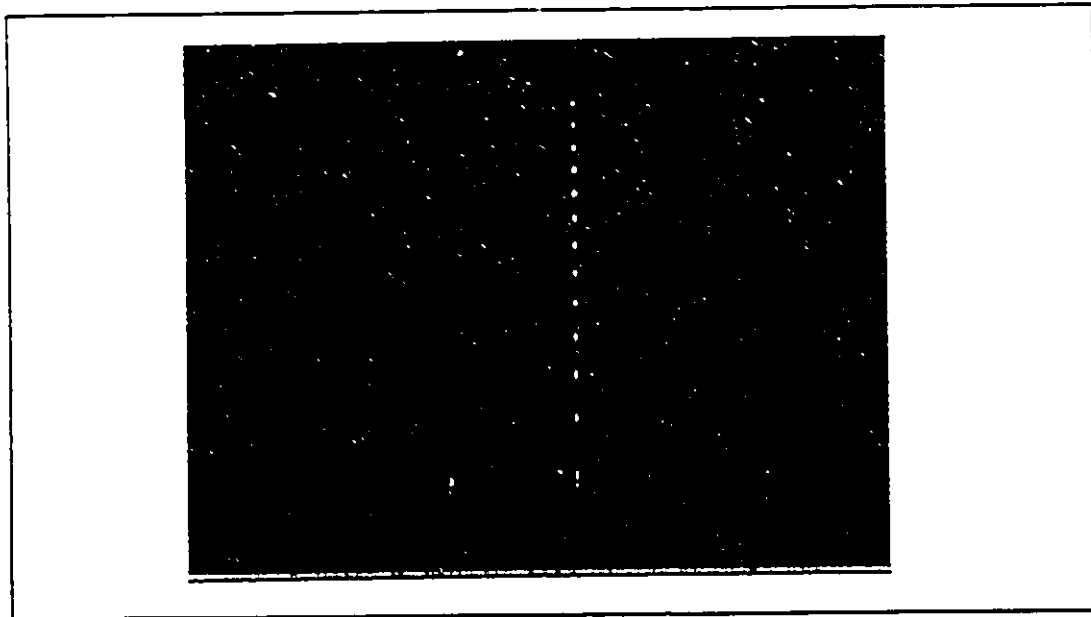


Figure 3.14 Scattering pattern of Sample B

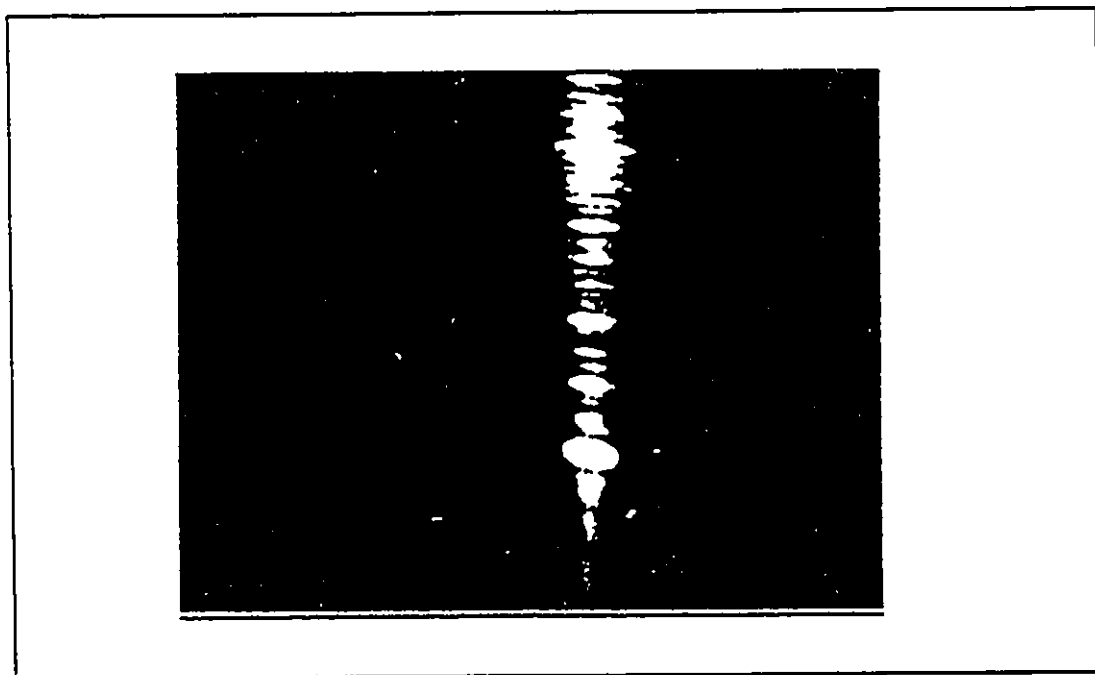


Figure 3.15 Scattering pattern of a hard turned sample

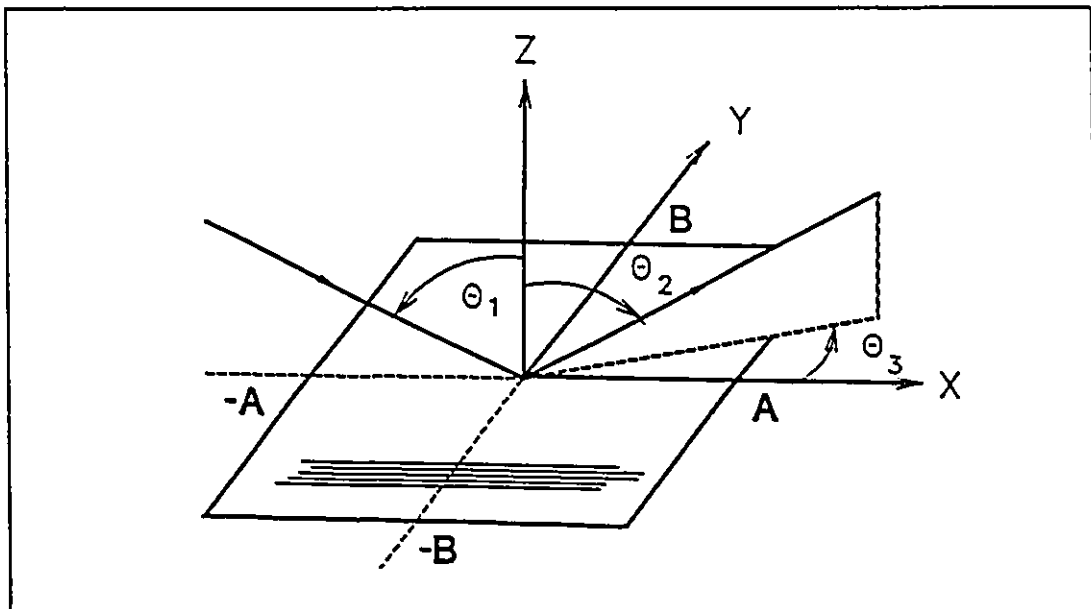


Figure 4.1 A schematic of scattering geometry

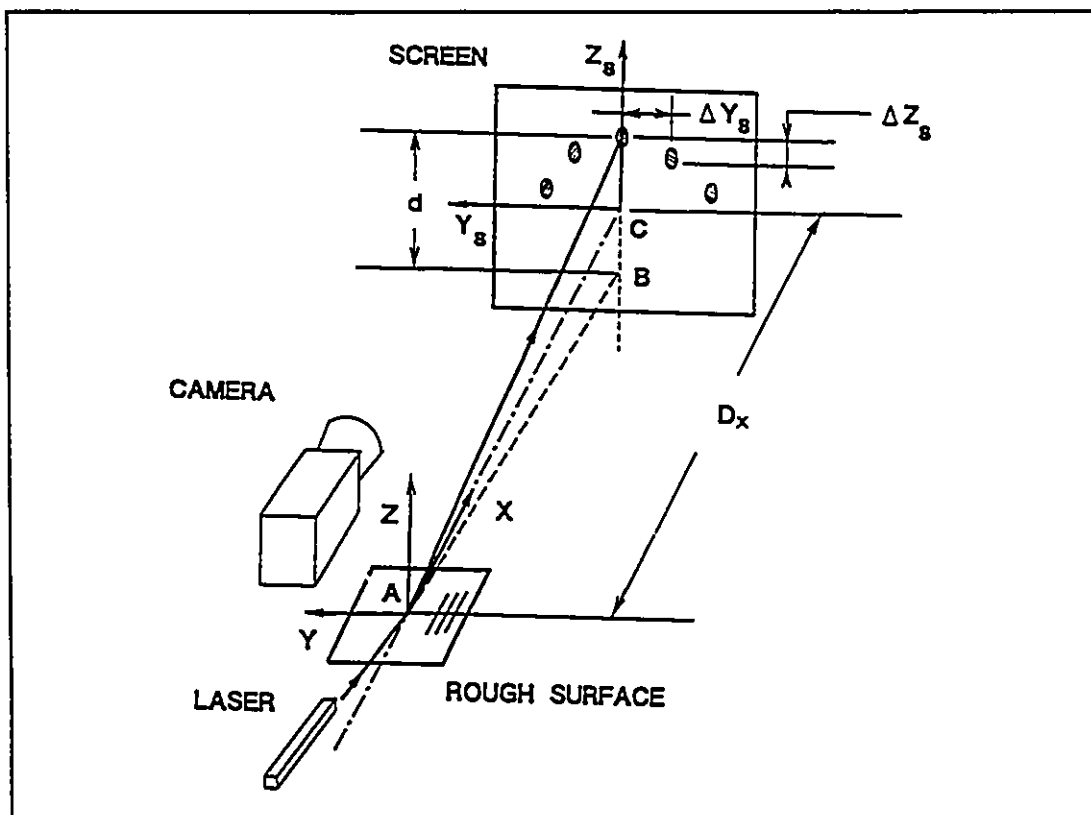


Figure 4.2 Screen coordinate system and the measurement setup

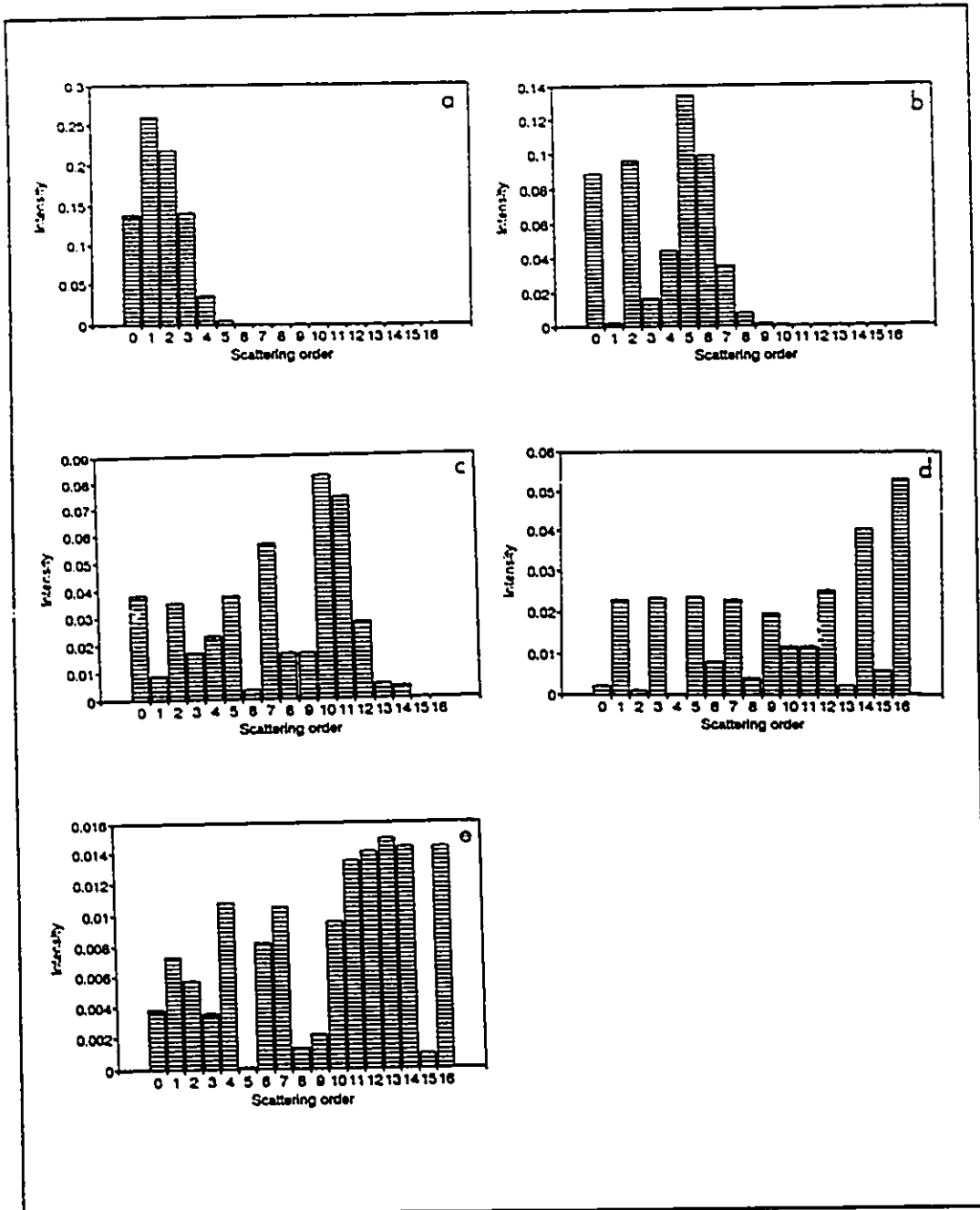


Figure 4.3 Calculated scattering peak intensities for 5 sinusoidal surface of different roughness (a) $H=1 \mu\text{m}$ (b) $H=2 \mu\text{m}$ (c) $H=4 \mu\text{m}$ (d) $H=8 \mu\text{m}$ (e) $H=16 \mu\text{m}$

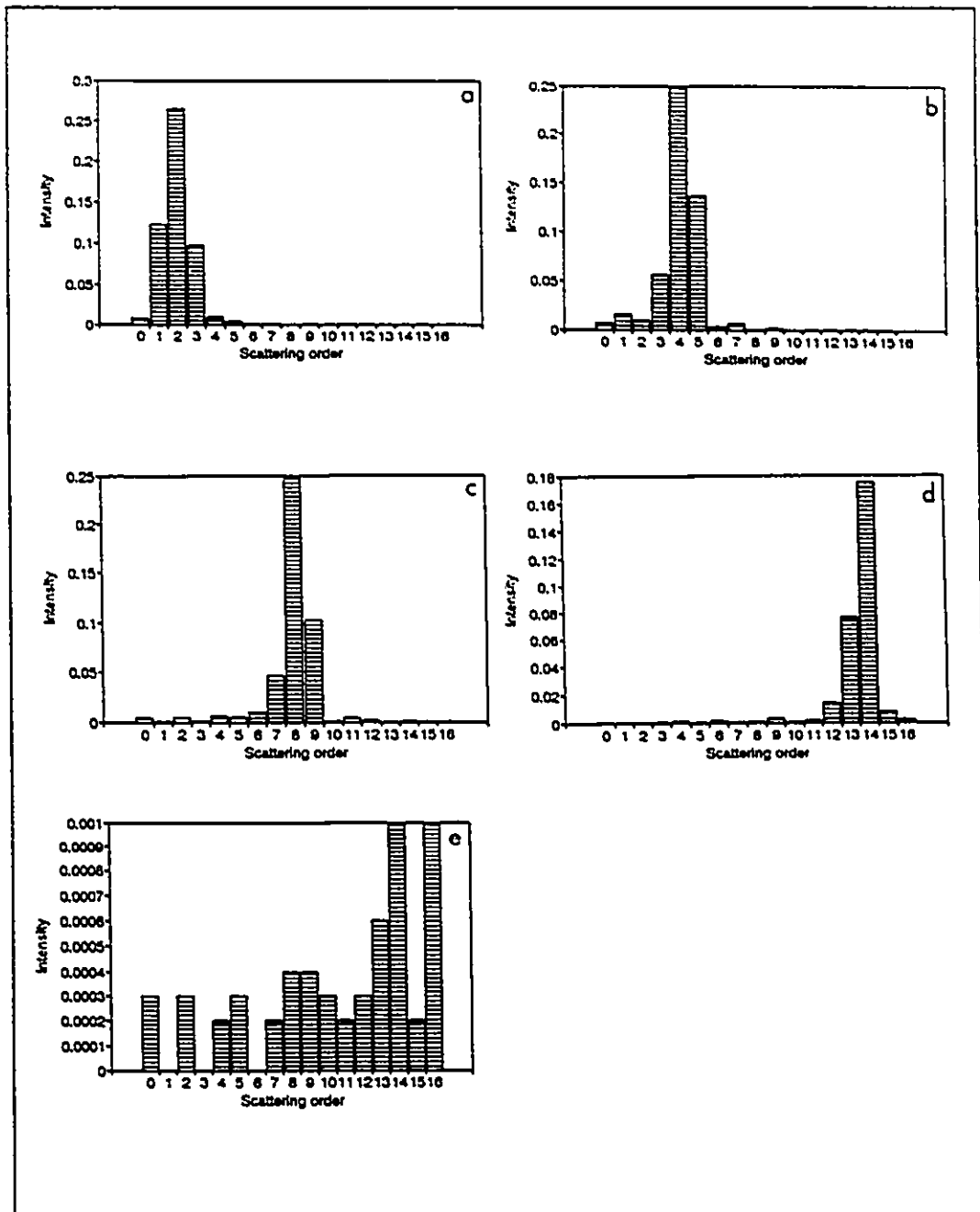


Figure 4.4 Calculated scattering peak intensities for 5 triangular surfaces of different roughness: (a) $H=1 \mu\text{m}$ (b) $H=2 \mu\text{m}$ (c) $H=4 \mu\text{m}$ (d) $H=8 \mu\text{m}$ (e) $H=16 \mu\text{m}$

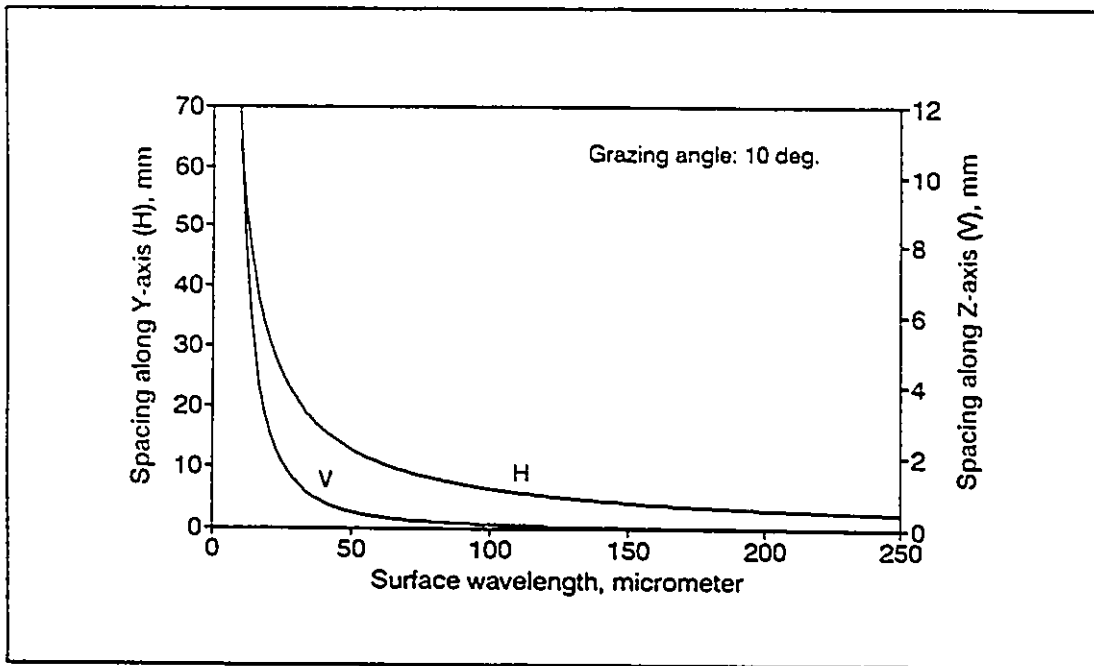


Figure 4.5 Calculated scattering peak spacing versus surface wavelength

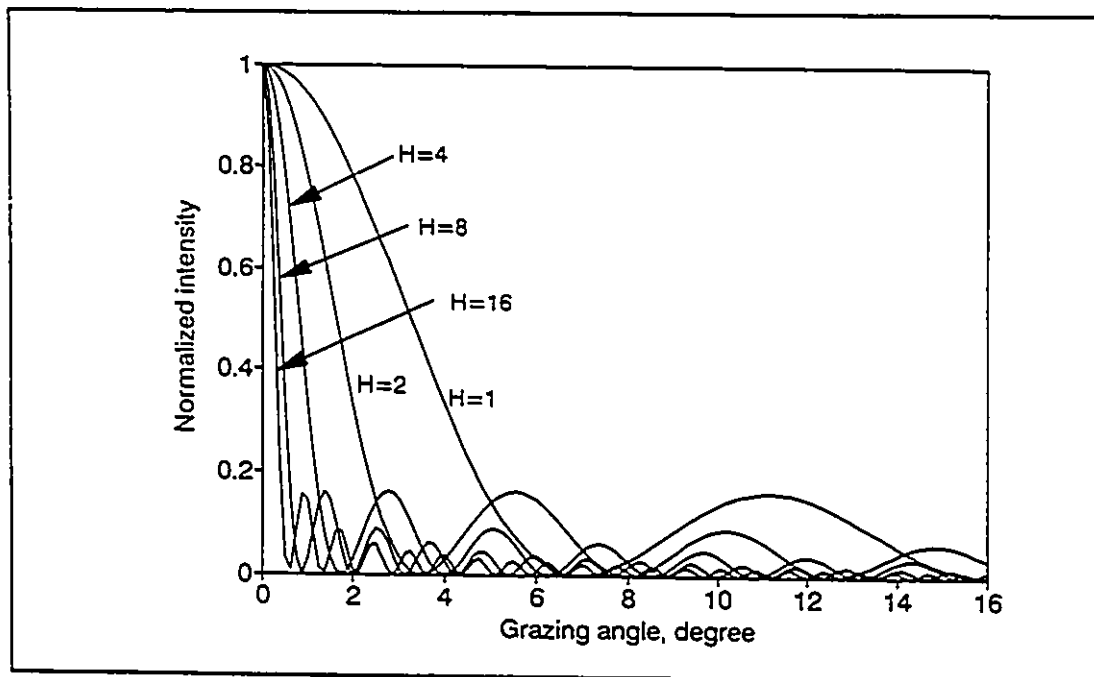


Figure 4.6 Intensity of the zero-order spot versus grazing angle for sinusoidal surface roughness profile

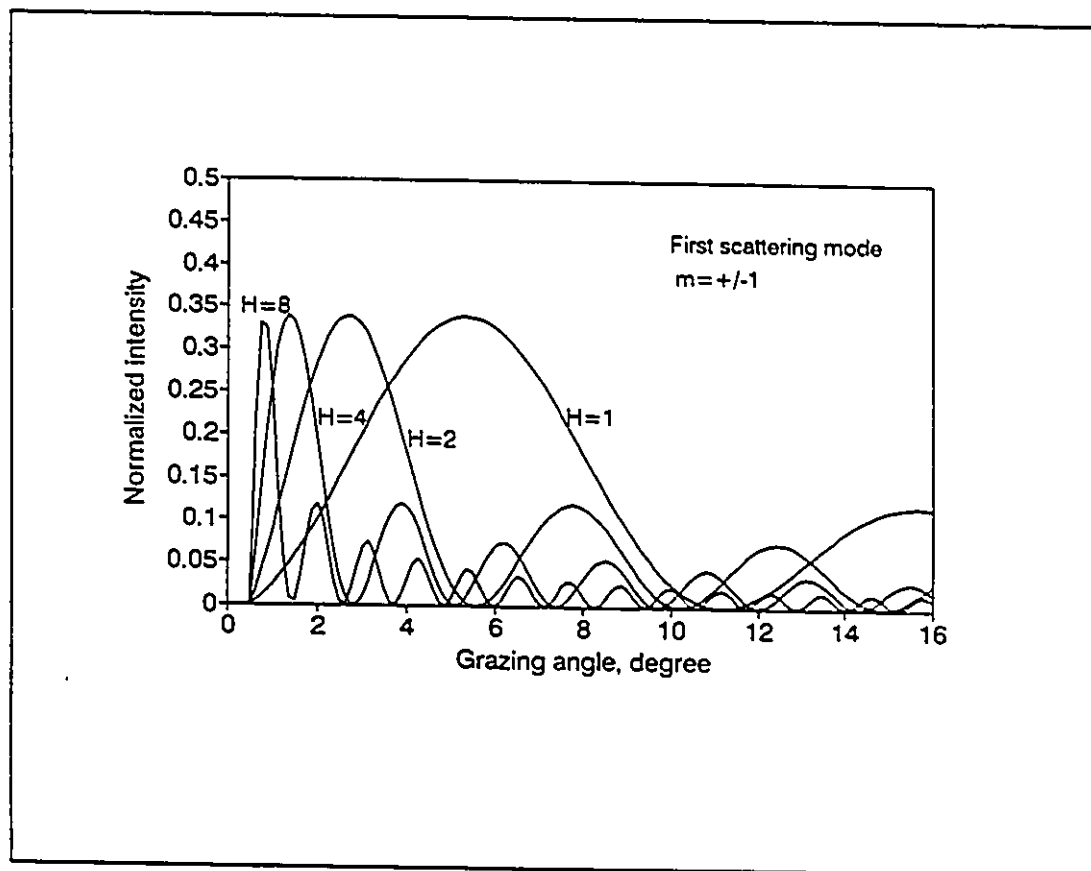


Figure 4.7 Intensity of the first order ($m=1$) spot versus grazing angle for sinusoidal surface roughness profile

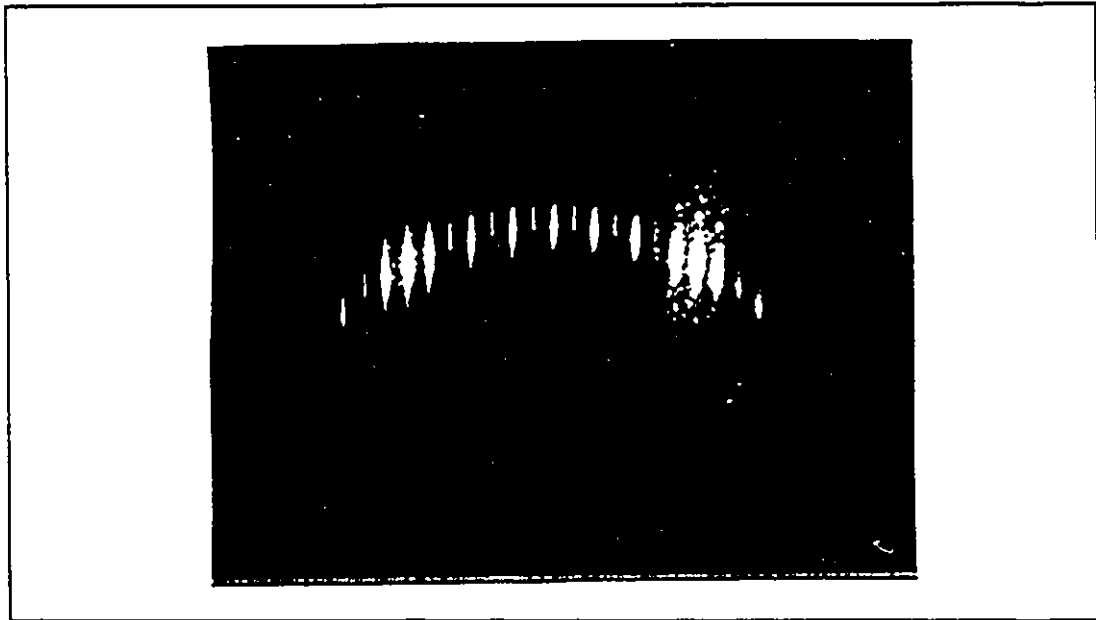


Figure 4.8a, b Photographs of Scattering patterns at 7° grazing angle: (a) Sample A (b) Sample B

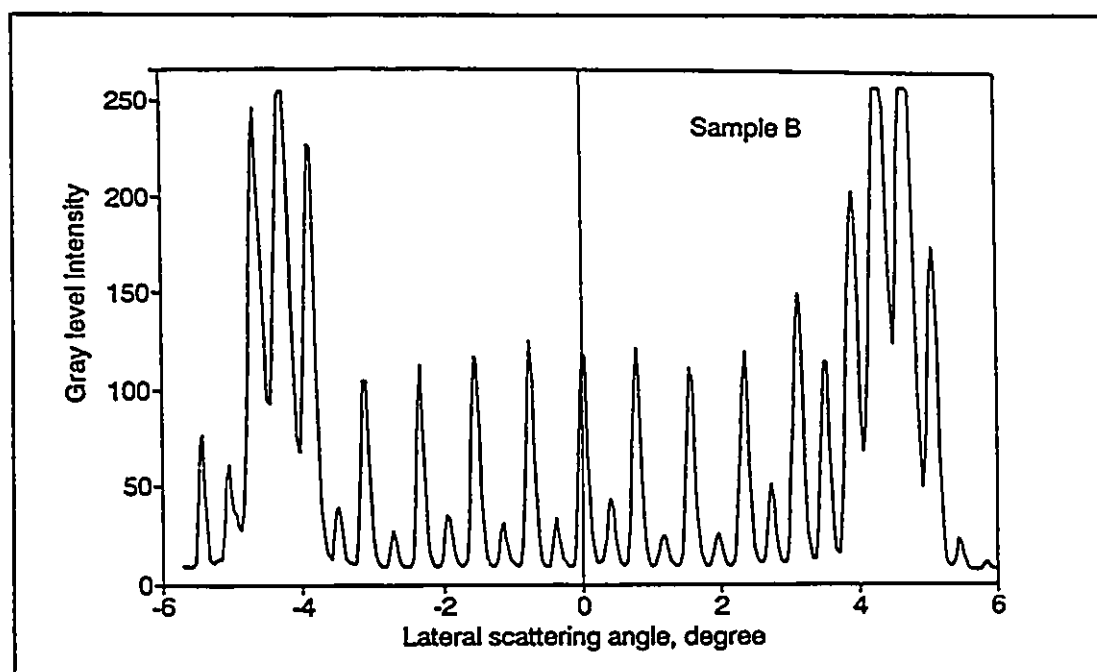
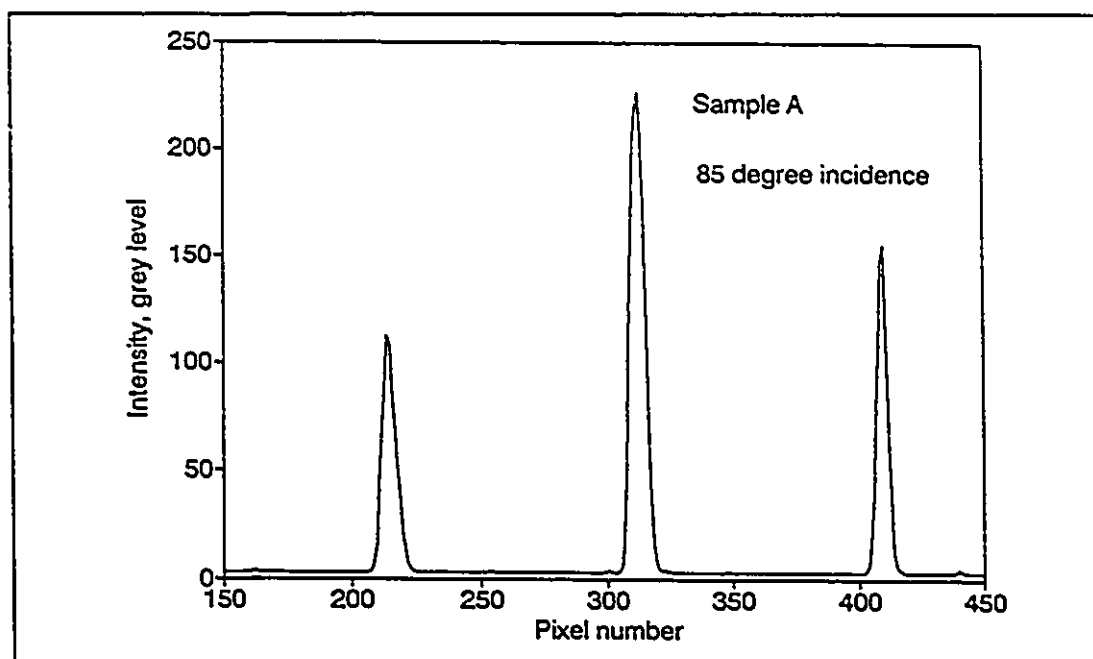


Figure 4.8c, d Intensity profiles of scattering patterns:
(c) Sample A (d) Sample B

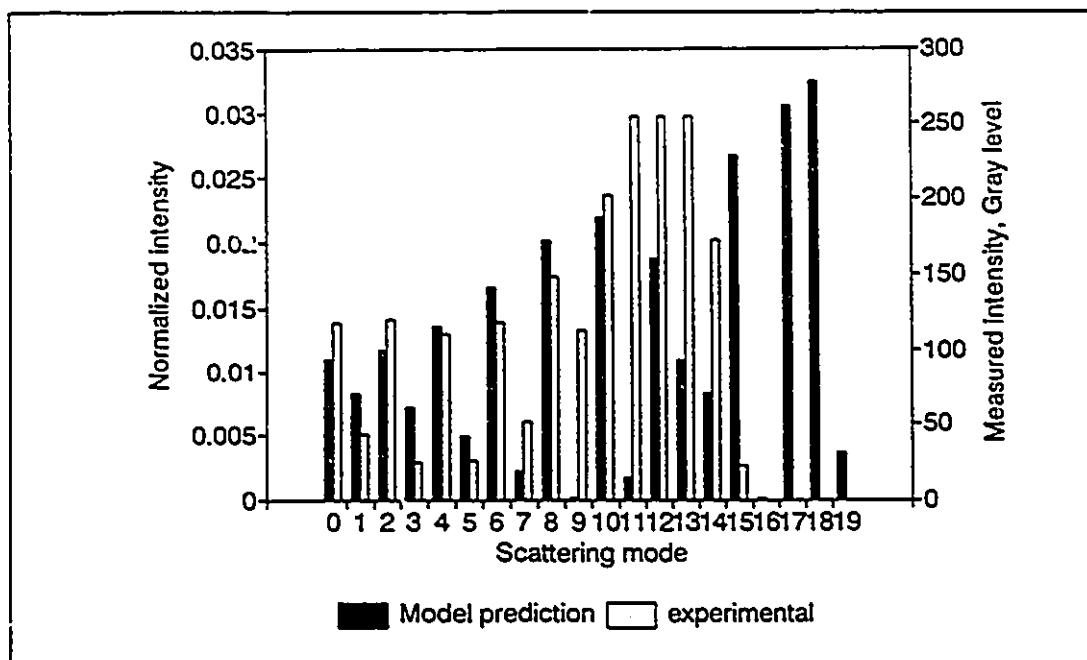


Figure 4.9 Comparison of the measured scattering pattern of Sample A with the predicted pattern

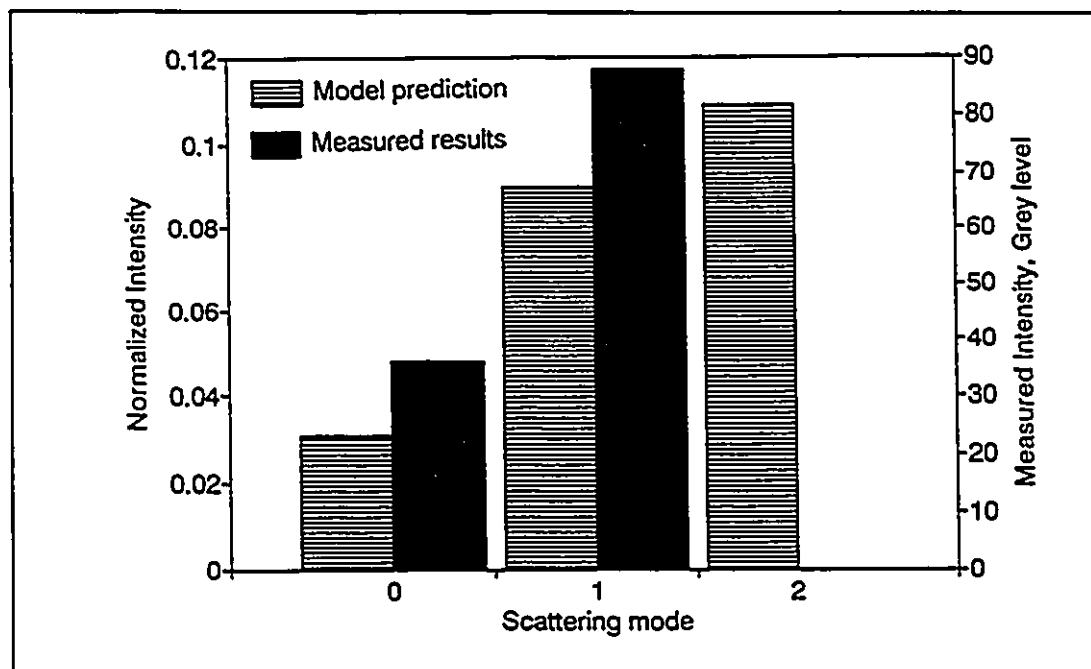


Figure 4.10 Comparison of the measured scattering pattern of Sample B with predicted pattern

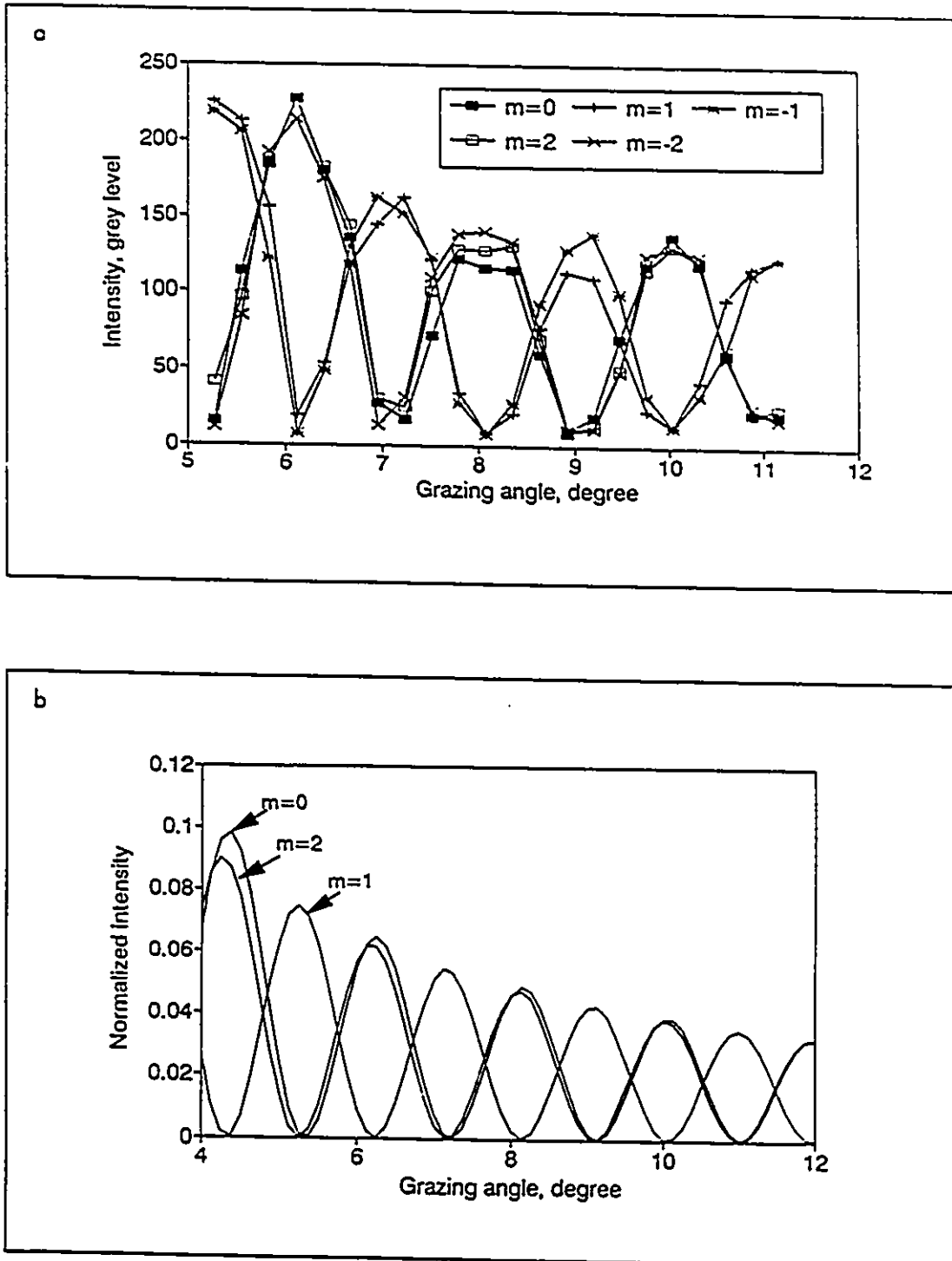


Figure 4.11 Intensity versus incident angle of Sample B:
 (a) Theoretical results, (b) Experimental results

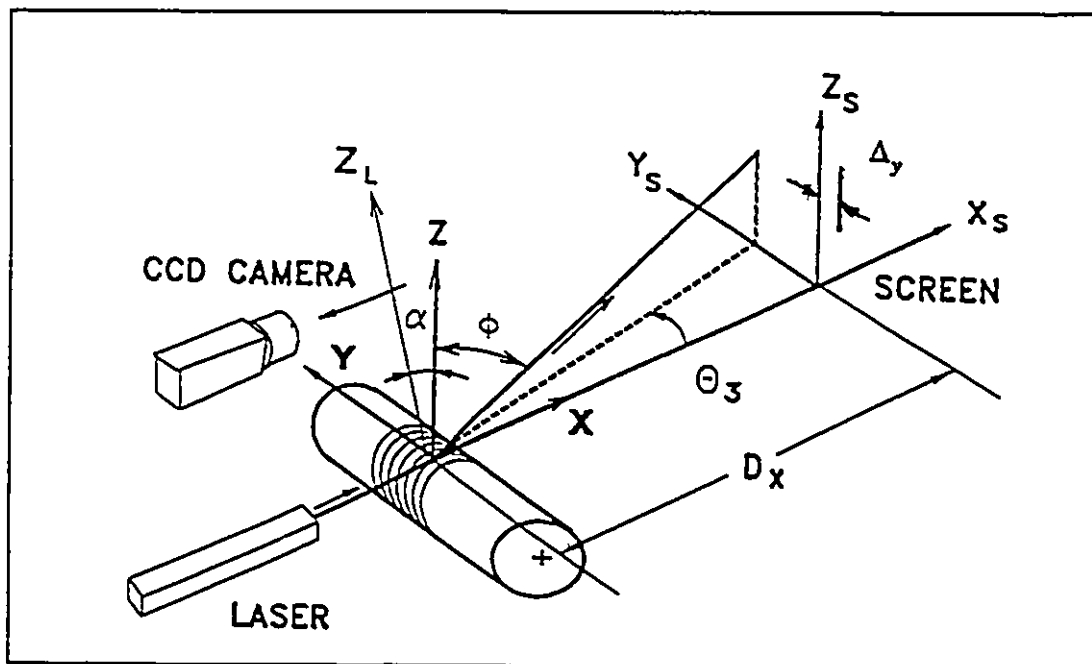


Figure 5.1 Scattering geometry of cylindrical surfaces and measurement setup

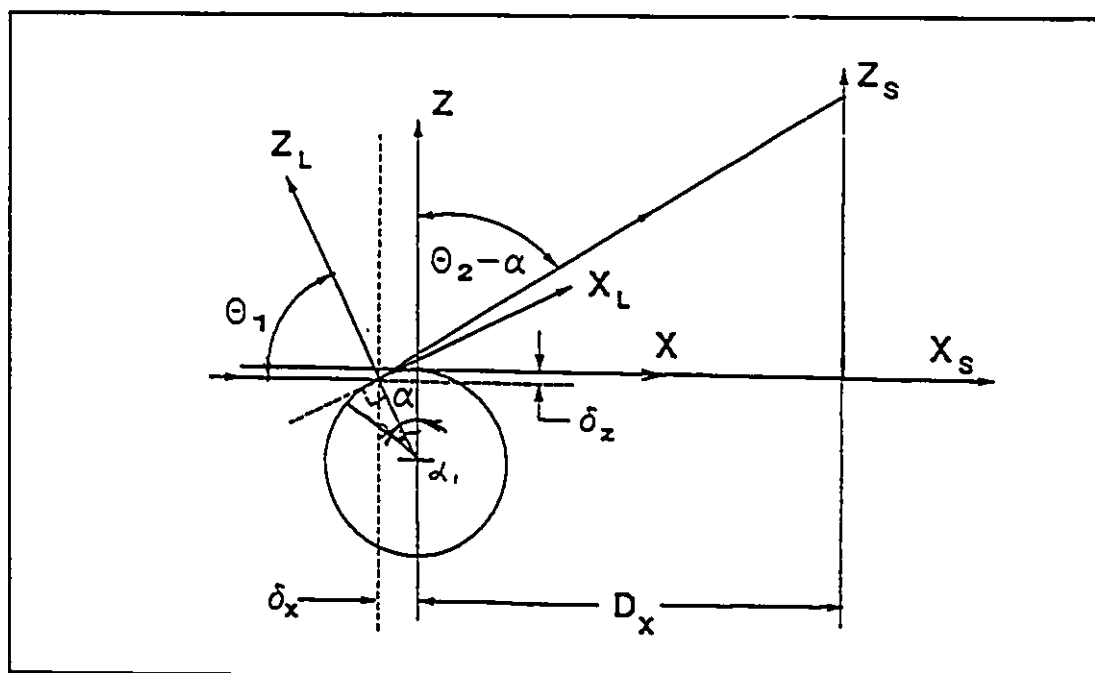


Figure 5.2 Side view of the cylindrical scattering geometry and the screen coordinate system

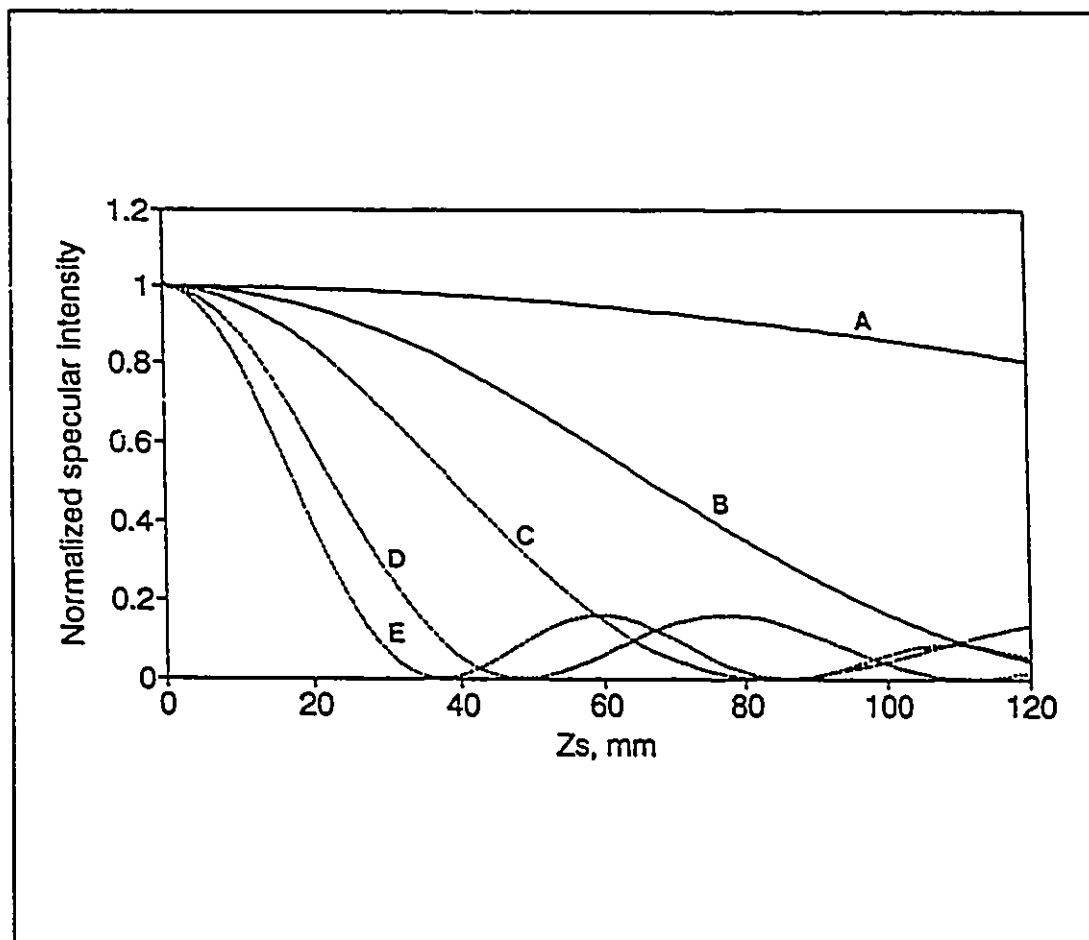


Figure 5.3 Calculated fringe intensities along the zero-order plane for sinusoidal surfaces of different roughness: (A) $H=1.1 \mu\text{m}$ (B) $H=3.4 \mu\text{m}$ (C) $H=5.8 \mu\text{m}$ (D) $H=10 \mu\text{m}$ (E) $H=13 \mu\text{m}$;

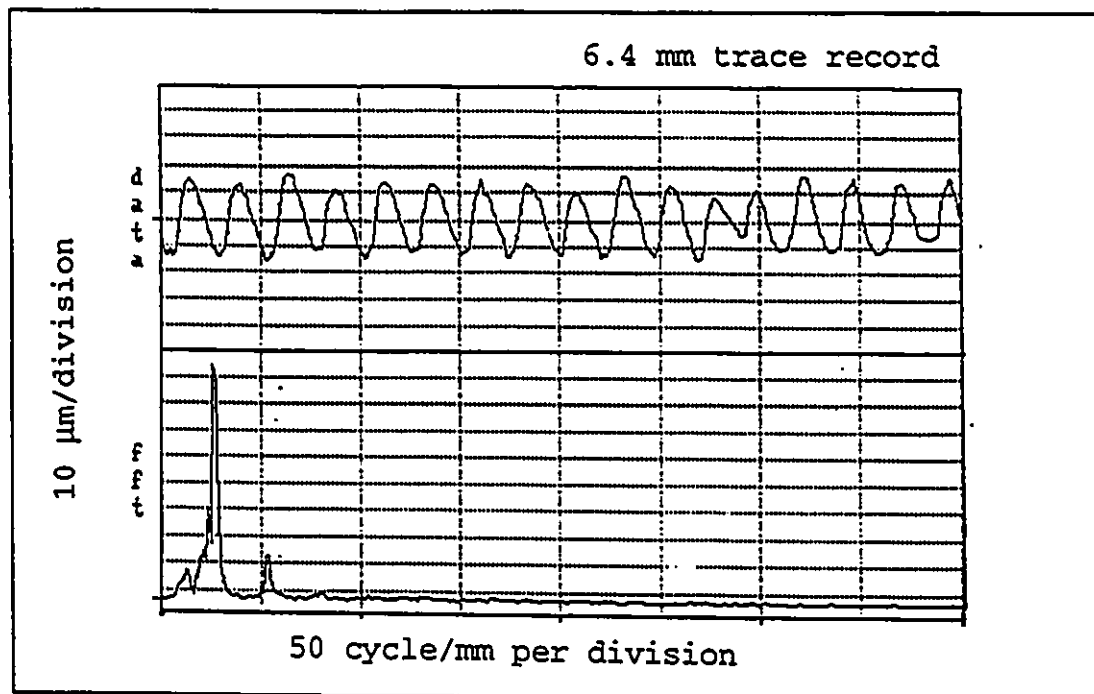
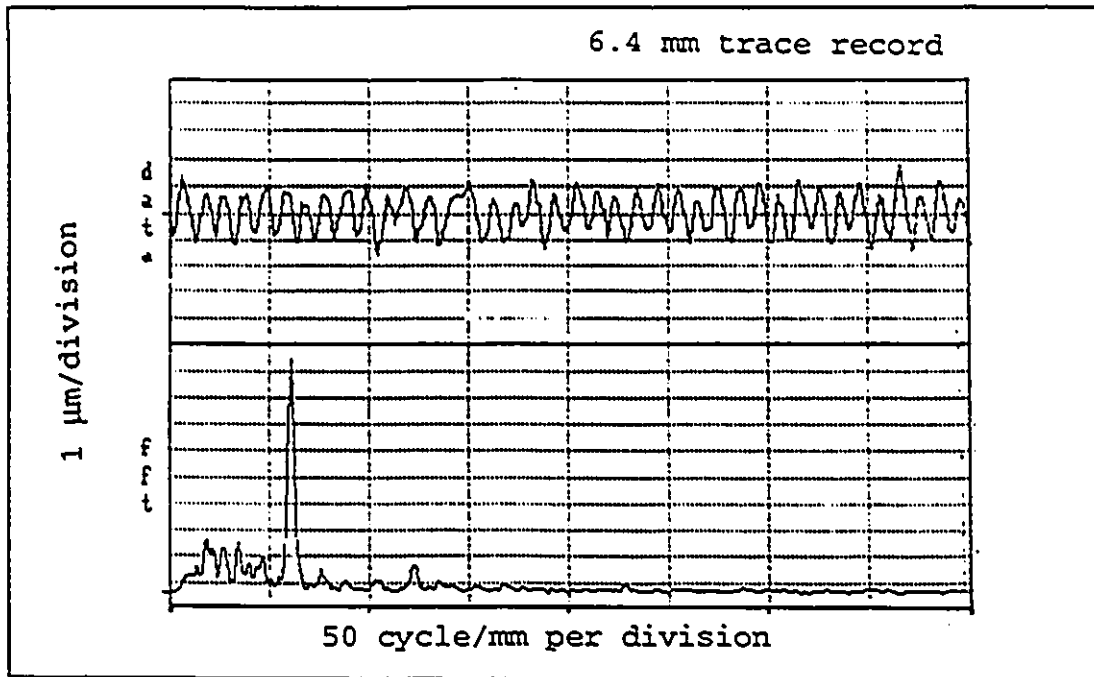


Figure 5.4 Surface roughness profile and its Fourier Transform of two samples: (A) Sample No.2, (B) Sample No.5 in Table 5.2)

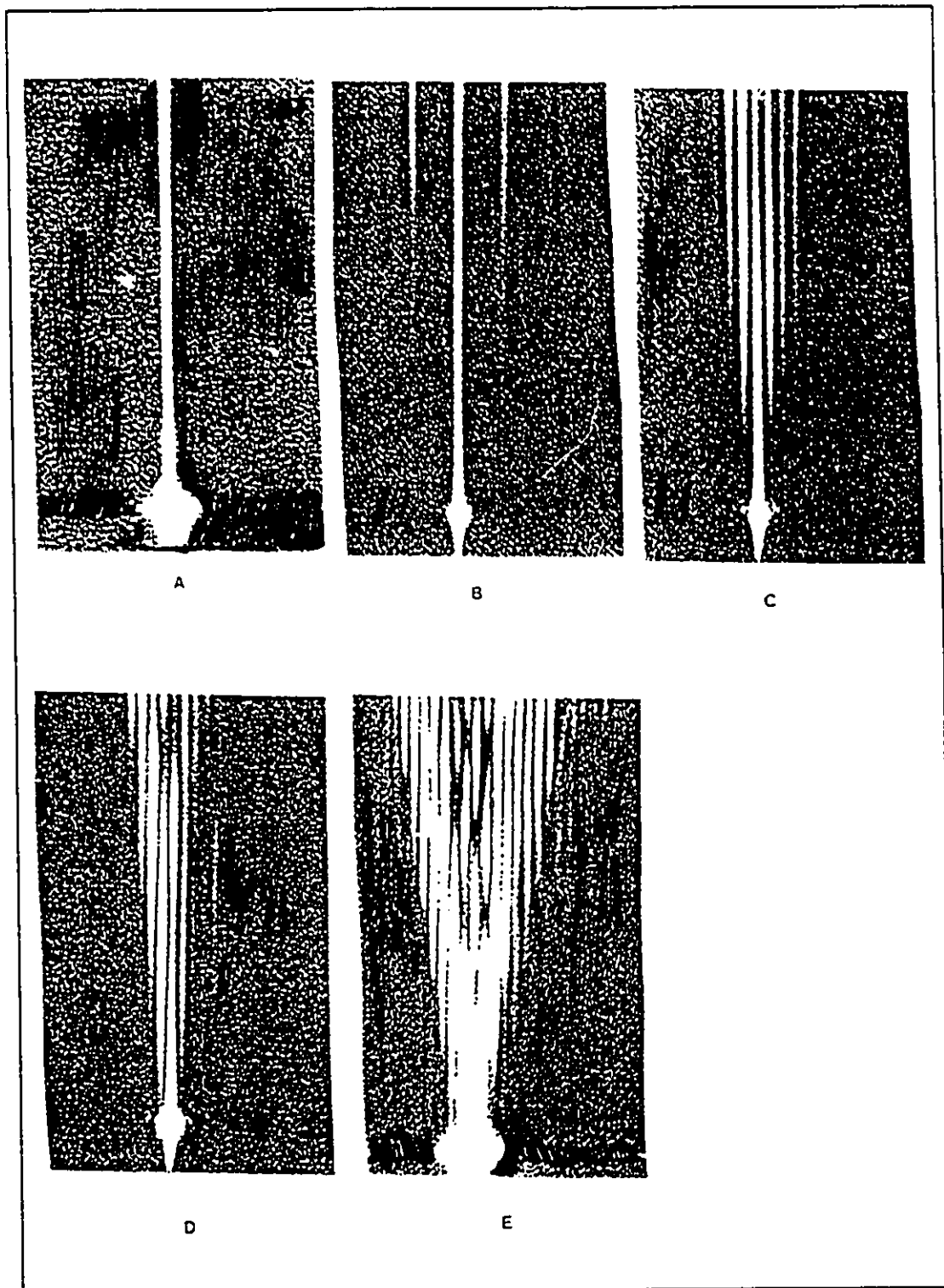


Figure 5.5 Photographs of scattering patterns of the turned sample (A-E). The actual screen image size is 800x500mm

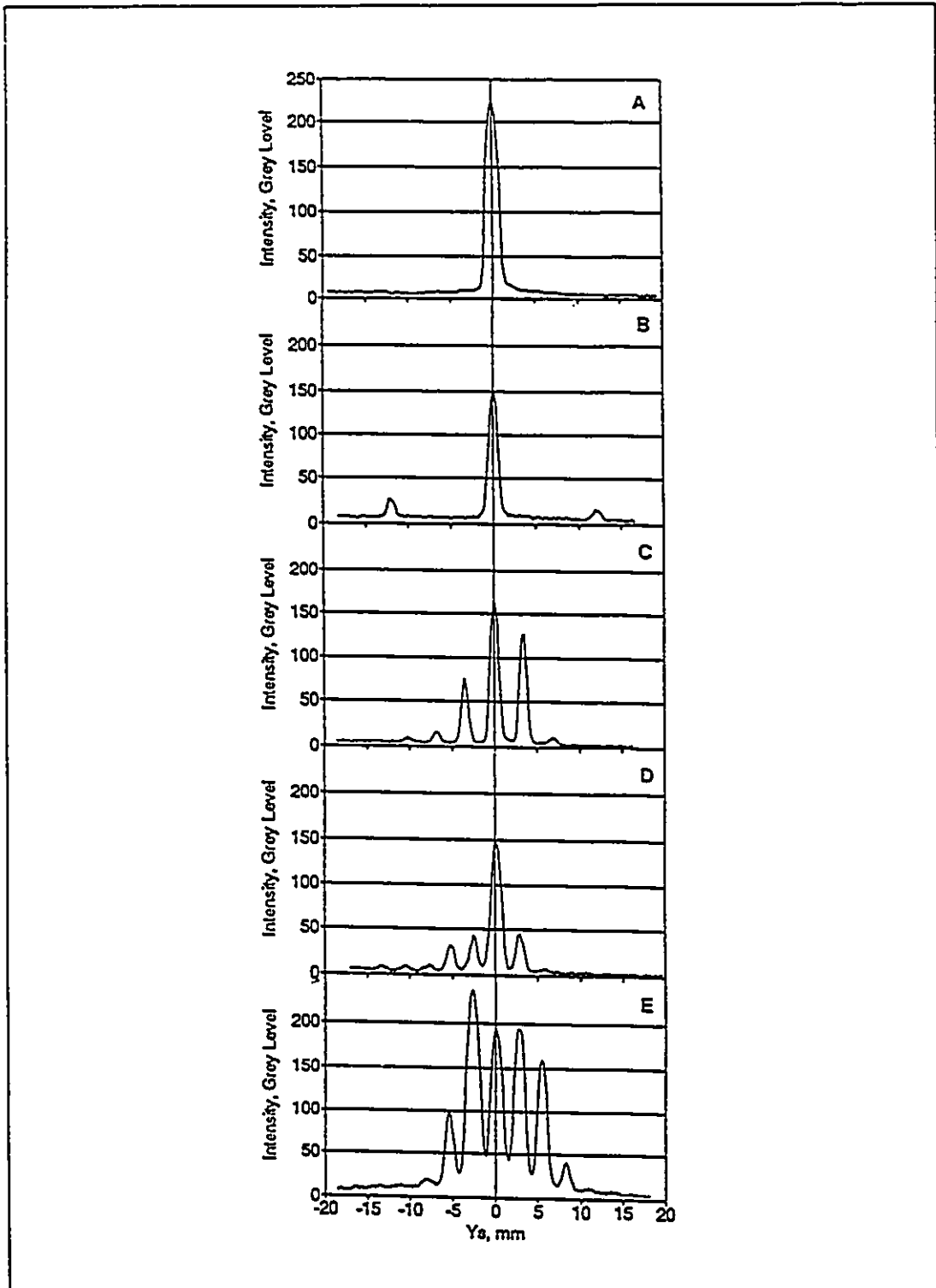


Figure 5.6 Cross-fringe intensity distributions of the test samples (A-E)

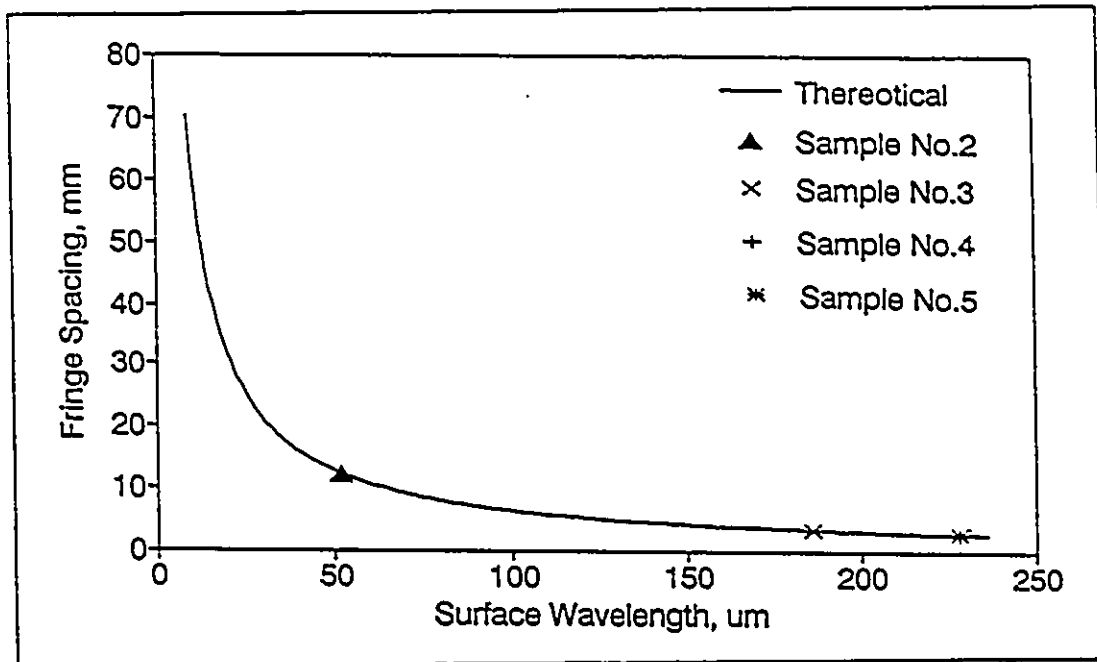


Figure 5.7 Fringe spacing versus surface wavelength

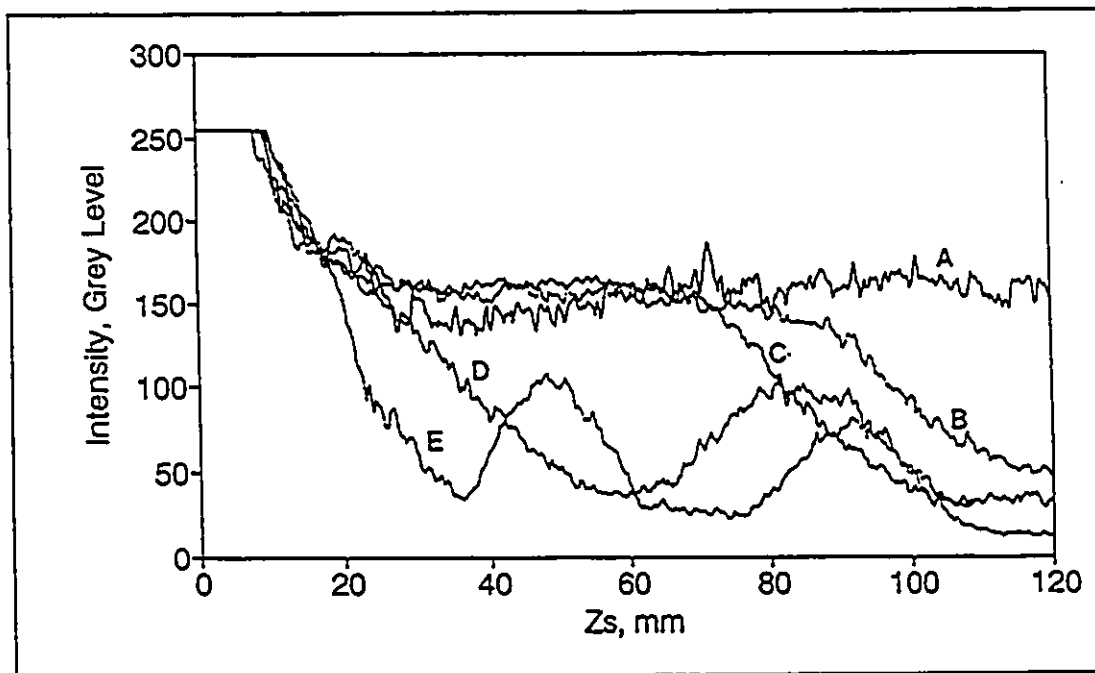


Figure 5.8 Fringe intensity distribution along the central plane (zero-order) for five test Samples A-E in Table 5.2

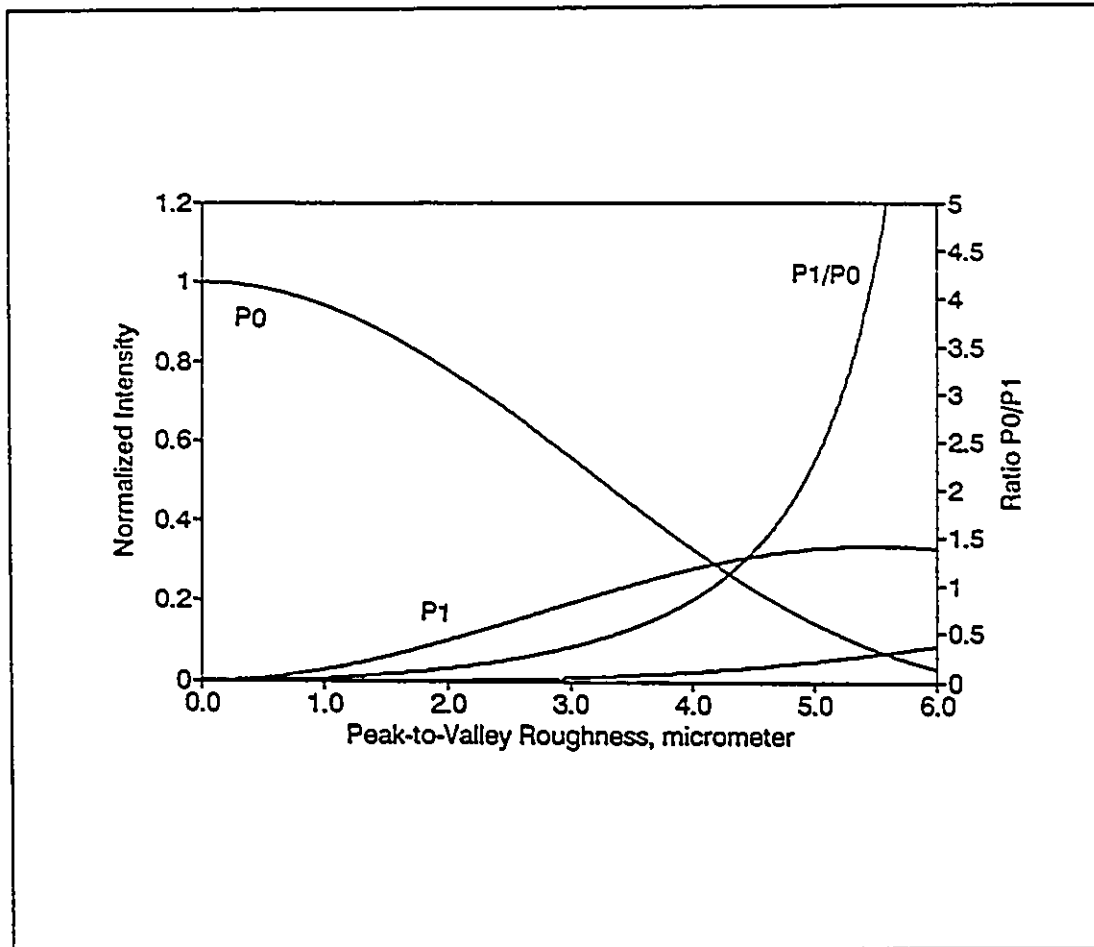


Figure 5.9 Predicted peak intensity and its ratio versus roughness (R_t) using the sinusoidal surface model

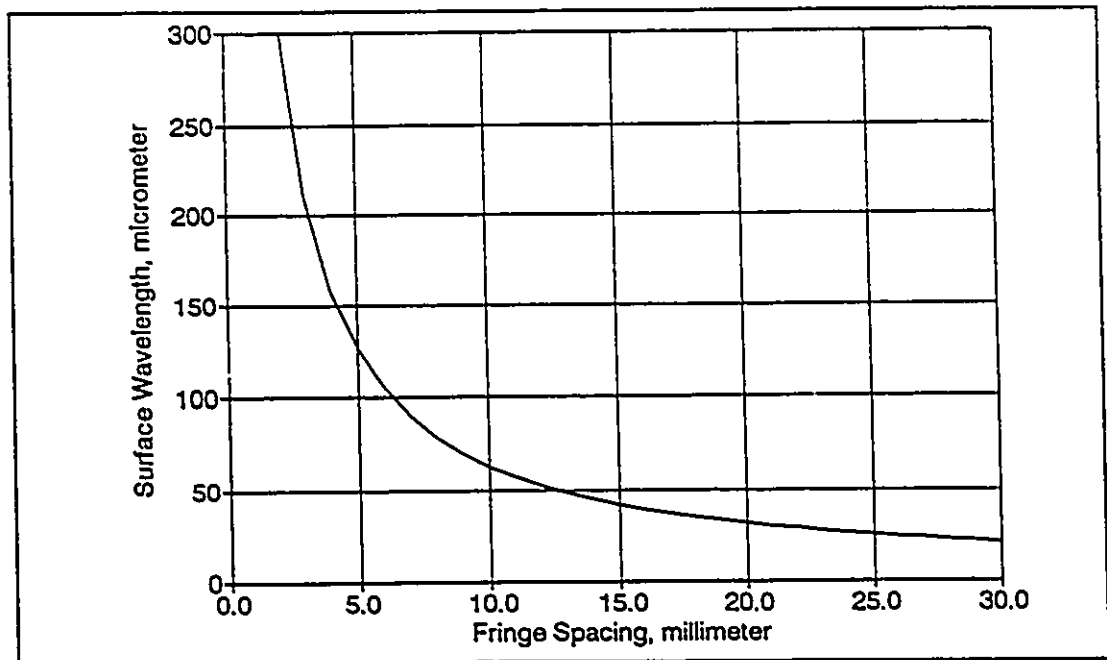


Figure 5.10 Surface wavelength versus fringe spacing

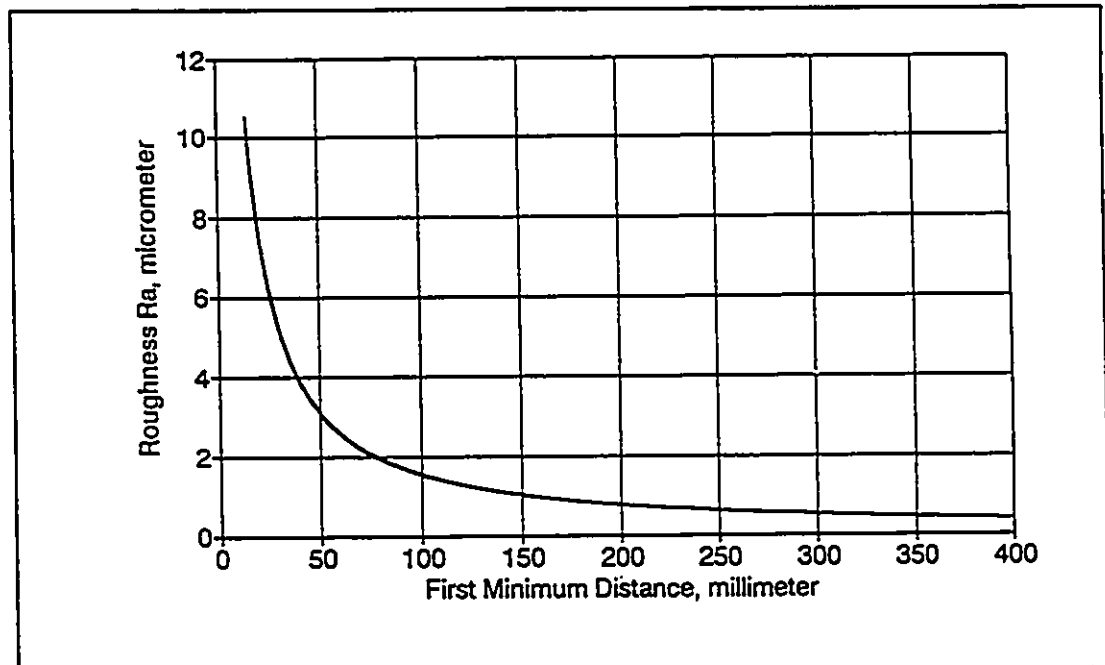


Figure 5.11a Surface roughness (R_a) versus the First Minimum Distance (D_f) for sinusoidal surfaces

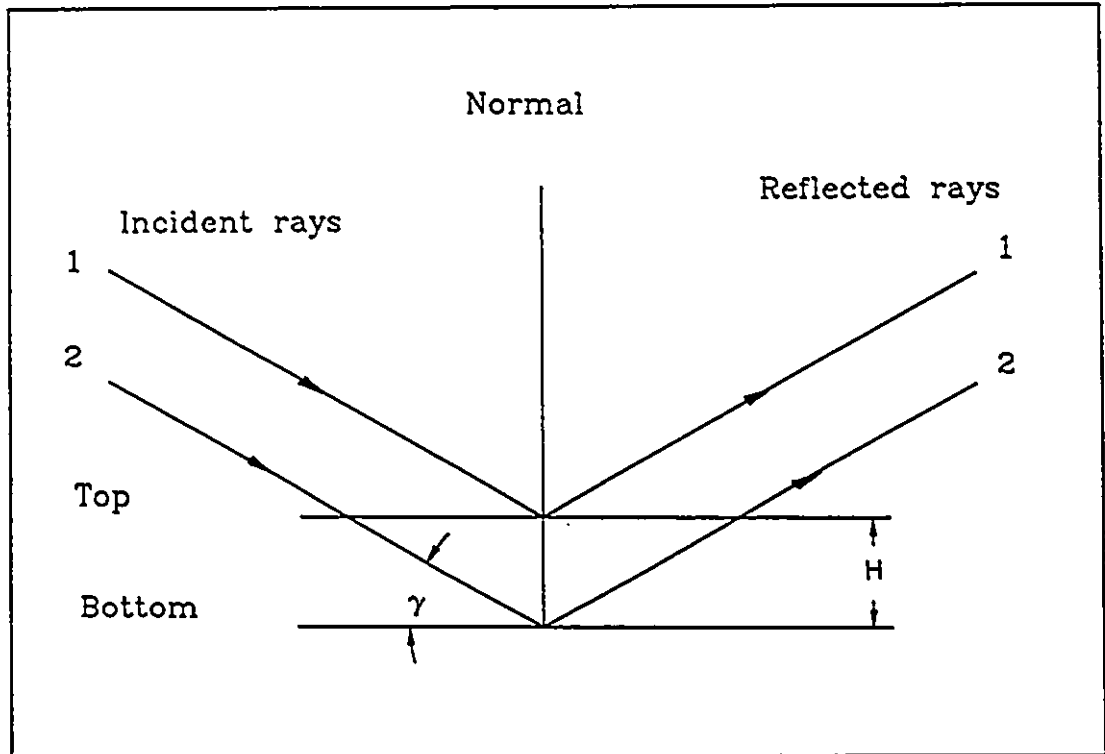


Figure 5.11b Light scattering from a square surface, H =step height, γ =grazing angle

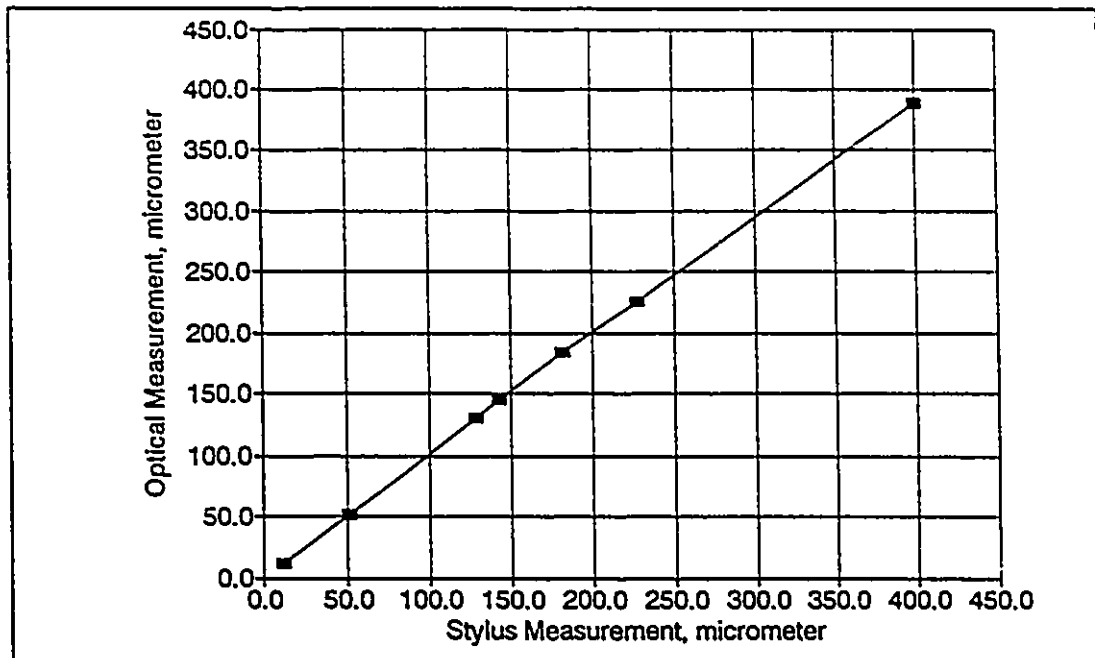


Figure 5.12 Correlation of surface wavelength obtained from the optical and stylus methods

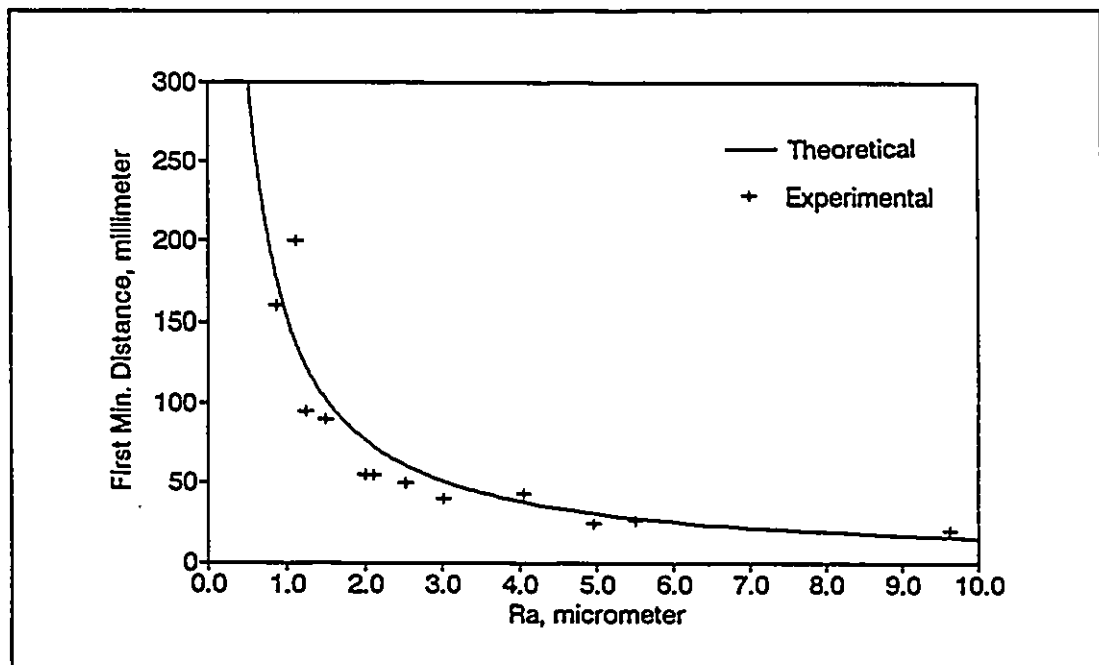


Figure 5.13 Comparison of measured and predicted curves of the first minimum distance (D_f) versus roughness (R_a)

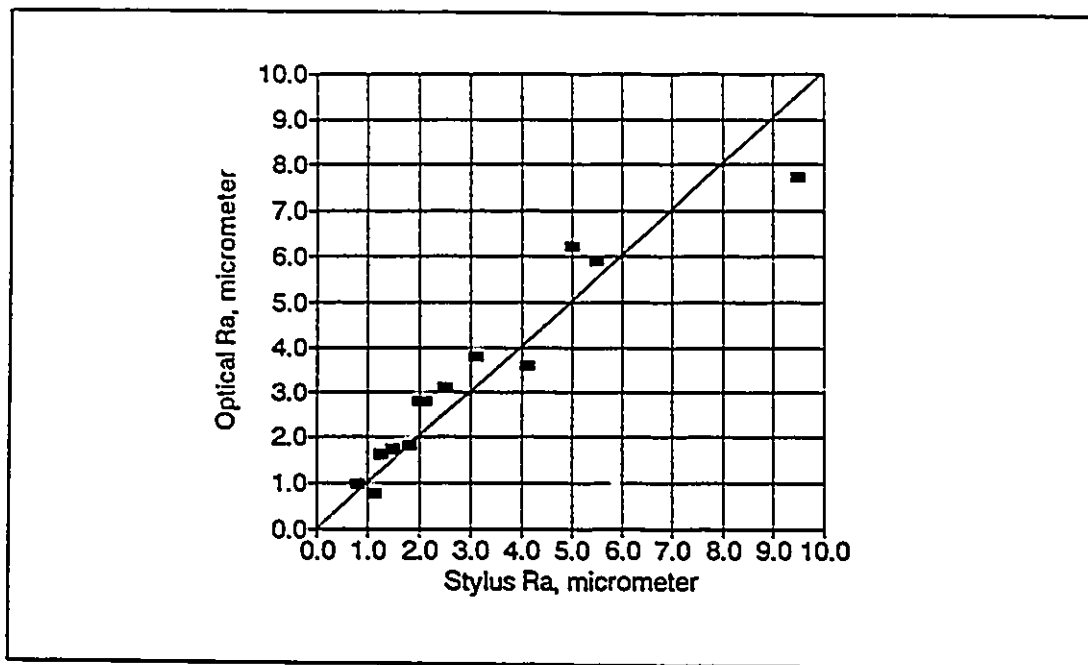


Figure 5.14 Correlation of surface roughness (R_a) obtained by the optical and stylus methods

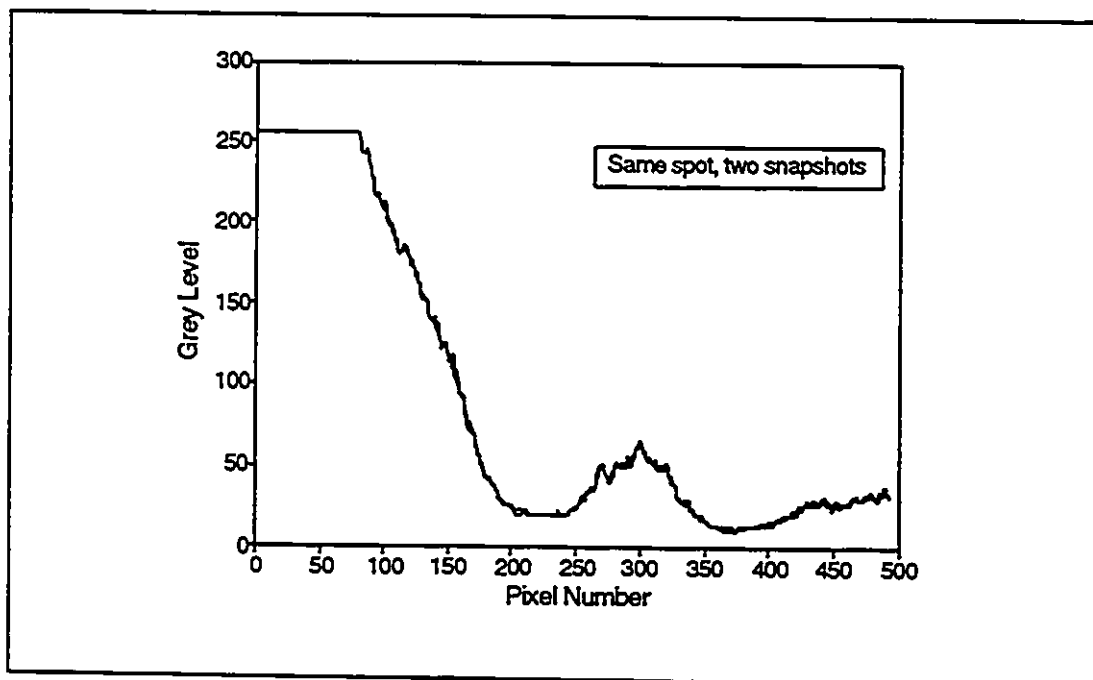


Figure 5.15 Central fringe intensities from two snapshots at the same spot (The two curves are identical)

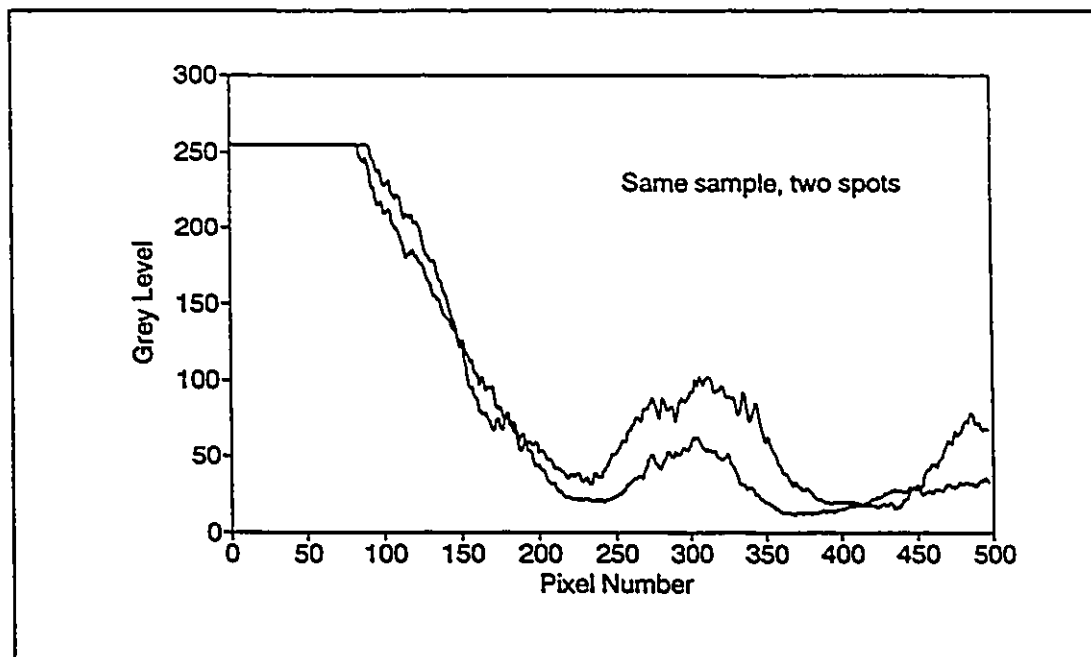


Figure 5.16 Central fringe intensities from two different spots of the same sample

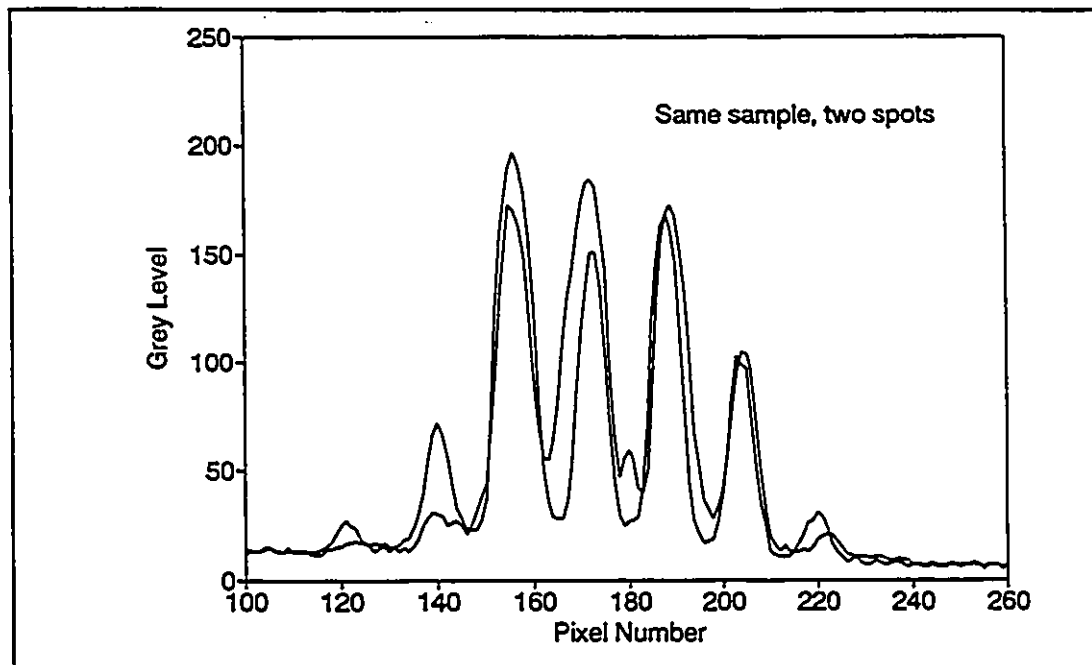


Figure 5.17 Cross-fringe intensity distributions from two spots of the same sample

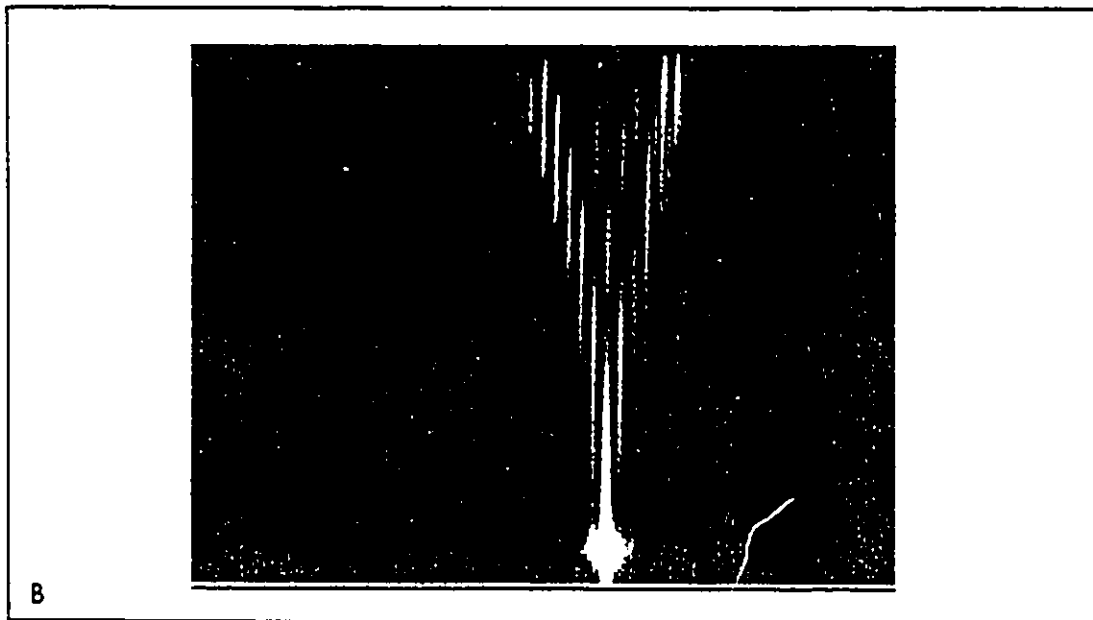
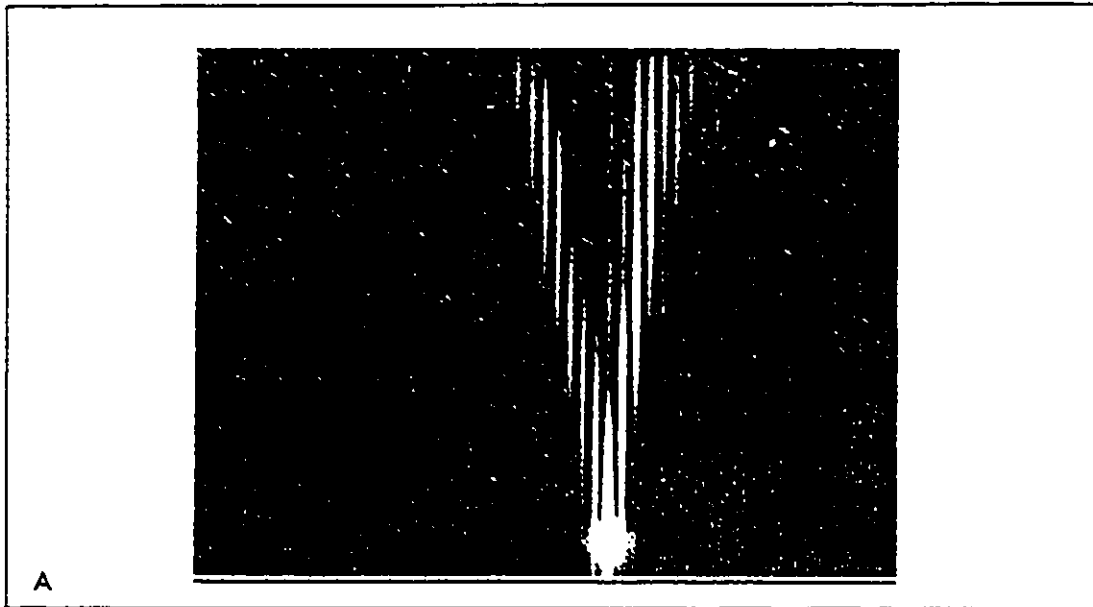


Figure 5.18 Influence of specimen misalignment on the scattering pattern: (A) Proper alignment, (B) 20° misaligned

APPENDIX A

Double Scattering Formula by Ray Optics

Case A: Incidence Plane Perpendicular to the Lay

Consider a ray of light which is obliquely incident upon a triangular surface with an incident angle θ_1 , see Figure A.1. The local incident angle for the left side surface will be $\theta_1 + \alpha$, therefore, it will be reflected at an angle of $2\alpha + \theta_1$. To avoid hitting right side surface, the reflection angle must be smaller than the right side surface slope. It follows that:

$$2\alpha + \theta_1 < 90^\circ - \alpha \quad \text{i.e.: } \theta_1 + 3\alpha < 90^\circ \quad (\text{A.1})$$

This is the necessary condition for avoiding double scattering. It can be shown no shadowing occurs if the above condition is met.

Case B: Incidence Plane Parallel to the Lay

Consider a scattering geometry where the incident beam is in a plane parallel to the lay of a triangular surface, see Figure A.2. Let's consider a ray of light impinge on

the left side of the surface. This ray and the surface normal at the intersection point forms a plane which also contains the reflected beam. The necessary condition for avoiding multiple scattering as established above can also be applied to the beam in this plane using an equivalent incident angle and an equivalent slope. From geometry, the equivalent incident angle θ_{1e} can be derived as:

$$\theta_{1e} = \arcsin(\cos\alpha \cos\theta_1) \quad (\text{A.2})$$

and the equivalent slope of the surface α_e can be found by:

$$\tan\alpha_e = \frac{\sec\alpha - \cos\alpha}{\sqrt{\sec^2\theta_1 - \cos^2\alpha}} \quad (\text{A.3})$$

These are substituted into Equation (A.1) to find the sufficient condition to avoid double scattering

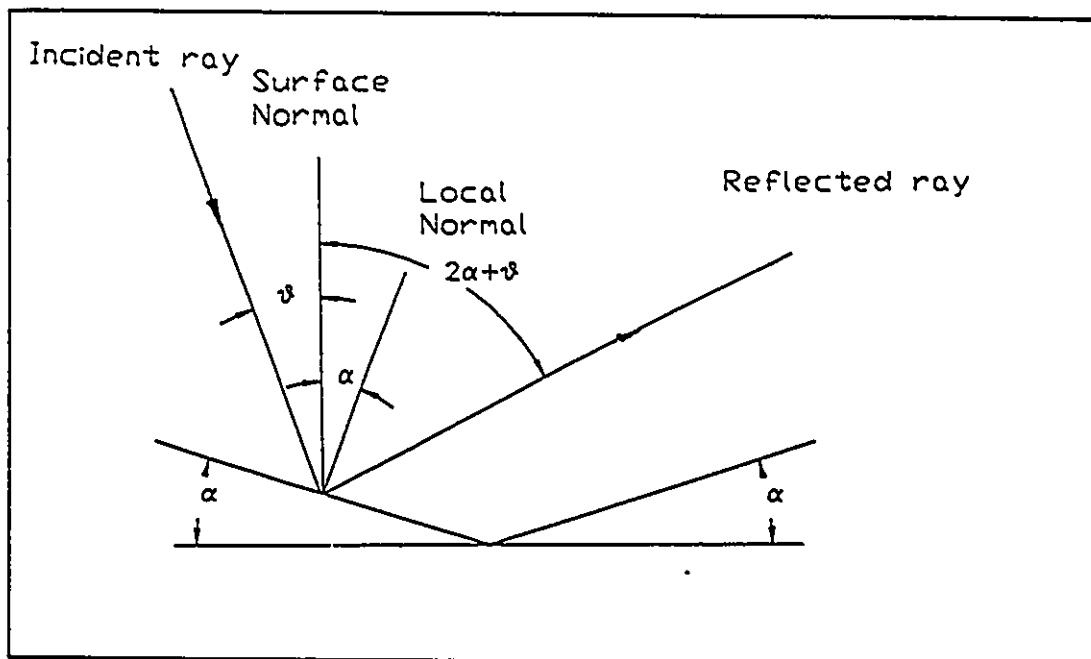


Figure A.1 Light reflection from triangular surface: incident plane perpendicular to the lay

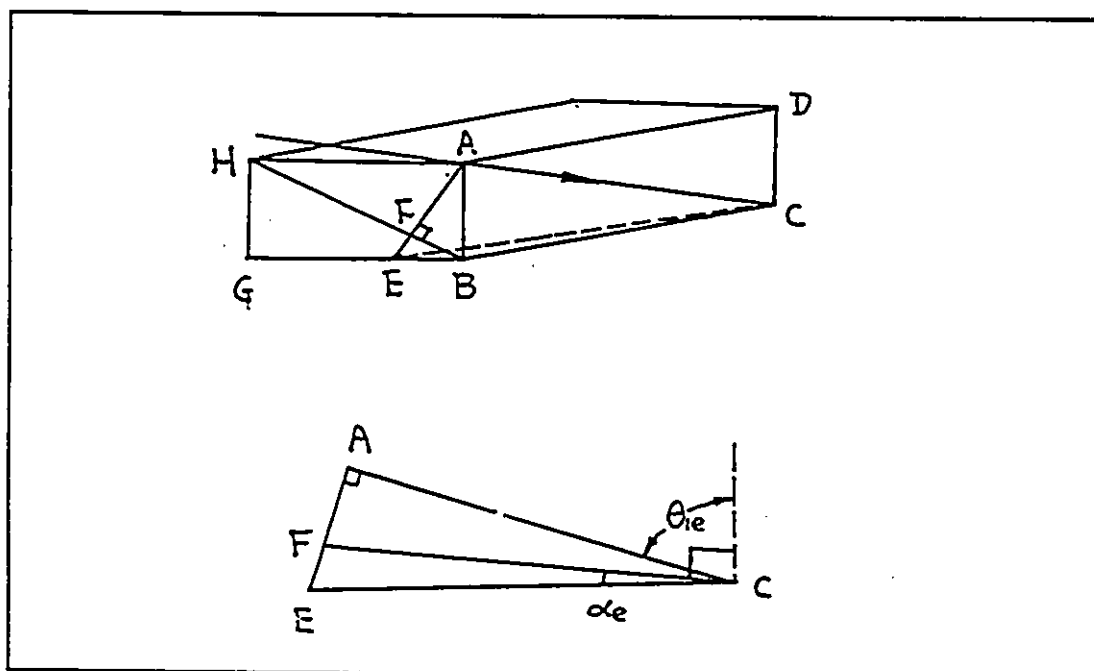


Figure A.2 Light reflection from a triangular surface: incident plane parallel to the lay

APPENDIX B

Equipment Specifications

He-Ne Laser

Manufacturer: Melles Griot, U.S.A.
Model: 05 LHP 121
Wavelength: 632.8 nm
Output Power: 2 mW

CCD Camera

Manufacturer: PULNiX, America, Inc.
Model: TM-845
Resolution: 800(H)x490(V) pixels

Zoom Lens

Manufacturer: Tokina, Japan
Type: 1:1.8
Focal length: 12.5-75 mm

Digitizing Board

Manufacturer: MATROX Electronic Systems Limited, Canada
Model: PIP-1024
Resolution: 512x512 pixels
Gray level: 8 bits

Stylus Profiler

Manufacturer: Mitutoyo Mfg. Co., Ltd., Japan
Model: SurfTest-III
Tip radius: $10 \pm 2.5 \mu\text{m}$
Tip angle: $90^\circ \pm 10^\circ$
Skid radius: 15 mm
Traverse speed: 2-4 mm/s

VITA AUCTORIS

- 1961 Born in Jilin, Jilin, China
- 1984 Received **Bachelor of Science (Automotive Engineering)**
Qinghua University, Beijing, China
- 1988 Received **Master of Science (Mechanical Engineering)**
Queen's University, Kingston, Ontario, Canada